

Nanocrystalline Perovskites for Bright and Efficient Light-Emitting Diodes

Kyung Yeon Jang, Seong Eui Chang, Dong-Hyeok Kim, Eojin Yoon, and Tae-Woo Lee*

Nanocrystalline perovskites have driven significant progress in metal halide perovskite light-emitting diodes (PeLEDs) over the past decade by enabling the spatial confinement of excitons. Consequently, three primary categories of nanocrystalline perovskites have emerged: nanoscale polycrystalline perovskites, quasi-2D perovskites, and perovskite nanocrystals. Each type has been developed to address specific challenges and enhance the efficiency and stability of PeLEDs. This review explores the representative material design strategies for these nanocrystalline perovskites, correlating them with exciton recombination dynamics and optical/electrical properties. Additionally, it summarizes the trends in progress over the past decade, outlining four distinct phases of nanocrystalline perovskite development. Lastly, this review addresses the remaining challenges and proposes a potential material design to further advance PeLED technology toward commercialization.

anion (e.g., Cl⁻, Br⁻, or I⁻).^[2] This structural versatility allows for precise tuning of the emission wavelength.^[3,4]

As a result, perovskite emitters can cover the entire visible spectrum and match the wavelengths required for the Rec. 2020 color standard (red: 630 nm, green: 532 nm, blue: 467 nm). Additionally, the intrinsically narrow full-width at half maximum (FWHM) of perovskite emission spectra (< 20 nm) aligns well with the requirements of a wide color gamut in ITU-R Recommendation BT.2020 (Rec. 2020), which is the standard for future display colors.^[1] This feature offers a significant advantage in color purity over organic light emitters and conventional inorganic quantum dots (QDs) such as II-VI (e.g., CdSe) and III-V (e.g., InP) QDs.^[5]

Notably, perovskites demonstrate exceptional advantages in the green emission region compared to the other types of emitting materials. With an emission wavelength of 532 nm and a narrow FWHM of ≈ 20 nm, achieve a CIE_y > 0.76, covering almost 100% of the Rec. 2020 color gamut.^[6] This performance significantly surpasses that of conventional green phosphorescent organic light-emitting diodes (OLEDs), which typically exhibit CIE_x ≈ 0.30 and CIE_y ≈ 0.65 , covering only $\approx 70\%$ of the Rec. 2020 standard due to undesirable shoulder peaks.^[7] Similarly, green InP QDs exhibit broader FWHM values of ≈ 34 nm, primarily due to their strongly size-dependent emission properties.^[8]

In addition to their outstanding optical properties, perovskites provide substantial advantages in production. Unlike organic emitters, which require complex synthesis processes taking several days to weeks, or inorganic QDs, which demand several tens of hours, perovskites can be processed into thin films or synthesized as colloidal nanoparticles in less than an hour. Thin films can be fabricated using simple spin-coating techniques, while colloidal nanoparticles are synthesized through reprecipitation under ambient conditions. This simplicity not only reduces production costs but also enhances scalability. Moreover, perovskites are derived from cost-effective metal halide precursors with minimal additives, making their material costs substantially lower than those of alternative emitting materials.^[1]

Despite these advantages, bulk perovskite was initially not an ideal light emitter due to its low exciton binding energy and long exciton diffusion length.^[9] However, extensive research has overcome intrinsic limitations, focusing on the development of three key types of nanocrystalline perovskites: nanoscale polycrystalline (PC) film,^[10] quasi-2D (Q2D) perovskites,^[11] and

1. Introduction

Perovskite light-emitting diodes (PeLEDs) have exceptional properties, particularly high color tunability and purity of emission spectrum, and therefore have been identified as promising candidates for next-generation display technologies.^[1] The emission wavelength of perovskites can be readily adjusted by modifying the components of their ABX₃ crystal structure, where A is a monovalent cation (e.g., organic methylammonium (MA⁺) or formamidinium (FA⁺), or inorganic cesium (Cs⁺)), B is a divalent inorganic cation (e.g., lead (Pb²⁺), tin (Sn²⁺)), and X is a halide

K. Y. Jang, S. E. Chang, D.-H. Kim, E. Yoon, T.-W. Lee
 Department of Materials Science and Engineering
 Seoul National University
 1 Gwanak-ro, Gwanak-gu, Seoul08826, Republic of Korea
 E-mail: twlees@snu.ac.kr

T.-W. Lee
 Research Institute of Advanced Materials (RIAM)
 Institute of Engineering Research
 Soft Foundry
 Interdisciplinary Program in Bioengineering
 Seoul National University
 1 Gwanak-ro, Gwanak-gu, Seoul08826, Republic of Korea
 T.-W. Lee
 SN Display Co.
 Ltd.
 1 Gwanak-ro, Gwanak-gu, Seoul08826, Republic of Korea

 The ORCID identification number(s) for the author(s) of this article can be found under <https://doi.org/10.1002/adma.202415648>

DOI: 10.1002/adma.202415648

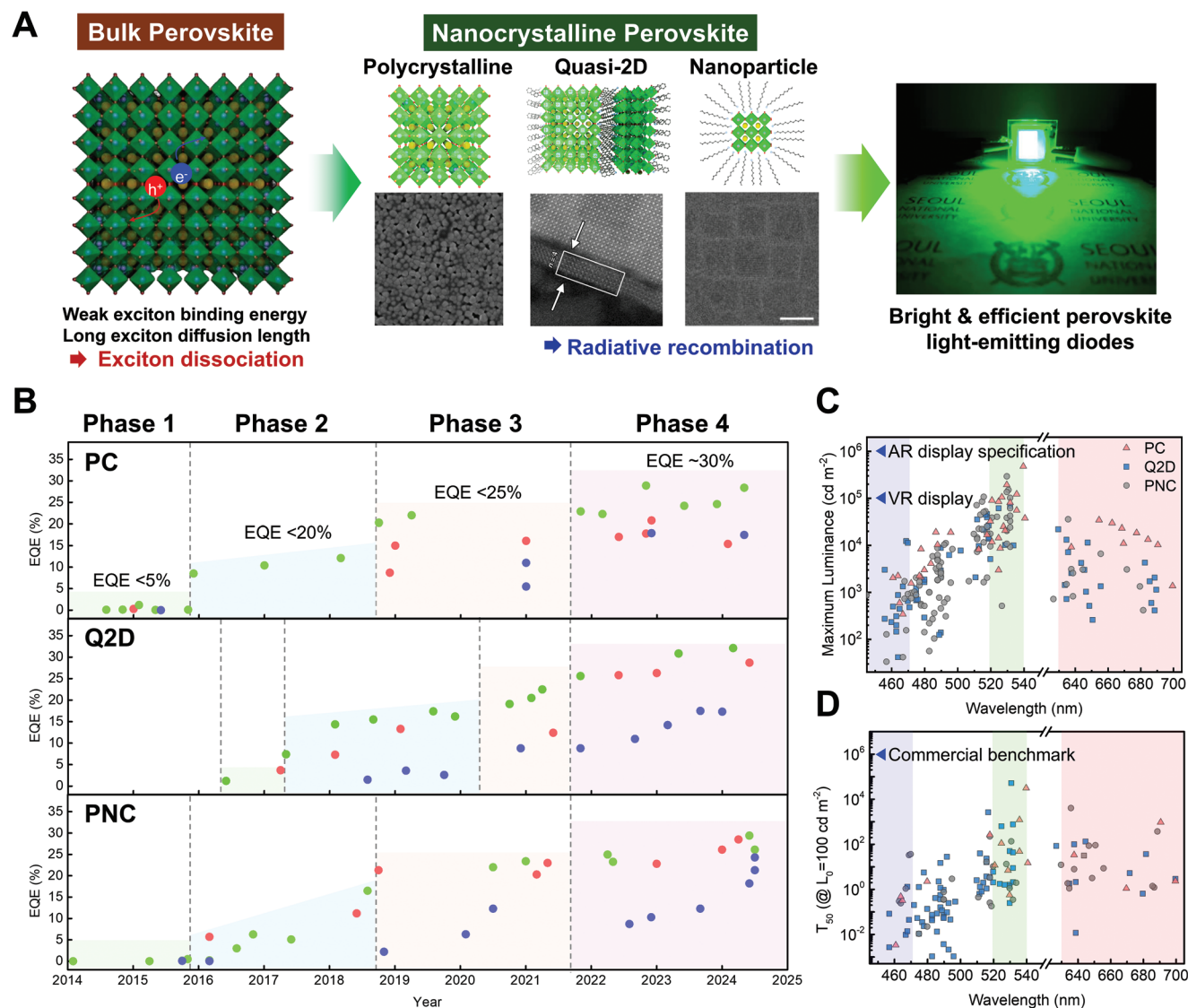


Figure 1. A) Schematic illustration of bulk perovskite and nanocrystalline perovskite structures, including SEM image of polycrystalline perovskite,^[14] and TEM images of quasi-2D perovskite^[69] and perovskite nanoparticles^[6] for PeLEDs. Reproduced with permission.^[6,14,69] Copyright 2022, Springer Nature. Copyright 2020, Springer Nature. Copyright 2024, Springer Nature. B) Development over time of the external quantum efficiency (EQE) of PeLEDs that use polycrystalline (including in situ nanocrystal), quasi-2D, or perovskite nanocrystals for red, green, and blue (peak wavelength < 480 nm) emissions. C) Maximum luminance for PeLEDs that use polycrystalline perovskite (red triangle), quasi-2D perovskite (blue square), and perovskite nanocrystal (grey circle), with commercial luminance requirements for VR displays (10⁵ cd m⁻²) and AR displays (10⁶ cd m⁻²) indicated. D) Operational lifetime (T₅₀) at an initial luminance of 100 nits for PeLEDs that use polycrystalline perovskite (red triangle), quasi-2D perovskite (blue square), and perovskite nanocrystal (grey circle), with the commercial benchmark of 10⁶ h indicated.

perovskite nanocrystals (PNCs).^[12] These nanocrystalline perovskites spatially confine excitons and facilitate radiative recombination while suppressing non-radiative decay pathways (Figure 1A). In particular, PeLEDs utilizing nanoscale polycrystalline perovskites achieved the first high-efficiency PeLEDs in 2015.^[10] As a result, PeLEDs using nanocrystalline perovskites have demonstrated significant improvements in external quantum efficiency (EQE), luminance, and operational lifetime over the past decade. A comparison of these achievements with the requirements for commercialization is provided below.

The EQE of PeLEDs has improved dramatically. Early PeLEDs reported in 2014 had a maximum EQE (EQE_{max}) of only 0.1%.^[13]

In contrast, recent advancements using nanocrystalline perovskites have achieved an EQE_{max} ≈ 30% (Figure 1B).^[6,14] The rapid progress of the EQE positions PeLEDs as competitive with commercial OLEDs, and thereby fulfills a key requirement for commercialization.

When evaluating the EQE improvements across different types of nanocrystalline perovskites, it is important to consider optical effects. While the EQE approaches the theoretical efficiency limit for single-junction devices, the actual improvements in PeLEDs using PC perovskite films are enhanced by photon recycling effects from a thick emissive layer^[14] or enhanced light outcoupling efficiency due to scattering from uneven perovskite

Table 1. Comparison of performance between state-of-the-art PeLEDs and inorganic QD-LEDs.

Type	EL Peak	FWHM	EQE	Luminance	Operational Lifetime (T_{50} @ 100 cd m ⁻²)	Refs.
Cd-based	600 nm	–	21.6%	356 000 cd m ⁻²	1 600 000 h	[227]
QD-LED	537 nm	26 nm	28.7%	>200 000 cd m ⁻²	2 570 000 h	[228]
	525 nm	–	22.9%	614 000 cd m ⁻²	1 760 000 h	[227]
	479 nm	23 nm	21.9%	>50 000 cd m ⁻²	24 000 h	[228]
Cd-free	630 nm	35 nm	21.4%	100 000 cd m ⁻²	1 000 000 h	[229]
QD-LED	543 nm	38.2 nm	26.68%	277 000 cd m ⁻²	508 349 h	[230]
	457 nm	–	20.2%	88 900 cd m ⁻²	15 850 h	[231]
PeLED	636 nm	28 nm	22%	7000 cd m ⁻²	780 (T_{90} @ 100 cd m ⁻²)	[22]
	540 nm	–	28.9%	473 990 cd m ⁻²	31 858 h	[14]
	531 nm	20 nm	26.1%	10 908 cd m ⁻²	5.0 h	[6]
	531 nm	22.1 nm	29.5%	147 872.8 cd m ⁻²	50 317 h	[21]
	470 nm	–	21.3%	635 cd m ⁻²	–	[147]
	465 nm	–	16.7%	430 cd m ⁻²	–	[147]

grains.^[15] The optical effect is relatively small in PNCs but more pronounced in PC films, making it difficult to fairly compare the EQE values between PNCs and PCs. Therefore, to accurately assess the EQE improvement of pure nanocrystalline perovskite materials, comparisons should exclude the influence of optical effects.

Maximum luminance (L_{\max}) is a crucial performance parameter in PeLEDs, with significant progress made across different emission colors. Green-emitting PeLEDs have achieved L_{\max} up to $\approx 470\,000$ cd m⁻²,^[14] red-emitting PeLEDs have reached $\approx 30\,000$ cd m⁻²,^[16] and blue-emitting PeLEDs have achieved $\approx 12\,000$ cd m⁻² (Figure 1C).^[17] The lower luminance in the blue and red colors compared to green is attributed to the differences in photopic luminous efficiency. While these luminance levels are suitable for applications such as indoor high-dynamic-range television (> 1000 cd m⁻²) and could be potentially suitable for outdoor displays (> 3000 cd m⁻²),^[18] they need to be further enhanced for virtual reality (VR) displays and significantly improved for augmented reality (AR) displays. Both AR and VR displays require complex optical paths, including significant optical losses of $\approx 75\%$ in VR displays using pancake lenses and up to 99% in AR displays using optical combiners. To achieve the necessary dynamic range and ambient contrast ratio, the luminance needs to reach $\approx 10^5$ cd m⁻² for VR displays and 10^6 cd m⁻² for AR displays.^[19,20]

Finally, operational lifetime remains a significant challenge. The commercial requirement for operational lifetime in televisions or mobile phones that have high average daily usage is typically $T_{95} \approx 10^4$ h at initial luminance $L_0 = 1000$ cd m⁻². For other practical mobile applications, excluding frequently-used televisions or mobile phones, a T_{50} of at least 10^6 h at $L_0 = 100$ cd m² is required, considering the average daily usage and replacement cycle of electronic devices.^[1] However, the longest reported operational lifetime at $L_0 = 100$ cd m² in PeLEDs is $T_{50} = 31\,808$ h in green PC-PeLEDs, and 50 317 h in green Q2D-PeLEDs.^[14,21] In comparison, red-emitting PeLEDs exhibit a $T_{50} \approx 3900$ h (estimated from $T_{90} = 780$ h),^[22] while blue-emitting PeLEDs show a significantly shorter $T_{50} \approx 35$ h,^[23] which represents the longest operational lifetimes achieved so far. Com-

pared to other emerging LED technologies using conventional inorganic QDs, the operational lifetime of PeLEDs still falls significantly short, highlighting a critical challenge for PeLEDs to achieve the stability required for practical applications (Table 1). At their current stage of development, PeLEDs are more suitable for applications with shorter display usage times, such as smart-watches, cameras, and fitness trackers. However, significant challenges remain, especially for red and blue PeLEDs, which require substantial improvements to reach commercial viability (Figure 1D).

The progress made in PeLEDs is the result of strategic material design efforts focused on PC perovskites, Q2D perovskites, and PNCs. However, much of the research in each area has primarily concentrated on addressing specific issues individually. Therefore, organizing these diverse strategies is valuable for offering a more comprehensive understanding of the field. Achieving the ultimate goal of PeLED commercialization will require addressing multiple complex challenges simultaneously. In this review, we integrate strategic material design approaches for three types of nanocrystalline perovskites, discussing how targeted efforts have enhanced the optical/electrical properties. By bringing these strategies together, we aim to facilitate the development of more precise and advanced nanocrystalline PeLEDs. Finally, we offer insights into future material requirements and the remaining challenges for advancing PeLED technology.

2. Recombination in Nanocrystalline Perovskite

Understanding the advances and remaining obstacles in PeLED technology requires an examination of the mechanisms of radiative recombination in nanocrystalline perovskites. To develop perovskites as efficient light emitters, limitations related to their excitonic properties must be overcome. Bulk perovskite is not an ideal light emitter because of several characteristics. One significant limitation of bulk lead halide perovskites is due to their inherently high relative dielectric constant, which leads to substantial screening of the electric field within the crystal.^[24] This electric field screening results in the formation of excitons that have low exciton binding energy, typically only 30–50 meV

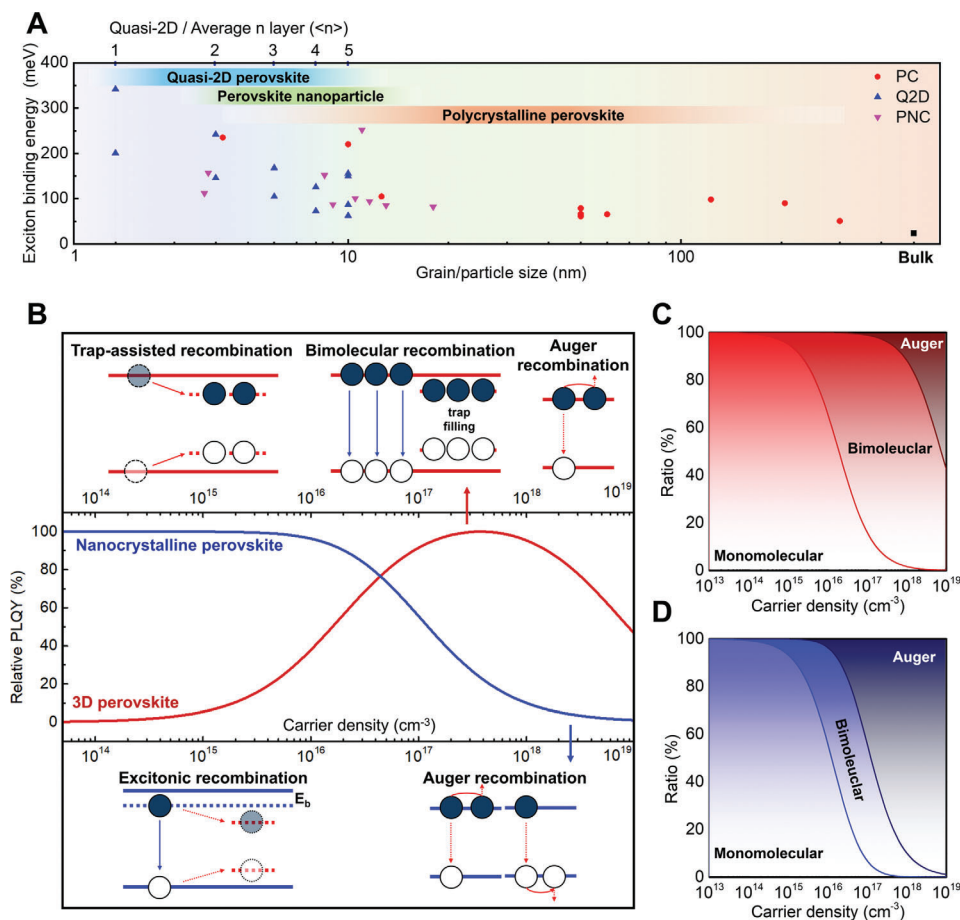


Figure 2. A) Exciton binding energy versus grain/particle size of polycrystalline, quasi-2D, and nanoparticle perovskites. B) Relative PLQY curve as a function of carrier density, illustrating the major exciton recombination mechanisms for 3D perovskites (top) and nanocrystalline perovskites (bottom). 3D perovskites exhibit low PLQY at low carrier densities due to dominant trap-assisted recombination but achieve high PLQY in the high carrier density regime due to radiative bimolecular recombination (red solid line). In contrast, nanocrystalline perovskites exhibit high PLQY at low carrier densities due to efficient radiative excitonic recombination but show a decline at high carrier densities due to non-radiative Auger recombination. C) Proportions of monomolecular, bimolecular, and Auger recombination for 3D perovskites as a function of carrier density, derived from theoretical calculations using the recombination constants of 3D perovskites. D) Proportions of the same recombination mechanisms for nanocrystalline perovskites, calculated using the recombination constants of nanocrystalline Q2D perovskites.

(Figure 2A).^[25] Such low exciton binding energy facilitates thermal ionization of electron-hole pairs (or excitons) to form free carriers. Moreover, the high charge-carrier mobility and long exciton diffusion lengths, coupled with slow recombination rates, allow charge carriers to diffuse easily within the grains. This increases the possibility of carriers being trapped in defect states or being extracted by charge-transporting layers; these characteristics are more suited to photovoltaic applications than to light emission.^[9]

However, the development of nanocrystalline perovskites has established perovskites as efficient light emitters. The spatial confinement increases the exciton binding energy from ≈ 30 meV in bulk perovskites to 50–300 meV in nanocrystalline perovskites (Figure 2A).^[14,26,27] This increased exciton binding energy prevents the formation of free carriers and promotes radiative excitonic recombination. Additionally, decreasing the grain size limits exciton diffusion, thereby reducing the probability of exciton quenching.^[10]

From a practical perspective on recombination mechanisms, the development of LEDs aims for radiative recombination (either monomolecular (exciton recombination) or bimolecular (free carrier recombination) that efficiently converts charge carriers to light. In bulk perovskites, due to the low exciton binding energy and high dielectric constant, charge carriers exist predominantly as free electrons and holes, and radiative recombination occurs by bimolecular processes.^[28] The charge carrier density depends on the time can be described as:^[29,30]

$$-\frac{dn}{dt} = k_1 n + k_2 n^2 + k_3 n^3 \quad (1)$$

where n [cm^{-3}] is charge-carrier density, t [s] is time, k_1 is the monomolecular recombination rate (including non-radiative trap-assisted recombination and radiative excitonic recombination), k_2 is the radiative bimolecular recombination rate, and k_3 is the non-radiative Auger recombination rate. This equation can

be used to obtain the photoluminescence quantum yield (PLQY) of the radiative recombination of bulk 3D perovskite as:

$$\eta(n) = \frac{k_2 n}{k_1 + k_2 n + k_3 n^2} \quad (\text{in bulk 3D perovskite}) \quad (2)$$

In typical bulk 3D perovskite, $10^6 \leq k_1 \leq 10^7 \text{ s}^{-1}$, $k_2 \approx 10^{-10} \text{ cm}^3 \text{ s}^{-1}$, and $k_3 \approx 10^{-28} \text{ cm}^6 \text{ s}^{-1}$.^[31] Under these conditions, monomolecular trap-assisted recombination dominates at $n < 10^{16} \text{ cm}^{-3}$. As n increases, the traps are filled by carriers, and radiative bimolecular recombination becomes significant (Figure 2B,C). Therefore, achieving efficient radiative recombination in bulk perovskites requires high n and well-passivated traps; achieving these conditions is a challenging task for low n LED operating conditions.

In contrast, in nanocrystalline perovskites, the charge carriers are confined within small grains, so the dominant radiative recombination mechanism can change to excitonic recombination. The PLQY of radiative recombination in nanocrystalline perovskites can be calculated as:^[29,30]

$$\eta(n) = \frac{k_1^r + k_2 n}{(k_1^r + k_1^{nr}) + k_2 n + k_3 n^2} \quad (\text{in nanocrystalline perovskite}) \quad (3)$$

Here monomolecular recombination rate k_1 divided into radiative excitonic recombination k_1^r and non-radiative trap assisted recombination k_1^{nr} . Even at low $n < 10^{16} \text{ cm}^{-3}$, radiative recombination can dominate if k_1^r is significantly larger than k_1^{nr} . Therefore, utilizing excitonic recombination in nanocrystalline perovskites is crucial for achieving high radiative recombination under typical LED operating conditions (Figure 2B,D).

However, several challenges still remain for nanocrystalline perovskites. Due to their small grain or particle size, the high surface-to-volume ratio induces surface defects, which increase the non-radiative recombination rate k_1^{nr} . Therefore, managing defects is crucial to achieving high quantum yield in nanocrystalline perovskites. Additionally, the non-radiative Auger recombination rate k_3 tends to be higher than in bulk 3D perovskites due to the smaller size and strong exciton binding energy (e.g., $k_3 \approx 10^{-27} \text{ cm}^6 \text{ s}^{-1}$ for Q2D perovskite using phenethylamine).^[30] This high k_3 results in an abrupt decrease in quantum yield at the high charge carrier density, and thus limits efficient operation at high brightness (Figure 2B,D).^[17,30] Overcoming these drawbacks remains a critical challenge for nanocrystalline PeLEDs. In the following sections, we investigate how different nanocrystalline structures increase radiative recombination processes and contribute to high-performance PeLEDs.

3. Nanoscale Polycrystalline Perovskites

3.1. Decrease the Grain Size of Polycrystalline Perovskites

Nanoscale PC perovskite was the first type of nanocrystalline perovskite to achieve bright and efficient PeLEDs.^[10,13,32,33] To fabricate PC perovskite, a precursor solution is prepared by dissolving the perovskite precursors in polar solvents such as dimethyl sulfoxide (DMSO) or dimethylformamide (DMF). The solution is then spin-coated onto a substrate. During the spin-coating

process, continuous solvent evaporation leads to supersaturation, initiating the nucleation of crystal seeds that grow into perovskite grains. However, without precise control over nucleation and growth, non-uniform, micrometer-sized grains (bulk 3D perovskites) often form. In bulk 3D perovskites, the low exciton binding energy causes excitons to easily dissociate into free carriers, leading to charge carrier trapping and non-radiative recombination, which reduces efficiency.^[10] Additionally, large and non-uniform film coverage can lead to severe leakage of current.^[34] Therefore, to achieve high-efficiency PeLEDs with PC perovskite, it is crucial to spatially confine the charge carrier, which can be achieved by reducing the grain size (Figure 3A and Table 2).

3.1.1. Crystallization Kinetics Engineering

To regulate grain size, the first strategy involves the engineering of a precursor solution. The perovskite precursor, dissolved in polar solvents, behaves as a colloidal solution, where the precursors are not fully dissolved but instead form clusters, such as PbX_2 -DMSO and PbX_2 -AX-DMSO.^[35] These clusters are typically sub-micrometer in size, and during nucleation following spin-coating, they act as nuclei, leading to the formation of large grains. Therefore, it is essential to prevent the formation of these microscale aggregated clusters.

One effective approach to achieving smaller grain sizes is by carefully controlling the aging time of the precursor, as colloid sizes tend to change over time. In the early stages of precursor preparation, large aggregates of clusters may form due to incomplete dissolution. To address this issue, perovskite solar cell precursors are typically aged for 6 hours to ensure complete dissolution. However, excessive aging can lead to the reformation of aggregates.^[36] For example, green PeLED precursors are often stirred overnight or aged for over seven days,^[37,38] while red PeLEDs may require only 1–2 h of stirring.^[39,40] Since the optimal aging time varies depending on the precursor composition, it should be carefully optimized for each specific formulation.

Additionally, modifying the precursor can help reduce aggregation. Adding an excess halide source can split larger aggregates into smaller colloids by forming high-valent halide-plumbates; for instance, adding HI or HBr has proven effective.^[41–44] Alternatively, additives such as caprylyl sulfobetaine and benzylamine, which strongly interact with the precursors, can significantly reduce colloid size, yielding small grains ($\approx 50 \text{ nm}$) and smoother film morphology.^[38]

Grain size can be further controlled by engineering the crystallization kinetics during coating. According to LaMer's nucleation theory,^[45] nucleation begins when the precursor concentration exceeds the critical supersaturation threshold. Subsequently, precursors diffuse to the nucleation site, so the crystal growth occurs until reaching equilibrium. To achieve small grain sizes with uniform and high-coverage film morphology, a high density of nucleation sites with restricted growth is required. Utilizing this theory, crystallization can be delayed by incorporating SnF_2 additives, which increase precursor solubility and the maximum saturation concentration.^[46] Nucleation initiated at higher concentrations suppresses crystal growth, leading to smaller, more homogeneous grains (Figure 3B). Additionally, polymeric additives such as poly(vinylpyrrolidone) (PVP)^[47] and poly(ethylene

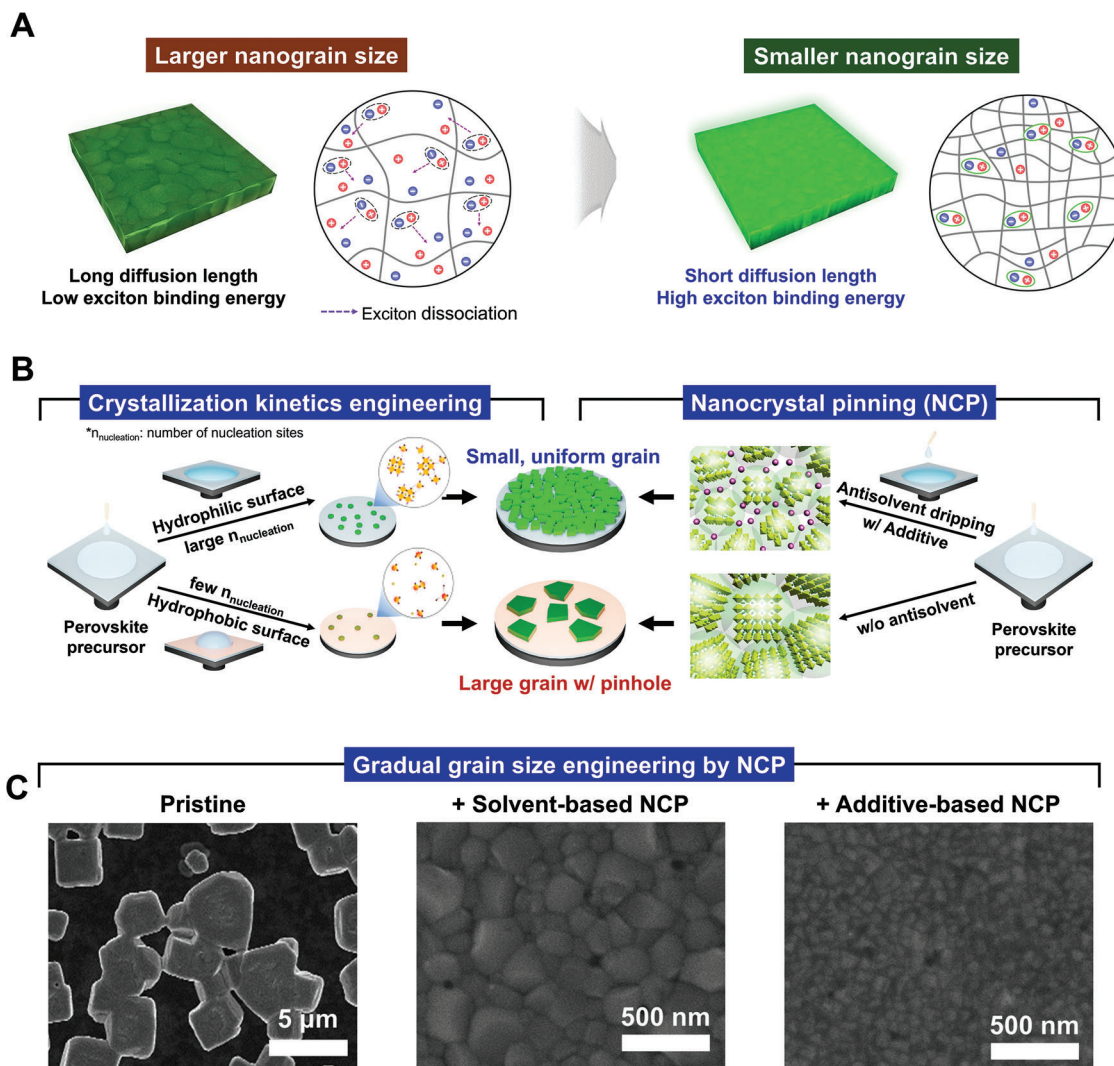


Figure 3. Grain size reduction of polycrystalline perovskites. A) Schematic illustration of charge carrier confinement effect depending on grain size.^[10] Copyright 2015, AAAS. In large grains, excitons dissociate into free carriers due to long diffusion lengths and low exciton binding energy, leading to low quantum yield. In contrast, reducing the grain size increases the exciton binding energy, spatially confines excitons within small nanograins, and enables high quantum yield. B) Schematic illustration of experimental approaches to reduce grain size; crystallization kinetics engineering (left) and crystal growth inhibition by nanocrystal pinning process (right). Reproduced with permission.^[46,58] Copyright 2022, American Chemical Society. Copyright 2017, Elsevier. C) SEM images of gradual grain size decrease depending on antisolvent-based nanocrystal pinning and additive-based nanocrystal pinning. Reproduced with permission.^[10] Copyright 2015, AAAS.

glycol) (PEO)^[48] have been introduced to prevent rapid crystal growth by interacting with perovskite precursors and interrupting precursor diffusion, further controlling grain size and film uniformity.

The underlying interface acts as a template that influences nucleation and growth, thus the material properties of the underlying layer must be carefully managed. In the case of poly(3,4-ethylenedioxythiophene) polystyrene sulfonate (PEDOT:PSS), slight solvation of the upper PSS layer by DMSO affects the crystallization process. To exploit this phenomenon, an alternative hole injection layer (HIL), Poly(styrenesulfonate)-grafted polyaniline (PSS-g-PANI), was introduced, which has a higher solubility of PSS in DMSO than PEDOT:PSS. This higher solubility results in the slow evaporation of DMSO, thereby significantly delaying

the crystallization of the perovskite. This slower crystallization, combined with the additive-based nanocrystal pinning (A-NCP) method, enables fine control of the perovskite film morphology, producing granular nanograins that more effectively confine excitons compared to the columnar grains typically formed when using PEDOT:PSS.^[49]

When using polymer hole transport layers (HTLs) (e.g., poly-TPD, TFB, and PVK), limited wettability is the primary factor to consider. The hydrophobic surface of polymer HTLs can lead to fewer nucleation sites, resulting in irregular, large grain sizes and insufficient surface coverage (Figure 3B).^[50,51] Therefore, polymer HTLs typically require an ultra-thin interlayer (< 5 nm) to convert the surface to hydrophilic and ensure proper nucleation. Common interlayers, such as poly(9,9-bis(3'-(N,N-

Table 2. Performance of state-of-the-art Polycrystalline PeLED.

Color	Perovskite Composition	EL Peak (FWHM)	Luminance/Radiance		EQE	Operational lifetime	Strategy	Refs.
Red	CsPbI _{3-x} Br _x	638 nm (30 nm)	9000 cd m ⁻²	17.8%	T _{50,Lum} ≈ 138.7 h @ 1 mA cm ⁻²	Metastable Phase Crystallization	[39]	
Green	(FA _{0.7} MA _{0.1} GA _{0.2}) _{0.87} Cs _{0.13} PbBr ₃	540 nm	470 000 cd m ⁻²	28.9%	T _{50,Lum} ≈ 31,858 h @ 100 cd m ⁻²	Defect Passivation in situ Core/shell; Reducing grain size to ~10 nm	[14]	
Green	CsFA _{0.15} PbBr ₃	521 nm (17.5 nm)	88 166 cd m ⁻²	28.4%	T _{50,Lum} ≈ 25.9 min @ 12025 cd m ⁻²	Molecular Additive	[82]	
Green	Cs _{0.5} MA _{0.4} FA _{0.1} PbBr ₃	526 nm	8500 cd m ⁻²	24.6%	T _{50,Lum} ≈ 23.8 min @ undefined	Interface Engineering	[74]	
Green	Cs _{0.5} MA _{0.4} FA _{0.1} PbBr ₃	530 nm (20 nm)	190 000 cd m ⁻²	22.3%	T _{50,Lum} ≈ 18.6 min @ 0.33 mA cm ⁻²	Molecular Additive	[37]	
Green	CsPbBr ₃ /Cs ₄ PbBr ₆	527 nm	10 050 cd m ⁻²	22.3%	T _{50,Lum} ≈ 59 h @ 130 cd m ⁻²	Core/shell Structure	[232]	
Green	Cs _{0.5} MA _{0.4} FA _{0.1} PbBr ₃	525 nm (20 nm)	83 306 cd m ⁻²	22.1%	T _{50,Lum} ≈ 36.1 min @ 0.33 mA cm ⁻²	Surface Treatment Molecular Additive	[233]	
Green	Cs _{0.5} MA _{0.4} FA _{0.1} PbBr ₃	527 nm	103 286 cd m ⁻²	22.06%	–	Molecular Additive	[234]	
Green	FAPbBr ₃	536 nm (21 nm)	120 000 cd m ⁻²	20%	T _{50,Lum} ≈ 26 min @ 10986 cd m ⁻²	Molecular Additive	[38]	
Green	FAPbBr ₃	532 nm	79 000 cd m ⁻²	18.04%	T _{50,Lum} ≈ 14.26 min @ 100 cd m ⁻²	Interface Engineering	[78]	
Blue	CsPbBr ₃	480 nm (21 nm) 465 nm (23 nm)	2910 cd m ⁻² 576 cd m ⁻²	17.9%, 10.3%	T _{50,Lum} ≈ 126 min @ 100 cd m ⁻² T _{50,Lum} ≈ 18 min @ 100 cd m ⁻²	Surface Ligand Engineering	[80]	
Blue	CsFA _{0.15} PbBr _x Cl _{3-x}	472 nm (14 nm) 478 nm (14 nm) 488 nm (16.5 nm) 496 nm (17 nm)	1516 cd m ⁻² 1534 cd m ⁻² 2038 cd m ⁻² 18 480 cd m ⁻²	11.1%, 17.5%, 21.6%, 24.4%	T _{50,Lum} ≈ 320s @ 95 cd cm ⁻² T _{50,Lum} ≈ 300s @ 129 cd cm ⁻² T _{50,Lum} ≈ 60s @ 778 cd cm ⁻² T _{50,Lum} ≈ 173s @ 1861 cd cm ⁻²	Molecular Additive	[82]	
Blue	FA _{0.2} Cs _{1.2} Rb _{0.1} PbBr _x Cl _{3-x}	478 nm (18 nm) 487 nm (18 nm)	8136 cd m ⁻² 18748 cd m ⁻²	10.3%, 13.6%	–	Interface Engineering	[235]	
Blue	CsPbBr _{1.5} Cl _{1.5}	464 nm (21 nm)	2180 cd m ⁻²	9.8%	T _{50,Lum} ≈ 23 min @ 100 cd cm ⁻²	Molecular Additive	[81]	
Blue	CsPbBrCl ₂	461 nm (15.4 nm)	1978 cd m ⁻²	5.68%	T _{50,Lum} ≈ 9 min @ 10 cd cm ⁻²	Surface Ligand Engineering	[236]	
NIR	Cs _{0.15} FA _{1.8} PbI ₃	793 nm (37 nm)	110 W sr ⁻¹ m ⁻²	24.3%	T _{50,Lum} ≈ 1,125 h @ 5 mA cm ⁻² T _{50,Lum} ≈ 84.4 h @ 100 mA cm ⁻²	Molecular Additive	[237]	
NIR	FAPbI ₃	810 nm	600 W sr ⁻¹ m ⁻²	23.6%	T _{50,Lum} ≈ 1,774 h @ 20 mA cm ⁻² T _{50,Lum} ≈ 256 h @ 100 mA cm ⁻²	Molecular Additive	[238]	
NIR	FAPbI ₃	785 nm	1593 W sr ⁻¹ m ⁻²	23.2%	T _{50,Lum} ≈ 227 h @ 100 mA cm ⁻²	Molecular Additive	[239]	
NIR	FAPbI ₃	800 nm	158 W sr ⁻¹ m ⁻²	22.8%	T _{50,Lum} ≈ 11,539 h @ 5.0 mA cm ⁻² T _{50,Lum} ≈ 32,675 h @ 3.2 mA cm ⁻²	Molecular additive	[70]	
NIR	FA _x Cs _{1-x} PbI ₃	789 nm (42 nm)	148.5 W sr ⁻¹ m ⁻²	21.3	T _{50,Lum} ≈ 190 h @ 20 mA cm ⁻²	Compositional Engineering	[60]	

dimethyl)-N-ethylammonium-propyl-2,7-fluorene)-alt-2,7-(9,9-dioctylfluorene))dibromide (PFN-Br),^[51] PVP,^[52–54] LiF,^[39,55–57] enhance the wettability, allowing the polar precursor to spread evenly and thus avoid these problems.

3.1.2. Inhibition of Crystal Growth by Nanocrystal Pinning

DMSO and DMF, the solvents used for perovskite precursors, have low volatility, allowing for slow evaporation during the spin-coating process. This slow evaporation provides sufficient time for precursors to diffuse to nucleation sites, promoting the growth of larger crystals. Moreover, these solvents interact strongly with the precursor and remain even after the spin-coating. These remaining solvents further facilitate the grain growth during the annealing process.

To address this issue, an excess amount of non-polar solvent can be introduced during the spin-coating process. This

technique, known as NCP, is effective for producing uniform and smaller grains.^[10] When a volatile non-polar solvent (e.g., chloroform),^[10] distinct from the anti-solvent typically used in perovskite solar cells, is applied to the perovskite precursor film during spin-coating, it causes rapid supersaturation of the precursor, resulting in the formation of a large number of nucleation sites across the surface. Consequently, a uniform and small grain-sized PC perovskite can be achieved (Figure 3B).

Applying A-NCP, which uses non-polar solvents with dissolved additives, can further inhibit crystal growth (Figure 3C). 1,3,5-tris(1-phenyl-1H-benzimidazol-2-yl)benzene (TPBi) has been used as an additive in chloroform reducing the average grain size from 171.04 to 86.67 nm.^[10,58] During the spin-coating process, TPBi intercalates between the grains, pinning the perovskite grain growth. MAPbBr₃ with A-NCP showed increased PL intensity as TPBi concentration increased, due to enhanced exciton confinement from smaller grain sizes and reduced defect density at grain boundaries. In later research,

TPBi was shown to suppress dynamic disorder in the perovskite lattice, facilitating radiative recombination.^[6] Additionally, TPBi, an electron-transporting organic molecule, can gradually cover the grain boundaries and top surface during A-NCP, enhancing electron injection into the perovskite layer. Thus, the multifunctional A-NCP with TPBi reduces grain size, suppresses dynamic disorder to enhance radiative recombination, and improves electron injection (Figure 3C).^[58] Similarly, the use of 2,4,6-tris[3-(diphenylphosphinyl)phenyl]-1,3,5-triazine (PO-T2T), which contains P=O bonds that can coordinate with Pb²⁺, can decrease grain size and passivate defects, and thereby increase radiative recombination.^[9]

3.2. Defect Management of Polycrystalline Perovskites

Although reducing grain size is crucial to overcoming the intrinsically low exciton binding energy and long diffusion length of bulk 3D perovskites, the increased surface-to-volume ratio can lead to the formation of defects at grain boundaries. These defects can trap carriers and induce non-radiative recombination, which competes with both excitonic and bimolecular radiative recombination. To suppress defect formation, several strategies can be employed: 1) A-site cation alloying can prevent defect formation and increase the activation energy of halide migration. 2) Stoichiometric engineering of A-site cation can prevent the formation of metallic Pb and undesirable phases, which induce non-radiative recombination. 3) The molecular passivator can be designed to minimize the number of defect sites to achieve high device efficiency and stability. 4) Modifying the interface and charge transport layer (CTL) can prevent exciton quenching and ensure charge balance.

3.2.1. A-Site Cation Alloying

A-site cations occupy the cuboctahedral sites within the perovskite lattice, balancing the negative charge of the [BX₆]⁴⁻ octahedra and stabilizing the crystal structure. Recent studies have increasingly focused on A-site cation alloying to enhance device efficiency and stability by suppressing ion migration. Ion migration, typically for halide anions, leads to the formation of halide vacancies or induces halide segregation. A-site cation alloying suppresses halide ion migration in two ways.

First, A-site cation alloying enhances crystallinity and reduces defects in the perovskite lattice, which can serve as pathways for ion migration.^[59] In a study of FA_{1-x}Cs_xPbBr₃, when x = 0.1, the PLQY increased by 28.3%, compared to 20.6% in pristine FAPbBr₃. PL lifetime also increased, indicating a reduction in defect density.^[59] Similarly in FAPbI₃, alloying with 15% Cs prevented interfacial decomposition and increased the PLQY from < 60% to 77.9%. Device stability was also significantly improved, with T₅₀ increasing from ≈38.4 h to 190.1 h.^[60]

Second, A-site cation alloying induces local lattice distortions, increasing the activation energy for ion migration. For example, doping with A-site cations such as Cs⁺ or MA⁺ into FAPbI₃, induces lattice contraction at the surface, which impedes ion diffusion along grain boundaries. For Cs_{0.05}(FA_{0.83}MA_{0.17})_{0.95}PbI₃, where 5% Cs⁺ was introduced, the activation energy for halide

anion diffusion increased significantly from 0.37 to 0.53 eV.^[61] Similarly, when 5% of Rb⁺ and Cs⁺ cations were doped into MAPbI₃, the activation energy increased from 0.4 to 0.47 and 0.48 eV, respectively.^[62] In CsPb(Br/Cl)₃, substituting Cs into larger A-site cations of methylenediammonium (MDA⁺) showed an increase in activation energy from 0.41 eV (single cation perovskite) to 0.86 eV, resulting in more stable electroluminescence (EL) in blue PeLEDs.^[63] Therefore, A-site cation alloying is an effective strategy to reduce defect density and hinder halide migration. Recent studies have also adopted quadruple cation alloying (FA/MA/GA/Cs) to achieve highly efficient and stable PeLEDs.^[14]

3.2.2. Stoichiometric Engineering of A-Site Cation

When forming ABX₃ perovskite crystals, the ideal stoichiometric ratio of AX to BX₂ compounds in precursor solution is 1:1. However, rapid film formation can cause an accumulation of lead precursors in localized areas, resulting in the formation of metallic lead (Pb⁰).^[10] Pb⁰ acts as a defect that leads to exciton quenching, promoting non-radiative recombination and significantly reducing PL intensity. Early PeLED research showed that increasing the MABr/PbBr₂ ratio to 1.05 suppressed the formation of metallic Pb⁰, resulting in EQE_{max} 8.53%, which marked a breakthrough in PeLED efficiency in 2015 (Figure 4A).^[10] More recently, a slightly higher AX/PbX₂ ratio of 1.15 with the quadruple cation has contributed to a further increase EQE_{max} to 28.9%.^[14] Excess A-site cations also provide a passivation effect at the grain boundary.^[64] When MABr is dissolved in an equal molar ratio to CsPbBr₃ precursor, MABr, which is more soluble in DMSO than CsBr, preferentially locates on the surface of CsPbBr₃ crystals. The MABr layer acts as a passivation layer that reduces non-radiative defects and achieves an EQE_{max} of 20.3%.^[64]

Additionally, when the ionic radius of an A-site cation is much smaller than halide ions, such as CsPbBr₃, CsPbI₃, or FAPbI₃, the potential formation of a non-emissive secondary phase should be considered. For instance, when Cs⁺ is the main A-site cation, the stoichiometry must be controlled to minimize the formation of Cs₄PbBr₆.^[65] The Cs₄PbBr₆ phase is thermodynamically favored with excess CsBr, leading to a non-emissive wide bandgap (3.9 eV) phase and insulating characteristics that hinder charge transport. To fully suppress the Cs₄PbBr₆ phase and obtain 3D CsPbBr₃ perovskite, a Cs:Pb ratio of 1.0 to 1.2 is recommended.^[66] In perovskites like CsPbI₃ or FAPbI₃, these perovskites can exist in two phases: the α-phase, which exhibits efficient radiative recombination, and the δ-phase (or yellow phase), which has isolated PbI₆ octahedra and poor emission properties.^[67] The use of excess CsI or FAI helps suppress the formation of the δ-phase by promoting the formation of corner-shared [PbI₃]⁻ intermediates rather than edge-shared PbI₂ intermediates, and thereby lowers the energy barrier for α-phase formation.^[68] Therefore, maintaining an optimal stoichiometric ratio is therefore crucial to increase the phase stability and efficiency of perovskites.

3.2.3. Design of Molecular Passivator

The realization of highly efficient and stable PeLEDs requires minimization of the number of defects in the perovskite film.

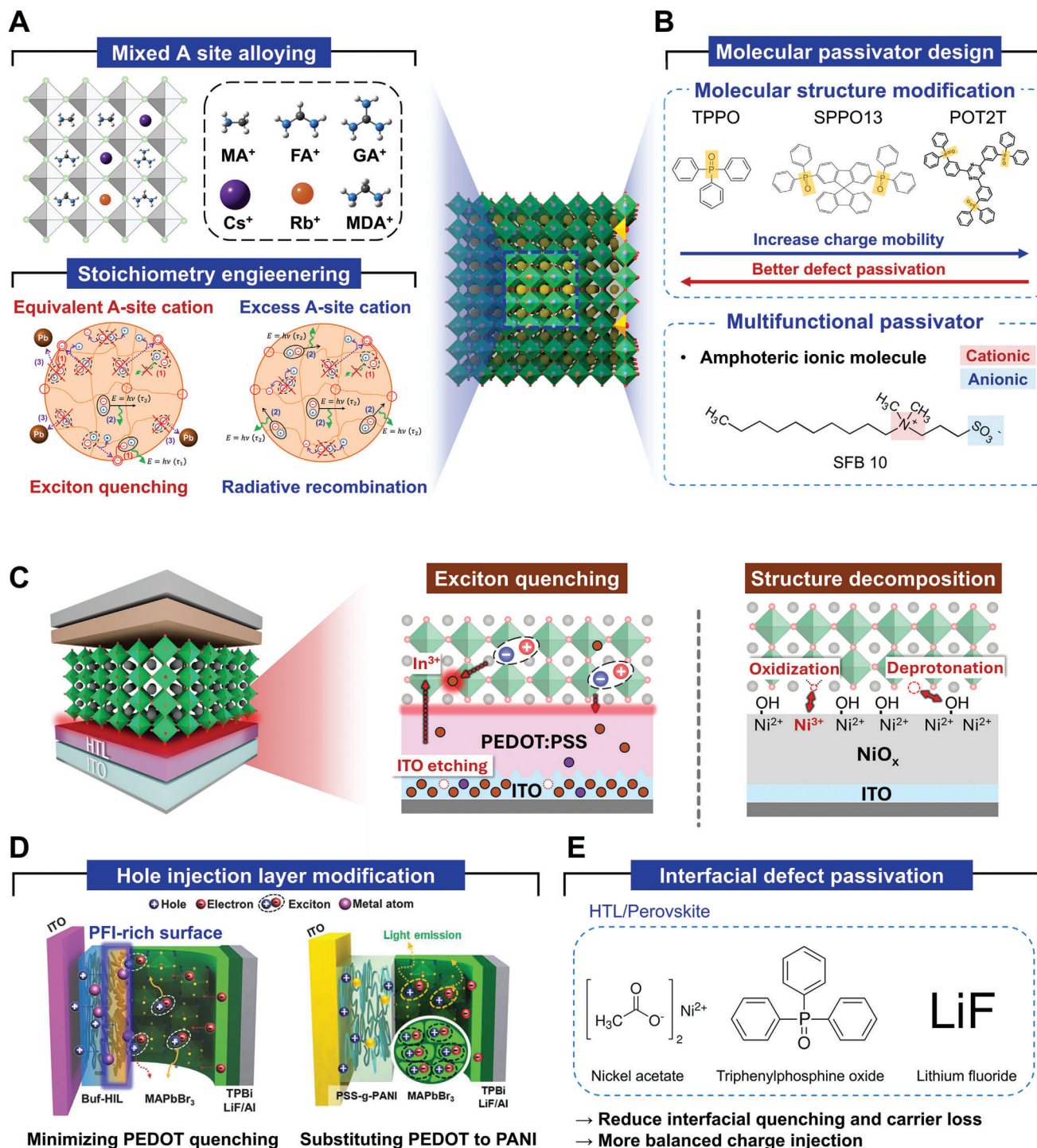


Figure 4. Defect management strategies of polycrystalline perovskites. A) Schematic illustration of defect management by mixed A-site alloying and stoichiometry engineering. Reproduced with permission.^[10] Copyright 2015, AAAS. B) Chemical structure of molecular passivator by molecular structure engineering (top) and multifunctional group modification (bottom). C) Schematic illustration of detrimental effects of PEDOT:PSS and NiO_x layer to perovskite. Acidic PEDOT:PSS etches the ITO electrode, allowing metallic species from the etched ITO to diffuse into the perovskite layer, causing exciton quenching. Additionally, highly conductive PEDOT:PSS induces interfacial quenching with the perovskite. Interfacial reactions with NiO_x result in the oxidation or deprotonation of perovskite components, degrading the crystal structure. D) Hole injection layer modification by PFI-enriched surface suppresses exciton quenching at the interface (left). Reproduced with permission.^[72] Copyright 2017, WILEY-VCH. Substituting PEDOT into PANI to prevent the ITO etching (right). Reproduced with permission.^[49] Copyright 2018, WILEY-VCH. E) Surface modifying materials at perovskite-HTL interface.

They include anionic halide vacancies and cationic uncoordinated Pb^{2+} . Ionic termination of the perovskite surface also should be neutralized to hinder ion migration through the vacancies. To overcome the defective nature of perovskite, various molecular passivators have been used.

Lewis-base molecular passivators can bind strongly to exposed Pb cations. Among these, the P=O bond is effective for surface passivation.^[69] Triphenylphosphine oxide (TPPO), which contains three phenyl rings attached to a P=O bond, can be applied during the NCP process (Figure 4B).^[69] However, TPPO is an insulating single-molecule material, so the use of excess TPPO as a passivator is not appropriate for low-voltage and high-luminance devices. This drawback can be mitigated by incorporating conductive molecular structures that have P=O functional groups.^[37] 2,7-bis(diphenylphosphoryl)-9,9'-spirobifluorene (SPPO13) consists of two P=O bonds connected by a spirobifluorene structure; the high electron mobility of SPPO13 increases charge injection. (Figure 4B). Due to the bulkier nature of SPPO13 compared to TPPO, the defect density was slightly higher than TPPO, but a significantly increased luminance of 190 000 cd m^{-2} was reported through efficient charge injection and moderate defect passivation.^[37]

To simultaneously block both cationic and anionic defects, amphoteric ionic molecules can be utilized.^[70] Sulfobetaine 10 (SFB10), which possesses both a positively charged ammonium moiety and a negatively charged sulfonate moiety, acts as a dipolar stabilizer (Figure 4B). By interacting with the precursors during crystal formation, SFB10 slows the crystallization and leads to the formation of uniform α -FAPbI₃. SFB10 concentrates at grain boundaries after phase formation; the ammonium moiety strongly binds with I^- ions, and the sulfonate ion binds with Pb^{2+} ions. This defect management strategy using SFB10 yielded near-infrared (NIR) PeLEDs with a $T_{50} \approx 32\,675$ h at 3.2 mA cm^{-2} .^[70]

Another effective molecular passivator is 1,8-octanedithiol (ODT), which acts as a multifunctional agent for comprehensive suppression of non-radiative recombination.^[71] ODT serves as a Lewis-base passivator for uncoordinated Pb^{2+} ions, suppressing exciton quenching at grain boundaries. Additionally, ODT surrounds the nanograins of perovskite, providing spatial confinement of excitons and concentrates at the interface with the HIL, thereby preventing exciton quenching at the perovskite-HIL interface. This defect passivation strategy using ODT has been shown to significantly improve EQE_{max} by 23.46% in single-cation PC PeLEDs.^[71]

3.2.4. Interface and Charge Transport Layer Engineering

In the PeLEDs that perovskite stacked between the HTL and electron-transport layer (ETL), interfaces are susceptible to defect formation owing to a mismatch of the lattice constant, and chemical reactivity. Therefore, interfacial defect sites must be passivated to prevent non-radiative recombination.

PEDOT:PSS is an excellent hole-injecting polymer, which is both transparent and conductive. However, excitons are easily quenched due to their strong acidity and high conductivity (Figure 4C). This problem can be overcome by mixing PEDOT:PSS with a perfluorinated polymeric acid, tetrafluoroethylene-perfluoro-3,6-dioxo-4-methyl-7-octene-

sulfonic acid copolymer (PFI), which has a deep work function and low conductivity.^[32] PFI has lower surface energy than PEDOT:PSS, so when PEDOT:PSS-PFI blend is spin-coated on a hydrophilic substrate, a vertical gradient of PFI develops in the layer, with PFI content increasing from the substrate to the top surface. The high PFI content at the surface decreases surface quenching induced by PEDOT and forms ohmic contact at the perovskite surface, thereby increasing hole injection. (Figure 4D).^[32,72] PSS-g-PANI has also been used as an alternative HIL of PEDOT:PSS. The polyaniline (PANI) moiety replaces the PEDOT, forming PSS-g-PANI which has a lower acidity of pH 5.4, compared to the PEDOT:PSS of pH 2.0.^[49] When acidic PEDOT:PSS spin-coated on ITO, it can etch ITO, generating metallic species that diffuse into the perovskite and cause exciton quenching. In contrast, PSS-g-PANI, with its lower acidity, suppresses the etching of ITO, effectively preventing the exciton quenching induced by metallic species (Figure 4D).^[49]

Nickel oxide (NiO_x) is commonly used inorganic HTL in PeLEDs, but it has several drawbacks. First, the discrepancy in lattice constants between NiO_x and perovskite can lead to microstrain in perovskite,^[73] or a weak connection at the NiO_x /perovskite can result in the formation of disconnected cavities.^[74] Additionally, the oxide surface is chemically reactive, which can dissociate the perovskite crystal structure and deprotonate the organic A-site cations (Figure 4C).^[75] To address these issues, the insertion of a thin interlayer on NiO_x using triphenylphosphine oxide (TPPO)^[76] or nickel acetate ($\text{Ni}(\text{OAc})_2$)^[74] has been introduced. This interlayer prevents direct contact between the perovskite with NiO_x thereby suppressing interfacial quenching and unwanted chemical reaction (Figure 4E).^[74]

In contrast, exciton quenching at the interface between the ETL and the perovskite is rarely reported, particularly when thermally deposited organic molecules are used. Instead, the device's efficiency and performance are more influenced by the electrical characteristics of these organic molecules. For example, while TPBi has been widely used since the early stages of PeLED development,^[10] the electron-transporting molecule with higher electron transport capability such as PO-T2T or 2-[4-(9,10-Di-naphthalen-2-yl-anthracen-2-yl)-phenyl]-1-phenyl-1H-benzimidazole (ZADN)^[14,77] has been adopted to achieve more efficient and stable PeLEDs. Additionally, modifying the structure of electron-transporting organic molecules by incorporating stronger nucleophilic groups has demonstrated further defect passivation on the perovskite surface. An example is 4,6-Bis(3,5-di(pyridin-3-yl)phenyl)-2-(pyridin-3-yl)pyrimidine (B3PyPPM), where the central methyl group of 4,6-Bis(3,5-di(pyridin-3-yl)phenyl)-2-methylpyrimidine (B3PyMPPM) is replaced with a phenyl group. Compared to B3PyMPPM, B3PyPPM exhibits a more negative electric field distribution within the molecule, enabling stronger coordination with surface Pb^{2+} vacancies. This modification increased the PLQY from 76.4% in B3PyMPPM-deposited perovskite films to 84.18% in B3PyPPM-deposited films.^[78]

3.3. In Situ Perovskite Nanocrystal

Despite advancements in reducing grain size and implementing passivation strategies for PC perovskites, further reducing the

grain size to 10–20 nm to form in situ perovskite nanocrystals (in situ PNCs) remains a key challenge. Achieving this would increase exciton binding energy, facilitating radiative excitonic recombination and ultimately enhancing PeLED efficiency. Two main strategies have been proposed for fabricating in situ PNCs: 1) splitting grains by using ligands that interact with grain boundaries and within the crystal,^[79] and 2) suppressing grain growth by using molecular additives.^[80–83]

3.3.1. In Situ Core/Shell Perovskite Nanocrystal with Grain Splitting

Initial research used a 3D/2D hybrid perovskite structure to achieve nano-sized grains in PC perovskite.^[79] The addition of a small amount of the large ammonium cation, benzylamine, to the precursor solution yielded a 3D/2D hybrid perovskite composed of nanograins. In the precursor, benzylamine is protonated by MA⁺, and converted to benzyl ammonium cation. These large benzyl ammonium cations preferentially form a 2D phase on the crystal surface, and thereby restrict grain growth and promote the formation of nano-sized grains; this restriction is beneficial for efficient exciton confinement. Additionally, the 2D phases at the grain boundaries effectively passivate defects and suppress ion migration between grains. As a result, the presence of these 2D phases on the surface both increased exciton binding energy and significantly improved the operational stability of PeLEDs to T₅₀ ≈ 14 h (L₀ = 100 cd m⁻²), compared to T₅₀ of ≈ 38 min in 3D PeLEDs. 3D PeLEDs exhibit an “overshoot” phenomenon, in which luminance increases by ≈ 40% beyond the initial value; this phenomenon is indicative of ion migration and internal electric field formation. Notably, the overshooting was suppressed in the 3D/2D hybrid PeLEDs, where ion migration was effectively blocked at the interface.^[79]

A state-of-the-art approach for reducing grain size to the nanometer-scale is the formation of an in situ core/shell PNC structure, which effectively decreases grain sizes to ≈ 10 nm by splitting grain at defect sites (Figure 5A).^[14] This method also passivates both inter- and intra-grain defects. A key step in this process involves coating benzyl phosphonic acid (BPA) solution on the perovskite film. In a weak polar solvent, BPA exists in its anionic form and forms strong covalent bonds with uncoordinated Pb²⁺ on the surface. This post-treatment reduced the average grain size from 123 nm to 10 nm, and thus significantly increased the exciton binding energy from 90 to 220 meV (Figure 5A). The introduction of short ligands facilitated both high exciton confinement and effective defect passivation and yielded an EQE of 28.9% and a maximum luminance of 473 990 cd m⁻² (Figure 5B). This structure also achieved a high luminance of 10 000 cd m⁻² at a low voltage of 2.7 V and a T₅₀ = 520 h at 1000 cd m⁻², with an estimated T₅₀ of 31 858 h at 100 cd m⁻², effectively overcoming the short operation lifetime PeLEDs.^[14]

3.3.2. Growth Regulation by Molecular Additives

Another approach for fabricating in situ PNCs involves directly synthesizing them on substrates by restricting crystal growth with additives that strongly coordinate with perovskite intermediates. In typical PC, crystal growth coincides with nucleation

during the spin-coating stage, so rapid crystallization and growth lead to the formation of large and uneven grains. In contrast, additives that strongly coordinate with perovskite precursors and intermediates suppress growth during spin-coating but allow controlled growth during subsequent thermal annealing. This regulated growth mechanism restrains the diffusion of intermediates and limits further growth.

Bulky phenethyl ammonium cations such as α -methylbenzylammonium (MBA) ligands, are utilized for this purpose. The α -methyl amine group in these cations binds to the perovskite surface, where it restricts grain growth and prevents the formation of 2D phases. The size of in situ grown PNCs can be tuned from bulk to quantum dots as small as 3.5 nm by adjusting the MBA concentration in the precursor solution. This process yielded a uniform, stable in situ PNC-LED that had a high EQE_{max} of 10.3% at pure-blue wavelength (465 nm) (Figure 5C).^[80] This method also applies to mixed-halide perovskites, in which 7 nm in situ PNCs had higher activation energy of ion migration (0.58 eV) than control samples (0.35 eV), and thereby increased phase stability and spectral stability during operation under voltage.^[81]

Similarly, δ -aminovaleric acid hydrobromide (δ -AVA-HBr) has bifunctional groups that effectively confine in situ PNCs to an average size of 6.8 nm. This treatment yielded a high exciton binding energy of 109 meV and an EQE_{max} of 22.5%.^[83] The 18-crown-6 molecule is a macrocyclic structure that includes strongly electron-donating oxygen atoms. It binds effectively to Pb²⁺ and A-site cations, and thereby slows the crystallization process and controls crystal growth to produce PNCs of 15.9 nm size. Synergistic additives such as *p*-fluorophenethylammonium bromide (*p*-FPEABr) and LiBr achieve EQE_{max} of 28.4% in green-emitting PeLEDs and 24.4%, 21.6%, 17.5%, and 11.1% in blue-emitting PeLEDs at wavelengths of 496, 488, 478, and 472 nm, respectively, depending on the Cl ratio (Figure 5C).^[82]

4. Quasi-2D Perovskite

The valuable attribute of Q2D perovskites is a self-assembled quantum-well structure, which was first reported for PeLEDs in 2016.^[11,84] For this reason, Q2D perovskites are regarded as highly promising materials for efficient PeLEDs. This quantum-well structure can be represented by the formula A'₂A_{n-1}B_nX_{3n+1}, where A' is an organic spacer cation, A is a monovalent cation, B is a divalent cation, and X is a halide anion. *n* is the number of [BX₆]⁴⁻ octahedral slabs, which are sandwiched between the terminating spacer cations and that determines the thickness of the layered structure (Figure 6A).^[85] We categorized Q2D phases based on the number of layers (*n*) as follows: 2D monolayer *n* = 1 phase, and small-*n* (*n* = 2 or 3) phases are classified as low-*n* phases (*n* = 1, 2 or 3); *n* = 4 or 5 phases as medium-*n* phases; and *n* ≥ 6 as high-*n* phases.^[86] In contrast, phases with *n* values exceeding 10 are more appropriately classified as nanoscale polycrystalline perovskites rather than Q2D perovskites.

Spacer cations on the surface act as dielectric layers that confine excitons, thereby forming quantum-well structures, a phenomenon known as the dielectric confinement effect.^[87,88] Due to these characteristics, Q2D perovskites have large exciton binding energies.^[89] The *n*-value determines the major physical

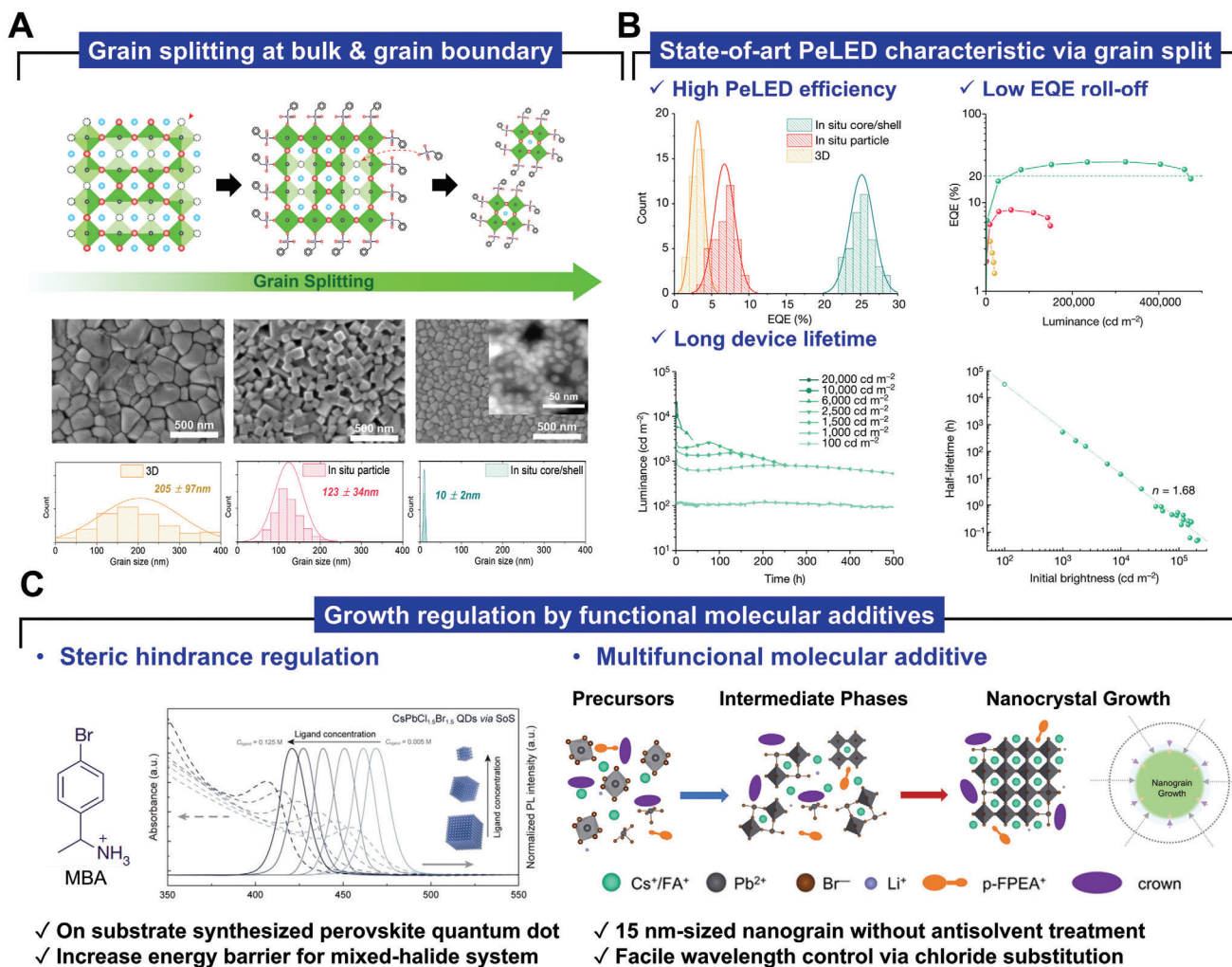


Figure 5. Representative strategies for in situ perovskite nanocrystals A) Schematic illustration of in situ core/shell PNC by grain splitting at bulk and grain boundary (top), SEM images, and grain size distribution (bottom). Reproduced with permission.^[14] Copyright 2022, Springer Nature. B) EQE, luminance, and device lifetime of PeLEDs on the basis of in situ core/shell PNC. Reproduced with permission.^[14] Copyright 2022, Springer Nature. C) Schematic illustration of grain growth regulation by functional additives. Steric hindrance regulation (left) and introduction of multifunctional molecular additive (right). Reproduced with permission.^[81,82] Copyright 2023, WILEY-VCH, Copyright 2024, WILEY-VCH.

and optical characteristics of Q2D perovskite by the quantum-confinement effect.^[90–92] Low-*n* phases, including the 2D monolayer (*n* = 1) and small-*n* phases (*n* = 2, 3) are strongly confined, so they have a large bandgap and large exciton binding energy. In contrast, medium-*n* (*n* = 4, 5) and high-*n* (*n* ≥ 6) phases can be regarded as weakly-confined structures, so they have lower bandgap and exciton binding energy than low-*n* phase Q2D perovskite.

Q2D perovskites are composed of multiple-quantum-wells that consist of various *n*-layered perovskite phases.^[11] If specific stoichiometry is targeted, such as $A'_2A_2B_3X_{10}$ for *n* = 3, the resulting perovskite film generally contains not only the *n* = 3 phase but also phases that have *n* = 1 or 2, and others that have *n* ≥ 4. This distribution of *n*-phases occurs because the formation energies and crystallization kinetics vary according to *n*, so a broad distribution of *n*-values develops in Q2D perovskites.^[93] This distribution of *n*-phases enables a photophysical phenomenon called

energy funneling, by which excitons are preferentially formed in the low-*n* phases due to their higher exciton binding energies than medium- or high-*n* phases (Figure 6A).^[84] These excitons then transfer along a gradient of energy levels to higher-*n* phases, which have lower bandgaps than lower-*n* phases. Ultimately, the excitons recombine in the high-*n* phases, which have progressively smaller bandgaps as *n* increases.

This energy-funneling process in Q2D perovskites facilitates highly efficient radiative recombination of excitons.^[84] However, for this process to be effective in increasing the PLQY, the energy funneling must occur rapidly. Slow energy transfer can lead to charge-carrier accumulation in low-*n* phases, where the carriers become susceptible to non-radiative trap-assisted recombination and Auger recombination, which reduces the PLQY (Figure 6B).^[94–96] Additionally, this inefficiency results in emissions from multiple-quantum-well energy gaps rather than the intended recombination in the targeted medium- or high-*n*

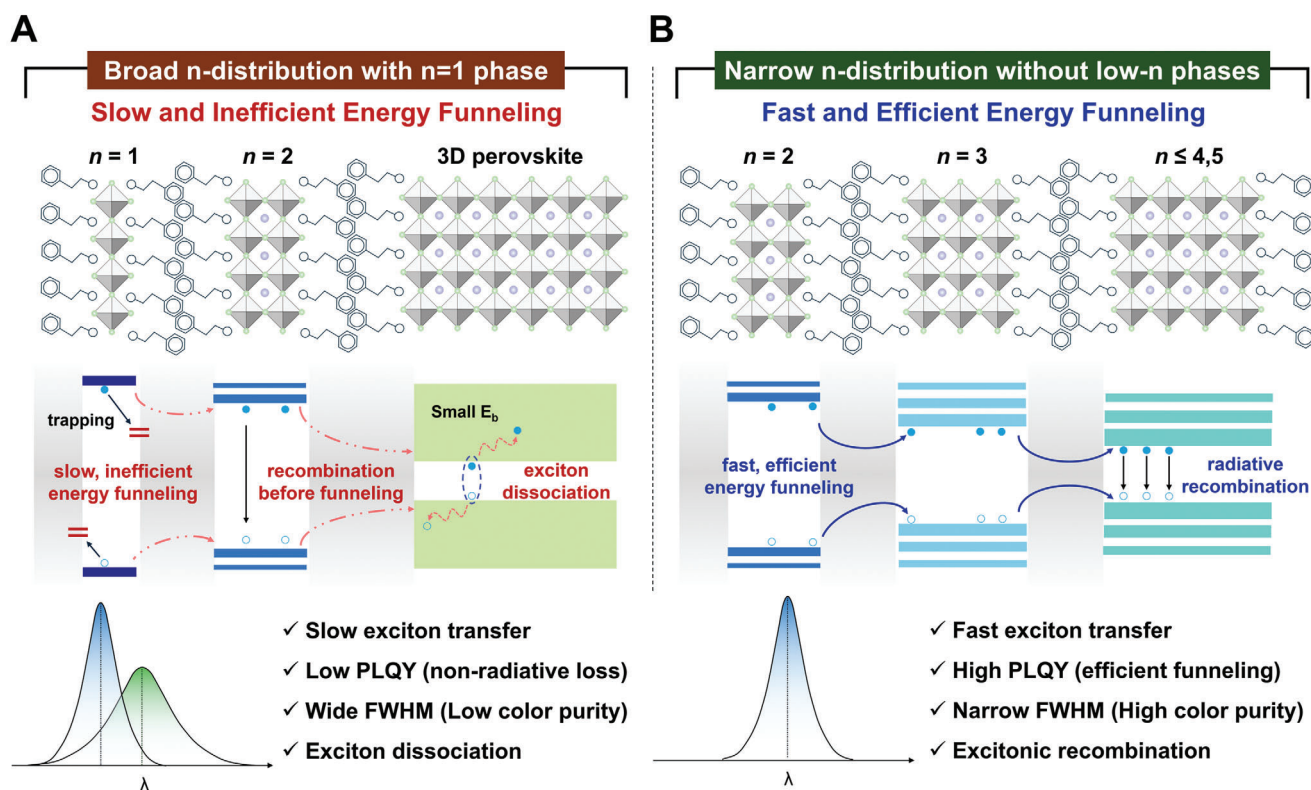


Figure 6. Schematic illustration of the characteristics of A) narrow n -distributed quasi-2D perovskite, demonstrating fast and efficient energy funneling, and B) broad n -distributed quasi-2D perovskite, demonstrating slow and inefficient energy funneling.

phase, the consequence is a broad emission spectrum with large FWHM and reduced color purity.^[94,97]

Given the relationship between energy funneling and n -distribution in Q2D perovskites, current advances have focused on controlling the distribution of n by methods such as engineering spacer cations and incorporating additives. Narrowing this distribution facilitates energy transfer. This section will discuss strategies to narrow the distribution of n -phases in Q2D perovskites, including 1) modulation of spacer cations, 2) control of nucleation and growth by using additives to increase energy funneling, and 3) strategies to enhance electrical property and operational stability to achieve efficient Q2D PeLEDs (Table 3).

4.1. Spacer Cation and n -Phase Modification

Narrowing the n -distribution is a promising approach to facilitate energy funneling in Q2D perovskites. Density functional theory (DFT) calculations indicate that the formation energy of low- n phases ($n = 1, 2, \text{ or } 3$) is more negative and thermodynamically stable compared to medium- or high- n phases that have $n \geq 4$. As a result, during the crystallization of Q2D perovskites, the formation of low- n -phases is favored during the early stages, whereas the formation of medium- or high- n phases is favored in later stages due to the depletion of spacer cations, which are largely consumed during the formation of low- n phases.^[97–99] These processes lead to the depopulation of targeted n phases and result

in a broad distribution of n -phases. Such a broad distribution fails to provide the ideal gradual energy-cascade and thus hinders efficient energy funneling toward the perovskite that has the smallest bandgap. In drastic cases, the appearance of the $n = \infty$ (3D) phase, which lacks sufficient exciton confinement, can further reduce the PLQY. To prevent the depopulation of n -phases and the excessive formation of low- n phases, the engineering of spacer cations is used to destabilize the formation of low- n phases.

From a thermodynamic perspective, formation energy is the energy gap between the perovskite components in the individual state and in the 2D layered perovskite structure state.^[93] More negative formation energy indicates the strong binding and facile spontaneous self-assembly of spacer cations; this condition is energetically favorable to form $n = 1$ or 2. Therefore, the formation energy of the $n = 1$ phase is a critical factor that must be decreased. For instance, phenethylamine (PEA) is a commonly used spacer cation that has planar benzene rings that stack as a result of π - π interactions. These interactions increase the magnitude of negative formation energy and therefore increase the favorability of $\text{PEA}_2\text{PbBr}_4$ ($n = 1$) over phases that have $n > 1$ (Figure 7A).

Therefore, for optimal Q2D PeLEDs, the formation energy of the phases must be finely tuned by the molecular design of spacer cations. The tuning can be achieved by controlling factors such as 1) the steric hindrance of the side chains, 2) the disruption of stacking interactions, and 3) the dipole moment of the spacer cation.

Table 3. Performance of state-of-the-art Q2D PeLED.

Color	Perovskite composition	EL peak (FWHM)	Luminance/radiance	EQE	Operational lifetime	Strategy	Refs.
Red	(PPT) ₂ FA ₂ Pb ₃ I ₁₀	700 nm	42 000 mW sr ⁻¹ m ⁻²	26.3%	T _{50,Lum} ≈ 2.8 h @ 12 mA cm ⁻²	Spacer Cation Engineering Phase Distribution Modulation	[107]
Red	(PPT) ₂ FA ₃ Pb ₄ (Br _{0.1} I _{0.9}) ₁₃	716 nm	33 000 mW sr ⁻¹ m ⁻²	26.2%	T _{50,EQE} ≈ 100 min @ 1 mA cm ⁻²	Spacer Cation Engineering Phase Distribution Modulation	[240]
Red	(<i>m</i> -FPEA _{0.6} NMA _{0.4}) ₂ CsPb ₂ I ₇	680 nm (34 nm)	1300 cd m ⁻²	25.8%	T _{50,Lum} ≈ 36 min @ 100 cd m ⁻²	Spacer Cation Engineering Phase Distribution Modulation	[106]
Red	(2-NMA _{0.4} PhBA _{0.6}) ₂ CsPb ₂ I ₇	639 nm	1300 cd m ⁻²	24.2%	T _{50,Lum} ≈ 115 min @ 100 cd m ⁻²	Defect Passivation	[241]
Red	(PEA _{0.5} NMA _{0.5}) ₂ CsPb ₂ I ₇	639 nm (45 nm)	2508 cd m ⁻²	21.8%	T _{50,Lum} ≈ 42 min @ 100 cd m ⁻²	Light Out-coupling	[242]
Red	(<i>p</i> -FPEA _{0.4} NMA _{0.6}) ₂ CsPb ₂ I ₇	682 nm (34 nm)	404 cd m ⁻²	21.8%	T _{50,Lum} ≈ 35 h @ 5 mA cm ⁻²	Defect Passivation Charge Transfer Engineering	[105]
Red	PEA ₂ CsPb ₂ I ₅	656 nm	6483 cd m ⁻²	20.7%	T _{50,Lum} ≈ 71 min @ 10 mA cm ⁻²	Defect Passivation Phase Distribution Modulation	[110]
Red	PEA ₂ Cs ₃ Pb ₄ (Br _{0.15} I _{0.85}) ₁₃	672 nm	2121 cd m ⁻²	19.6%	T _{50,Lum} ≈ 306 min @ 100 cd m ⁻²	Crystallization Kinetics Control	[243]
Green	PEA ₂ Cs ₄ Pb ₅ Br ₁₆	516 nm (20 nm)	11 370 cd m ⁻²	32.1%	T _{50,Lum} ≈ 3.56 h @ 100 cd m ⁻²	Light Out-coupling	[244]
Green	PEA ₂ FA ₂ Pb ₃ Br ₁₀	524 nm (30 nm)	39 393 cd m ⁻²	30.8%	T _{50,Lum} ≈ 100.6 min @ 100 cd m ⁻²	Light Out-coupling Charge Transport Engineering	[245]
Green	PEA ₂ FA ₃ Pb ₄ Br ₁₃	531 nm (22.1 nm)	147 872.8 cd m ⁻²	29.5%	T _{50,Lum} ≈ 18.67 h @ 12 000 cd m ⁻²	Phase Distribution Modulation Defect Passivation	[21]
Green	PEA ₂ (FA _{0.95} Cs _{0.05}) ₄ Pb ₅ Br ₁₆	532 nm	95 000 cd m ⁻²	26.2%	T _{50,Lum} ≈ 920 min @ 1000 cd m ⁻²	Suppression of Ion Migration	[246]
Green	PEA ₂ (Cs _{0.933} FA _{0.067}) ₃ Pb ₄ Br ₁₃	515 nm	83 561 cd m ⁻²	26.0%	–	Charge Injection Engineering	[247]
Green	PEA ₂ FA ₂ Pb ₃ Br ₁₀	530 nm (24 nm)	288 798 cd m ⁻²	25.9%	T _{50,Lum} ≈ 91.1 min @ 100 cd m ⁻²	Phase Distribution Modulation	[117]
Green	PEA ₂ Cs _{1.6} MA _{0.4} Pb ₃ Br ₁₀	517 nm (20 nm)	52 000 cd m ⁻²	25.6%	T _{50,Lum} ≈ 115 min @ 7200 cd m ⁻²	Phase Distribution Modulation Defect Passivation	[94]
Green	(PEA) ₂ FA ₄ Pb ₅ Br ₁₆	530 nm (22 nm)	16 000 cd m ⁻²	25.1%	–	Defect Passivation Charge Transfer Engineering	[248]
Green	PEA ₂ Cs ₄ Pb ₅ Br ₁₆	511.7 nm (21 nm)	73 000 cd m ⁻²	24.3%	T _{50,Lum} ≈ 35.5 min @ 100 cd m ⁻²	Defect Passivation	[249]
Green	PEA ₂ (FA _{0.87} Cs _{0.13}) ₂ Pb ₃ (Br _{0.97} Cl _{0.03}) ₁₀	530 nm	23 657 cd m ⁻²	23.9%	T _{50,Lum} ≈ 63 min @ 100 cd m ⁻²	Spacer Cation Engineering Phase Distribution Modulation	[96]
Blue	(PEA) ₂ Cs ₂ Pb ₃ (Br _{0.5} Cl _{0.5}) ₁₀	478 nm (21.1 nm)	590 cd m ⁻²	21.9%	T _{50,Lum} ≈ 10 min @ 100 cd m ⁻²	Phase Distribution Modulation Defect Passivation	[95]
Blue	PDA ₂ Cs ₂ Pb ₃ (Br _{0.77} Cl _{0.37}) ₁₀	472 nm (25 nm)	941 cd m ⁻²	17.5%	T _{50,Lum} ≈ 11.3 min @ 100 cd m ⁻²	Spacer Cation Engineering	[250]
Blue	<i>p</i> -FPEA ₂ (Cs _{0.9} FA _{0.1}) ₃ Pb ₄ (Br _{0.4} Cl _{0.6}) ₁₃	478 nm (22 nm)	547 cd m ⁻²	17.3%	T _{50,Lum} ≈ 5 min @ 1 mA cm ⁻²	Crystallization Kinetics Control	[251]
Sky-blue	<i>p</i> -FPEA ₂ Cs ₄ Pb ₅ (Br _{0.42} Cl _{0.58}) ₁₆	483 nm (25 nm)	1147 cd m ⁻²	18.7%	T _{50,Lum} ≈ 220 s @ 1 mA cm ⁻²	Defect Passivation Suppression of Ion Migration	[252]
Sky-blue	<i>p</i> -FPEA ₂ Cs ₄ Pb ₅ (Br _{0.42} Cl _{0.58}) ₁₆	488 nm	2708 cd m ⁻²	17.3%	T _{50,Lum} ≈ 5.6 min @ 2 mA cm ⁻²	Crystallization Kinetics Control	[253]
Sky-blue	PBA ₂ CsPb ₂ Br ₇	492 nm (25.9 nm)	10 142 cd m ⁻²	17.08%	T _{50,Lum} ≈ 16.8 min @ 4.5 V	Phase Distribution Modulation Charge Transport Engineering	[254]
Sky-blue	<i>p</i> -FPEA ₂ Cs ₇ Pb ₈ (Br _{0.5} Cl _{0.5}) ₂₅	485 nm (24.8 nm)	5740 cd m ⁻²	16.3%	T _{50,Lum} ≈ 23.62 min @ 1 mA cm ⁻²	Defect Passivation	[255]
Sky-blue	PEA ₂ (Cs _{0.7} EA _{0.3})Pb ₂ Br ₅	490 nm	2150 cd m ⁻²	15.6%	T _{50,Lum} ≈ 55.3 min @ 100 cd m ⁻²	Phase Distribution Modulation Crystallization Kinetics Control	[97]

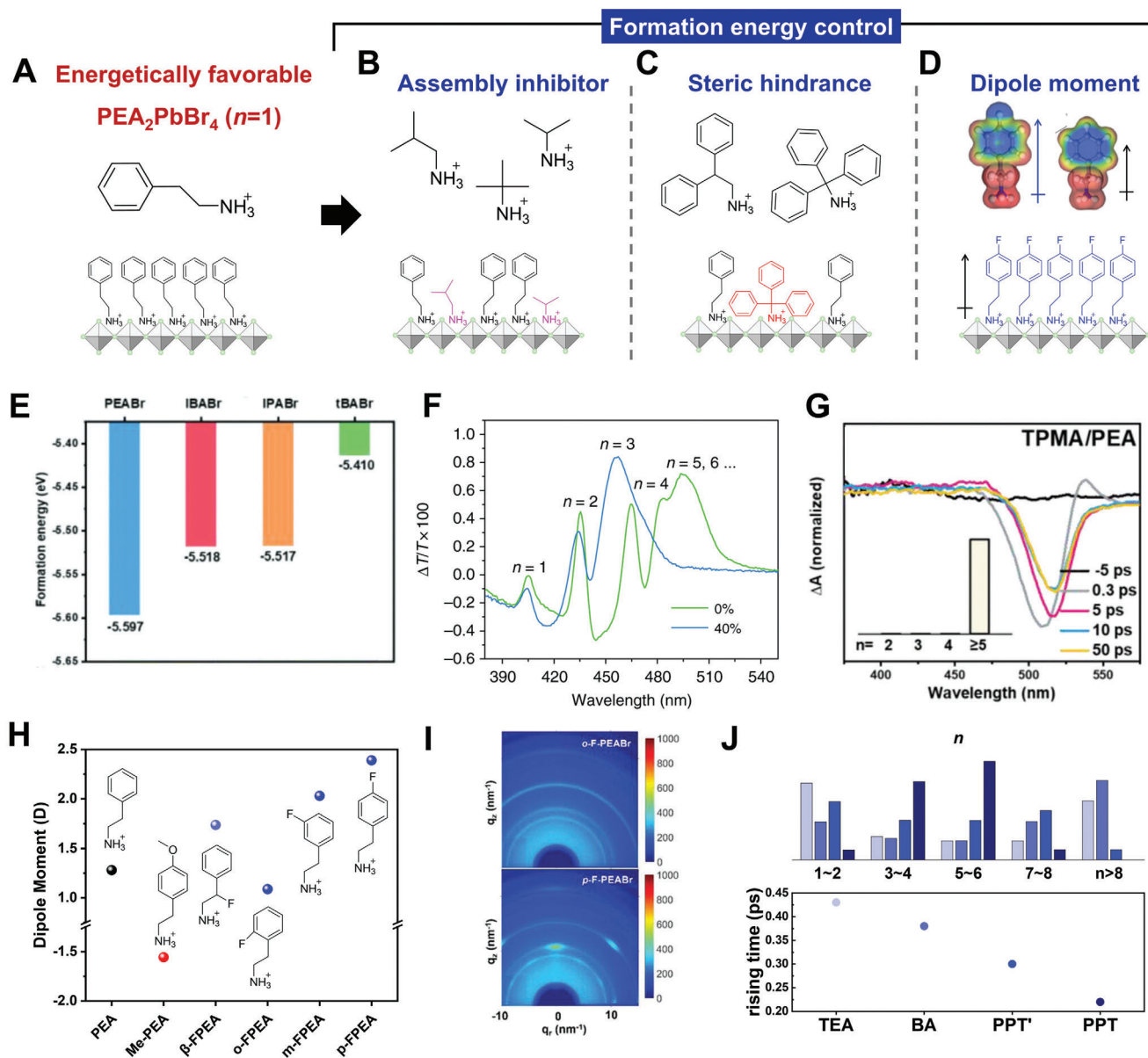


Figure 7. Schematic illustration of A) energetically favorable $n = 1$ perovskite and strategies to suppress the formation of $n = 1$ perovskite: B) the inhibition of self-assembly of spacer cation, C) the steric hindrance, and D) the dipole moment control. E) Formation energies as a function of the assembly ability of the tail group of the spacer cation. Reproduced with permission.^[96] Copyright 2023, WILEY-VCH. Transient absorption spectra of quasi-2D perovskite films F) with 0 and 40% IPABr and G) with TPMA/PEA at Δt from -5 ps to 50 ps with different spacer cation substitutions. Reproduced with permission.^[96] Copyright 2018, Springer Nature. Copyright 2023, WILEY-VCH. H) Dipole moments of PEA derivatives with electron-withdrawing and electron-donating groups.^[30,101–103] I) Grazing-incidence wide-angle X-ray scattering results for *o*-F-PEABr and *p*-F-PEABr.^[104] J) The n -distribution and transient absorption rise time with TEA, BA, PPT, and PPT'. Reproduced with permission.^[104] Copyright 2023, WILEY-VCH.

4.1.1. Self-Assembly and Steric Hindrance

The driving force for the formation of 2D perovskites is the stacking and self-assembly of spacer cations. Engineering the side chain of the spacer cation to induce weak assembly can make the formation energy less negative. One example of a weak-assembly spacer cation is a small alkyl cation without a benzene ring, such as isobutylamine (iBA), isopropylamine (IPA), or tert-butylamine (tBA) (Figure 7B). Their formation energies are reported to be

−5.518, −5.517, and −5.410 eV, respectively, which are all smaller than the formation energy of −5.597 eV of PEA. This difference indicates that low- n phase formation can be suppressed by using these small alkyl cations (Figure 7E).^[96] Partially replacing PEA with these small alkyl spacers effectively suppresses low- n phases by reducing the interactions between PEAs.

For instance, incorporating 40% IPABr into $\text{PEA}_2\text{PbBr}_4$ destabilizes the $n = 1$ phase, reducing the magnitude of its formation energy.^[98] PEA-only Q2D perovskite has a broad n -distribution

ranging from $n = 1$ to 6. Conversely, the IPA/PEA co-cation perovskite has primarily the $n = 2$ and 3 phases, with a reduced presence of $n = 1$ phase, and no phase that has $n \geq 5$ (Figure 7F). This distribution increases PLQY from 69% to 88% and yields desirable blue emission at 467 nm.^[98] Similar results have been observed when using iBAAs as a co-spacer with PEA. Replacing 40% of PEA with iBA nearly eliminates the $n = 1$ phase while significantly increasing the $n = 2$ and $n = 3$ phases. Consequently, PLQY increased from 21% to 45%, EQE_{max} increased ≈ 2.9 times to 7.84%, and L_{max} increased five times to 1130 cd m⁻² at 485 nm in blue PeLEDs.^[100] These small alkyl spacer cations effectively suppress $n = 1$ phases while maintaining $n = 2$ and $n = 3$ phases, so they are suitable for Q2D perovskites that require low- n phase, such as blue-emitting or red-emitting perovskites that require strong confinement.

When targeting a narrow n -distribution of high- n phases ($n \geq 6$) for green-emitting and deep-red-emitting perovskite, the use of a bulky spacer cation is effective, because its steric hindrance results in much weaker assembly ability than small alkyl spacers (Figure 7C). These non-planar or bulky spacer cations typically feature two or more benzene rings as side chains, and they hinder the ability of the spacer cations to assemble into a low- or medium- n phase. This characteristic allows them to effectively prevent the formation of highly confined low- n phases, and to favor the formation of high- n phases.

Spacer cations that have multiple benzene rings or highly-branched configurations, such as 3,3-diphenylpropylamine (DPPA), 2,2-diphenylethylamine (DPEA), and triphenylmethylamine (TPMA), have been introduced as bulky co-spacers with PEA for green-emitting Q2D perovskites.^[96] These bulky spacers suppress not only low- n phases but also medium- n phases and therefore favor a distribution composed mainly of phases that have $n \geq 5$ without forming 3D phases. This distribution facilitates rapid charge funneling (< 5 ps) into the lowest bandgap domains (Figure 7G). As a result, the incorporation of TPMA as a co-spacer cation leads to an increase in PLQY from 65.4% to 81.2% (TPMA/PEA co-spacer) and an increase in EQE_{max} from 20.3% to 23.9%.

4.1.2. Dipole Moment of Spacer Cation

The binding affinity of the spacer cation to the perovskite lattice also affects the formation energy of 2D perovskites. The dipole moment represents the separation of positive and negative charges within a molecule or ion, indicating the degree of polarity. In molecular systems, it can also be used as an indicator of interaction strength, such as binding affinity or intermolecular forces. (Figure 7D). An increased dipole moment of the ammonium spacer cation enhances the probability of bonding with uncoordinated Pb²⁺ ions, resulting in more negative formation energy of the $n = 1$ phase. Consequently, to achieve a narrow n -distribution, spacer cations with lower dipole moments are preferable.

One common strategy to modulate the dipole moment is to introduce electron-withdrawing groups like fluorine or electron-donating groups like methoxy group to spacer cation (Figure 7H).^[30,101–103] The position of fluorine on the phenyl ring affects the dipole moment because the delocalized π -electrons in

the ring can be easily attracted toward the electron-withdrawing group. The dipole moment increases from *o*-FPEA (1.09 D) to *m*-FPEA (2.03 D) to *p*-FPEA (2.39 D) (Figure 7H). Increasing dipole moments in the order of *o*-FPEA < PEA < *m*-FPEA < *p*-FPEA, show a corresponding trend in the negative formation energy, with values of -9.39 , -9.41 , -9.44 , and -9.63 eV, respectively.^[103] Consequently, low- n phase is formed more prominently with *p*-FPEA than with *o*-FPEA (Figure 7I).^[104] By tuning the dipole moment through molecular design, efficient energy funneling can be achieved by minimizing the low- n phase. *o*-FPEA achieves a higher PLQY (60%), than does for *p*-FPEA (35%). This comparison indicates that introducing spacer cations with lower dipole moments can increase radiative recombination by suppressing the development of low- n phases, which induce non-radiative recombination.^[103]

Furthermore, although *m*-FPEA and *p*-FPEA have more negative formation energies than *o*-FPEA and PEA, and therefore tend to form lower- n phases, their molecular configurations of *m*-FPEA and *p*-FPEA provide better surface passivation and stronger interaction with perovskite than PEA. As a result, combined with spacers such as 1-naphthylmethyl ammonium (NMA) that have less negative formation energy, *m*-FPEA is also widely adopted for the development of efficient PeLEDs.^[105,106]

4.1.3. Ion Diffusion Restriction Model

Blocking the ion diffusion between octahedral slab layers can suppress the formation of broad n -phase distribution. Since $n = 1$ phase is enthalpically stable and a mixture of n -phases is entropically favored, ion diffusion between octahedral slab layers causes phase segregation into low- n and high- n phases.^[107] Therefore, the incorporation of spacer cations that can block the interlayer ion diffusion can lead to a narrow n -distribution. For example spacer cations such as (2-(5-(3',5'-dimethyl-[1,1'-biphenyl]-4-yl)thiophen-2-yl)ethyl-1-ammonium (PPT') and (2-(5-(2,2'-dimethyl-[1,1'-biphenyl]-4-yl)thiophen-2-yl)ethyl-1-ammonium (PPT), which possess large π -conjugation and high steric hindrance, have good surface coverage so that the free energy barrier for I⁻ diffusion is significantly high.

Perovskites in which the spacer cation is butylammonium (BA) or thiophenylethylammonium (TEA) have the highest population of $n = 1$ and $n = 2$, and 3D phases ($n > 8$), with a few $n = 5$ and $n = 6$ phases due to their poor surface coverage. In contrast, when the spacer cation is PPT' or PPT, the proportion of $n = 5$ and $n = 6$ phases increases, particularly in PPT, which has very little $n = 1$ and $n = 2$ and none of the 3D phase (Figure 7J). This difference is attributed to the rotational angle between the phenyl rings, which is $\approx 20^\circ$ for PPT' and 90° for PPT, and this high steric hindrance effectively suppresses the ion diffusion between layers.^[107] In carrier dynamics, $\tau_{\text{rising time}}$, which represents the time constant of energy funneling within a multi-quantum-well structure, significantly decreases with PPT' and PPT (Figure 7J). As the n -distribution narrows and centers around $n = 5$ and $n = 6$, $\tau_{\text{rising time}}$ decreases; this change indicates efficient and rapid energy transfer from low- n phases to emissive high- n phases. This efficient energy transfer from the restriction of ion diffusion

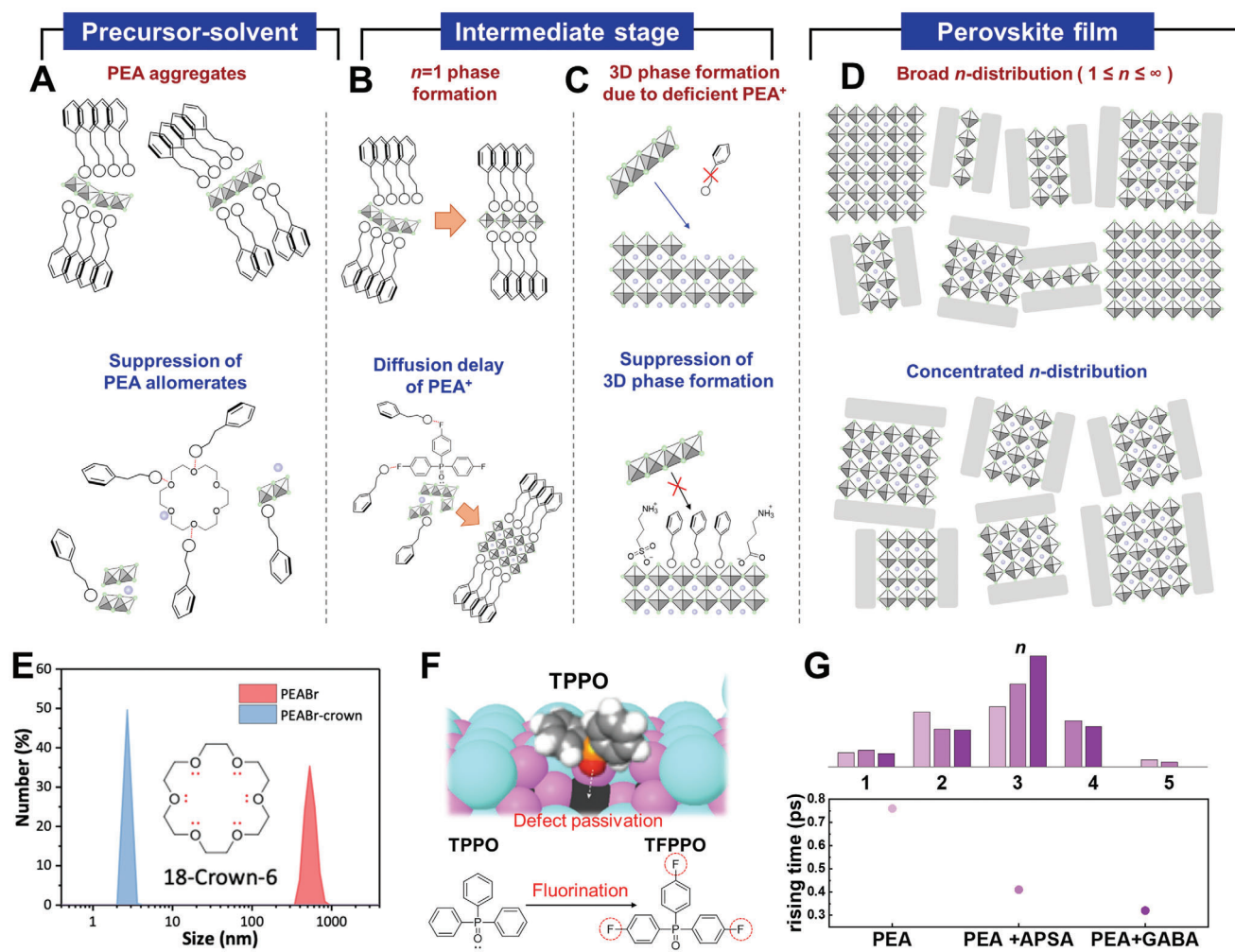


Figure 8. Schematic illustration of A) precursor-solvent complex, B, C) controlling the formation of 2D and 3D phase in intermediate stages, and D) resulting n -distribution with and without phase-regulating strategies. E) Dynamic light scattering results showing the size of PEA agglomerates with and without 18-Crown-6. Reproduced with permission.^[108] Copyright 2018, Springer Nature. F) Defect passivation of TPPO and the fluorination from TPPO to TFPPPO. Reproduced with permission.^[69] 2020, Springer Nature. G) The n -distribution and transient absorption rise time of pristine quasi-2D perovskite films, and those that include APSA or GABA. Reproduced with permission.^[97] Copyright 2022, WILEY-VCH.

contributes to the high PLQY of 94% and an EQE_{max} of 26.3% that have been achieved using PPT.^[107]

4.2. Nucleation and Growth Engineering by Additives

Incorporating additives into the precursor is another strategy to narrow the n -phase distribution of Q2D perovskites. Strong coordination of additives with precursors of Q2D perovskite modulates the nucleation and growth of Q2D perovskite. Additives that bind with the intermediates can suppress the excess growth of low- n phases and high- n phases and the consequent development of a narrow distribution of n (Figure 8D).

4.2.1. Nucleation Engineering

Agglomeration of PEA cations occurs due to the spontaneous π - π stacking of phenyl rings from precursor states (Figure 8A). Dur-

ing nucleation, PEA agglomerates serve as nuclei for the crystallization of low- n phases, and then the subsequent local deficiency of spacer cations promotes the formation of high- n phases.^[108] Thus, to suppress non-radiative recombination associated with defective 2D phase, large agglomeration of PEA in the precursor must be prevented. Additives that can directly interact with the -NH group in PEA disrupt the agglomeration of PEA in the precursor state, and thereby hinder the formation of $n = 1, 2$ phases.

Crown ethers, which contain C—O—C bonds, are representative additives that enable hydrogen bonding with the -NH group in PEA (Figure 8A). For instance, 18-crown-6 (1,4,7,10,13,16-hexaoxacyclooctadecane) and cryptands have been introduced to Q2D perovskites.^[108,109] These additives intercalate between PEA molecules, and thus effectively disrupt the agglomeration of PEA cations and decrease the size of the PEA agglomerate (Figure 8E).^[108] This disruption results in the elimination of the $n = 1$ phase. The use of 18-crown-6 in green Q2D PeLEDs leads to a 3 fold increase in PLQY to $\approx 70\%$ and a significant increment

of EQE_{max} from 1.25% to 15.5%. Similarly, cryptands, which also form hydrogen bonds with PEA, have been utilized in blue Q2D perovskites, in which they facilitate energy transfer in 1 ps from $n = 2$ to higher- n phases.^[109] In the absence of cryptand, excitons remain in $n = 1$ phase for over 10 ps, so non-radiative recombination occurs. Consequently, the incorporation of cryptand results in an increase of ≈ 2.5 times in PL intensity and an increase in EQE_{max} from 2.33% to 10.16%.

4.2.2. Growth Engineering: Additive as Diffusion Delay Agent

Delaying the diffusion rate of PEA toward the perovskite framework can be an effective strategy to suppress the formation of low- n phases (Figure 8B). TPPO is a promising candidate for this purpose; it inhibits the diffusion of spacer cations. Typically, TPPO is used as an additive for defect passivation due to the highly nucleophilic lone pair electrons of the P=O bond, which can effectively bind with uncoordinated Pb²⁺ ions and passivate defects (Figure 8F).^[69] Additionally, the oxygen in the P=O group can form hydrogen bonds with the -NH group of the spacer cation, and thereby regulate the diffusion of spacer cations toward the perovskite layers. This regulatory action by TPPO helps suppress the formation of low- n phases while promoting the formation of medium- or high- n phases by controlling the diffusion of spacer cations.^[94]

Fluorination of TPPO can further inhibit spacer cation diffusion (Figure 8C). Fluorinated tris(4-fluorophenyl)phosphine oxide (TFPPO) still forms hydrogen bonds between the oxygen in P=O and -NH groups but also forms hydrogen bonds between fluorine and -NH (Figure 8F).^[94] This dual hydrogen bonding strengthens the regulation of spacer cation diffusion and thereby favors the formation of high- n phases. By suppressing the formation of defective 2D phase and insulating low- n phases, Q2D perovskite LEDs with TFPPO achieve PLQY $\approx 100\%$ that arises from rapid energy transfer and high EQE_{max} of 25.6% due to increased charge mobility.

4.2.3. Growth Engineering: Additive as Inhibitor

The binding affinity of additives and spacer cations to [PbX_n]²⁻ⁿ slabs strongly affects the growth of Q2D perovskites. Additives that compete with PEA for binding to intermediates can effectively suppress the excessive growth of high- n phases. Short multi-functional additives, such as amino acids, are advantageous because they have higher binding affinity than PEA cations to [PbX_n]²⁻ⁿ slabs (Figure 8C). The effect of coordination affinity of additives toward [PbX_n]²⁻ⁿ slabs on n -phase distribution has been investigated using zwitterions: 3-aminopropylphosphonic acid (APPA), aminopropylsulfonic acid (APSA), γ -aminobutyric acid (GABA), and 4-aminobutane-1-thiol (ABT).^[97]

The binding affinity of each additive correlates with the electron-donating ability, in the order: APPA < APSA < GABA < ABT. With moderate electron-donating ability APSA and GABA, result in a concentrated phase centered around $n = 3$, without the presence of low- and high- n phases (Figure 8G). In contrast, with the weakest electron-donating ability, APPA is insufficient to effectively inhibit the growth of high- n phases resulting in broad n -distribution ranging from $n = 1$ to $n \geq 6$. On the other hand, ABT,

which has the strongest electron-donating ability, excessively inhibits growth and yields Q2D perovskite that consists predominantly of $n = 2$ phases, with a consequent significant blueshift of emission to 457 nm and a low PLQY of 26.3%. Notably, by controlling the binding affinity of additive on perovskite, concentrated medium- n phase with APSA and GABA yields high PLQYs of 47.1% and 54.4%, respectively, with a significantly faster rise time of 0.41 and 0.32 ps, compared to a rise time of 0.76 ps in the pristine sample (Figure 8G).

L-Norvaline and ethyl thiooxamate (ETO) also both possess two binding moieties that strongly coordinate to [PbX_n]²⁻ⁿ slabs: L-Norvaline has -NH³⁺ and -COO⁻, and ETO has C=O and C=S groups.^[27,110] Consequently, these compounds bind strongly to the surface, restricting the growth of Q2D perovskites, and thus prevent the formation of high- n phase formation and consequently increase EQE (L-Norvaline from 6% to 21.3%,^[27] ETO from 10.31% to 19.84%).^[110] This result demonstrates that efficient and rapid energy funneling can be achieved for Q2D PeLEDs by modulating the growth mechanism, specifically by suppression of low- n phases and narrowing of the n -distribution.

4.3. Modulation of Electrical Properties and Operational Stability

Q2D perovskite has an excess amount of insulating organic spacer cations. However, the insulating property of Q2D perovskite must be overcome for high luminance and device stability. Low charge mobility leads to low luminance and fast device degradation due to Joule heating, which accelerates ion migration. Therefore, strategies to increase the charge mobility of Q2D perovskite have been developed as follows.

4.3.1. Charge Transport Through Van Der Waals Gap

The hole and electron mobilities vary depending on the spacer cation, which affects the van der Waals gap between Q2D perovskite layers (Figure 9A). A decrease in the van der Waals gap increases carrier mobility by increasing the number of charge carriers hopping across the insulating spacer cation barrier (Figure 9B). For example, as the alkyl chain length shortens from phenylbutylammonium (PBA) to phenethylammonium (PEA) to phenylammonium (PA), the d-spacing of the $n = 1$ phase decreases from 20.1 to 16.8 to 16.7 Å (Figure 9C);^[111] this d-spacing includes both the van der Waals gap and the thickness of the inorganic perovskite layer. Benzimidazolium (BIZ) has the smallest d-spacing of 14.4 Å and therefore BIZ-based Q2D perovskite has higher electron and hole mobility than those of PBA, PEA, and PA (Figure 9C). As a result, Q2D PeLED that used the BIZ spacer had low turn-on voltage and superior I_{max} of 30 000 cd m⁻². Hence, reducing d-spacing by choosing shorter spacer cations is an effective strategy to increase charge mobility in Q2D perovskites.^[111]

Dion-Jacobson (DJ)-type bidentate spacer cations are also used to reduce the van der Waals gap (Figure 9B). These cations can bind simultaneously to two Q2D perovskite layers. Typical DJ-type spacer cations feature two binding groups para-substituted on a benzene ring. For example, 1,4-bis(aminomethyl)benzene (BAB) has two amine groups that tightly bind, resulting in a d-spacing of 11.3 Å, which is significantly shorter than

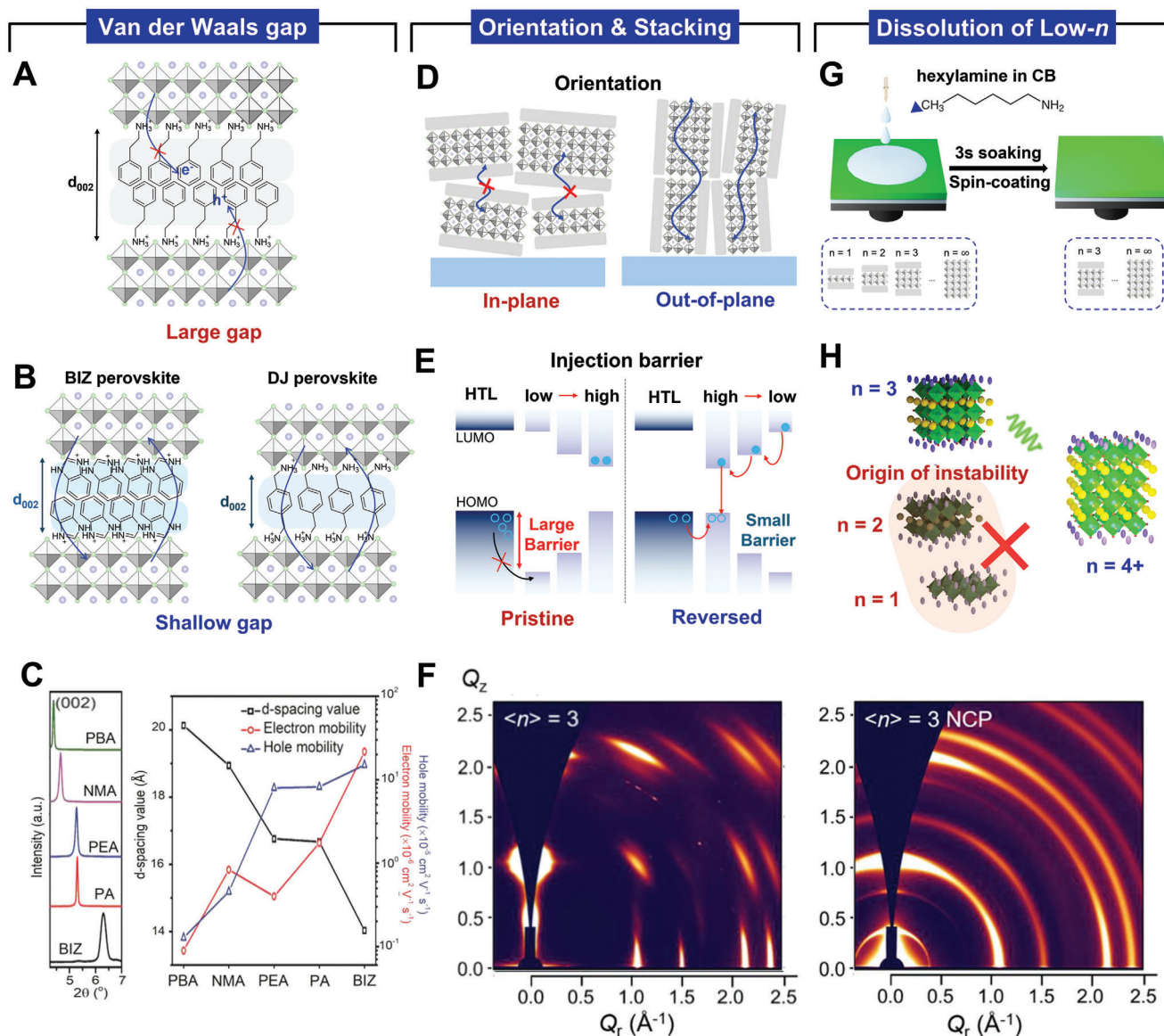


Figure 9. Schematic illustration showing A) low charge mobility with a large van der Waals gap and B) high charge mobility with shallow van der Waals gaps. C) XRD peaks of (002) plane and corresponding d-spacing, electron mobility, and hole mobility of PBA, NMA, PEA, PA, and BIZ. Reproduced with permission.^[111] Copyright 2018, WILEY-VCH. Schematic illustrations of D) charge transport depending on the orientation of quasi-2D perovskite slabs and E) of the large hole injection barrier in the $n = 1$ phase and efficient hole injection with a reduced injection barrier with a reversed energy gradient. F) Grazing-incidence wide-angle X-ray scattering results with and without the nanocrystal pinning process, showing the orientation of perovskite planes. Reproduced with permission.^[115] Copyright 2019, WILEY-VCH. Schematic illustration of G) selective dissolution of low- n phase and H) efficient radiative recombination by suppressing trap-assisted non-radiative recombination and facilitating energy funneling.

the spacing of two stacks of single-dentate spacer cations.^[112] These DJ-type cations can be partially doped into Q2D perovskites. For instance, 4-(2-aminoethyl)benzoic acid (ABA) has been introduced as a co-spacer that reduces the van der Waals gap and increases charge transfer between perovskite slabs, as a result, this approach achieved EQE_{max} of 10.11% compared to 7.07% for pristine PeLEDs.^[113] Similarly, the use of the DJ-type cation 4'-(aminomethyl)-biphenyl-3-carboxylic acid (4-ABCA) improves charge injection and transport, resulting in a high EQE of 23.15% and a high L_{max} of $133\,560\text{ cm}^{-2}$.^[114]

4.3.2. Orientations and Stacking of Quasi-2D Perovskites

Charge carrier mobility can be increased by controlling the orientation of the Q2D perovskite planes (Figure 9D). The Q2D layers with insulating spacer cations tend to stack and grow in the in-plane direction because the slow evaporation of solvents such as DMSO thermodynamically favors the growth of the (001) plane of PbBr_6 .^[115] This in-plane perovskite hinders the charge transport in the vertical direction toward electrodes.

NCP can suppress the preferential in-plane growth and accelerate perovskite crystallization, randomizing the orientation

of perovskite layers to facilitate charge transport.^[115] In grazing-incidence X-ray diffraction patterns, the samples without NCP, show a distinctive diffraction peak along the Q_z direction (out-of-plane). In contrast, with NCP, the diffraction peak appears along the Debye ring; this result indicates a random orientation of Q2D perovskite planes (Figure 9F). A random mixture of in-plane and out-of-plane Q2D perovskites effectively facilitates charge transport by creating a 3D network of charge-transport pathways. The increase of charge transport by NCP overcame the insulating nature of spacer cations and thus increased the current density at 5 V from 38.9 to 42.2 mA cm⁻².^[32] During LED operation, this increase in charge mobility by nanocrystal pinning resulted in an increase of L_{max} from 900 to 4710 cd m⁻² and a 2018-times increase in current efficiency.^[115]

Charge-transport efficiency can also be increased by increasing the out-of-plane component of Q2D perovskites. The out-of-plane Q2D perovskite facilitates better vertical charge transport between the anode and cathode through conductive inorganic perovskite slabs (Figure 9D). Amine-terminated carbon dots on the HTL promote preferential growth of out-of-plane Q2D perovskites.^[116] An increase in the proportion of out-of-plane components increased the hole mobility 3.5 times, from 1.7×10^{-6} to 5.9×10^{-6} cm² V⁻¹ s⁻¹, and increased the electron mobility by two times, from 3.2×10^{-6} to 7.8×10^{-6} cm² V⁻¹ s⁻¹. These improvements in charge transport resulted in an increase in EQE from 15.3% to 24.5%.^[116]

Reversing the stacking gradient can also improve the charge injection of Q2D PeLEDs. Typically, the film develops a vertical gradient of n -phases, with the proportion of low- n phases decreasing from the bottom to the top.^[27] The low- n phase has a deep valence band maximum (VBM) and therefore hinders hole injection at the bottom (Figure 9E). By positioning high- n phases with shallow VBM levels at the bottom of the film, charge injection efficiency can be increased.

This inversion of the gradient of n -phases can be obtained by exploiting the hydrogen bonding between 2-(methylsulfonyl)-4-(trifluoromethyl)benzoic acid (MTA) and PEA; this bonding slows the diffusion of PEA and thereby facilitates the reversal of the stacking gradient.^[117] This modification reduces the hole-injection barrier, as evidenced by a shift of the VBM level from -5.69 to -5.62 eV and a decrease in turn-on voltage from 3.1 to 2.9 V. The efficient charge injection obtained using MTA increased the L_{max} from 110 000 to 290 000 cd m⁻², and the EQE from 16.8% to 25.9%.^[117]

4.3.3. Selective Dissolution of Defective and Insulating Low- n Phases

Low- n phases, particularly 2D monolayer $n = 1$ phases are highly insulating and promote non-radiative recombination, and this problem is a major cause of degradation of Q2D perovskites during LED operation. In certain cases, small amounts of low- n phases located at grain boundaries surrounding 3D phases can enhance the stability of perovskite light-emitting diodes and solar cells by passivating dangling bonds and mitigating incomplete coordination.^[79,118] Additionally, small n -phases ($n = 2, 3$) are crucial for achieving deep-blue emission in Q2D-PeLEDs with high EQE.^[86] Those are because low- n phases thermodynamically exhibit a lower defect density compared to their 3D counterparts

due to their inherently higher defect formation energy from lattice distortion that releases lattice strain.^[119,120]

Despite this advantage, some defects in low- n phases act as deep traps that significantly increase non-radiative recombination, unlike the shallow traps typically found in 3D phases.^[120] Consequently, a large proportion of low- n or 2D phases can hinder efficient radiative recombination in green-emitting Q2D-PeLEDs that utilize medium- n or high- n phases. Furthermore, the presence of a substantial amount of insulating spacer cations in low- n phases leads to Joule heating during LED operation, which promotes ion migration and ultimately results in the decomposition of the perovskite.^[55,121] Therefore, the low- n phases must be removed to improve the stability of Q2D-PeLEDs.

One promising strategy to overcome the insulating properties of Q2D perovskites is the selective removal of low- n phases (Figure 9G). This goal has been achieved by applying a carefully-controlled mixture of polar and non-polar solvents to Q2D perovskite films after spin-coating.^[21] The key to this process lies in the precise control of the polarity of the polar solvent, to achieve selective dissolution of targeted low- n phases. In this case, a small amount of hexylamine, a polar solvent, was used to selectively dissolve the defective $n = 1$ and $n = 2$ phases, and chlorobenzene, a non-polar solvent, which barely interacted with the perovskite structure (Figure 9H). This selective removal of defective low- n phases serves two critical functions: it suppresses trap-assisted non-radiative recombination and promotes efficient energy funneling from medium- n to high- n phases. Effective elimination of low- n phases increased conductivity and achieved a high L_{max} of 147 832 cd m⁻². The prevention of Joule heating also increased operational stability and achieved a state-of-the-art T_{50} of ≈ 50 000 h. These advancements, coupled with an EQE of 29.5%, underscore the importance of removing low- n phase to optimize Q2D-PeLEDs.^[21]

5. Perovskite Nanocrystals

Perovskite nanocrystals (PNCs) are synthesized as colloidal particles in a non-polar solvent and then deposited onto a substrate, whereas nanoscale PC perovskites and Q2D perovskites are typically deposited and crystallized directly on the substrate.^[2,122] PNCs offer the advantage of easy tunability of particle size, enabling highly efficient excitonic recombination properties, even in the early stages of development. Additionally, because material properties are adjusted prior to deposition, PNCs are more suitable for large-area applications or mass production.

5.1. Fundamental Approaches for Efficient PNCs

An important feature of PNC is that their crystal growth is terminated in solution while using organic ligands.^[2,123,124] These ligands are multifunctional, which 1) control PNC size, 2) bind to the surface to passivate defects, and 3) prevent PNC aggregation; all of these functions significantly affect the luminescent properties of PNCs. However, high ligand density or long alkyl chains can hinder charge transport increase the charge-injection barrier, and thereby reduce the efficiency of PeLEDs. Therefore, the management of PNC properties requires ligand engineering.

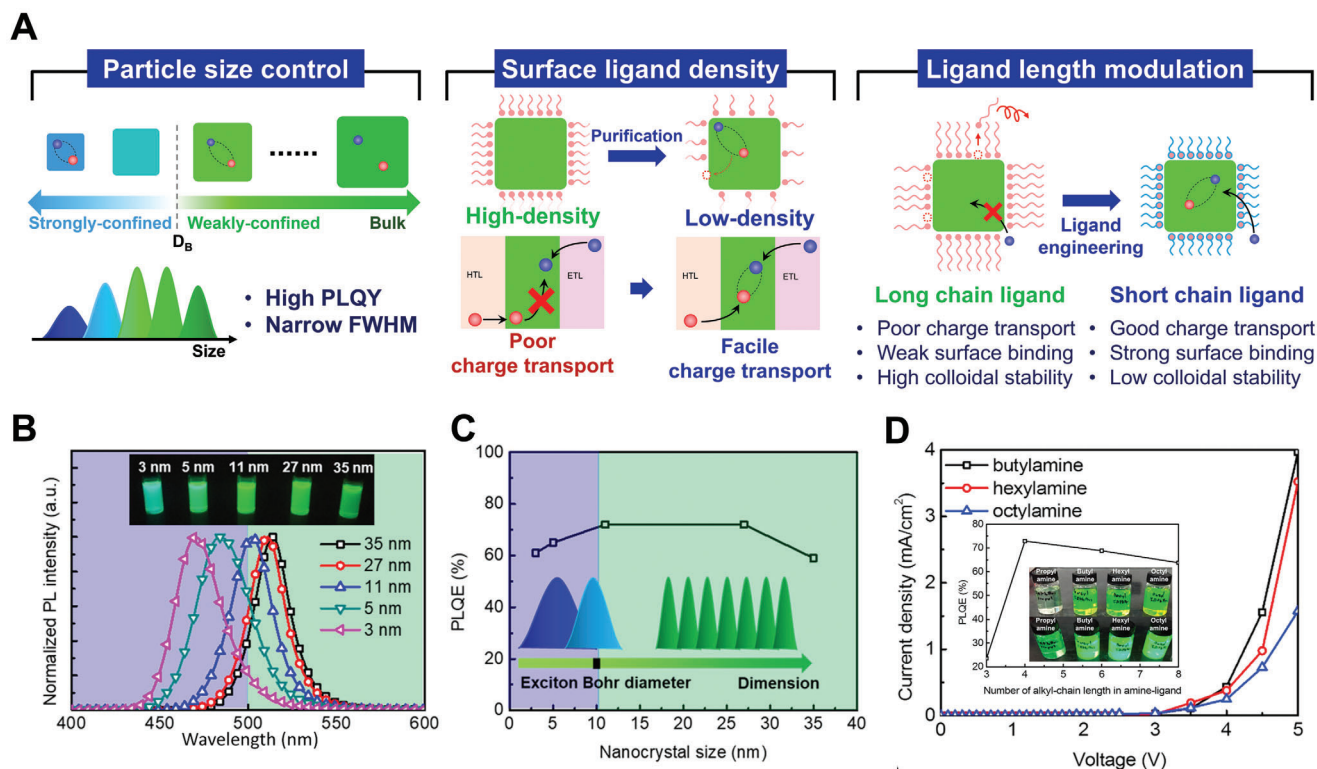


Figure 10. A) Schematic illustration of fundamental approaches to synthesizing efficient PNCs. Size control of PNCs (Left). Reduction of PNC size below D_B induces strong quantum confinement, leading to a blue shift in the PL spectrum. Surface ligand density (Middle). Decreasing the density of ligands can improve charge transport, but it can generate surface defects, inducing exciton quenching. Ligand length modulation (Right). Short chain ligands generally exhibit good charge transport properties and strong surface binding characteristics but compromise colloidal stability. B, C) PL spectrum, photographs under UV light (B), and PLQY (C) of MAPbBr₃ PNC solutions with varying sizes from 3 to 35 nm. D_B is ≈ 10 nm. PNCs with the size over D_B show size-independent PL spectra. Reproduced with permission.^[124] Copyright 2017, American Chemical Society. D) Electron current density of electron-only devices based on FAPbBr₃ PNCs that had various lengths of the alkyl chain.^[34] Inset: PLQY of FAPbBr₃ PNC solutions with amine ligands of various alkyl chain lengths. Photographs: FAPbBr₃ PNC solutions with (bottom row) and without (top row) UV light exposure. Reproduced with permission.^[34] Copyright 2017, Elsevier.

The basic approaches include 1) controlling PNC size, 2) adjusting the density of ligands at the crystal surface, and 3) modifying the length of alkyl chains in the ligands (Figure 10A). In the following section, we will explain these factors based on pioneering studies that have established the key guidelines for designing efficient PNCs.

5.1.1. Size of PNCs

According to initial foundational PNC patents proposed in 2014, highly efficient emitters require PNCs of optimal size, typically slightly larger than the exciton Bohr diameter (D_B).^[125–127] If PNCs are too large (> 30 nm), exciton confinement is inefficient, leading to low PLQY due to the thermal dissociation of excitons.^[124] On the contrary, reducing PNC size below D_B induces quantum-confinement effects, causing a blueshift in emission wavelength. This effect can be exploited to synthesize blue-emitting PNCs from single-bromide perovskites that typically emit green-light (Figure 10B).^[128–130] However, a reduction in PNC size increases the surface-to-volume ratio, thereby increasing the density of surface defects and decreasing the PLQY.^[131]

Therefore, when small, highly confined PNCs are used, management of surface defects becomes critical.

The size of PNCs can be controlled by adjusting synthesis conditions, such as ligand concentration or synthesis temperature. Adjusting ligand concentration affects crystal growth by interfering with the diffusion of perovskite precursors.^[132] Low ligand concentrations can allow crystal sizes to exceed D_B , and this effect yields size-independent emission spectra with narrow linewidth. Increasing the concentration of a carboxylic acid (e.g., oleic acid) reduces crystal size below D_B , and thereby induces quantum-confinement effects and blueshifted PL emission with broadened linewidth. Fine adjustment of the concentration of oleic acid enabled precise control of the size of MAPbBr₃ PNCs to around D_B (Figure 10C). Among MAPbBr₃ PNCs with sizes ranging from 3 to 35 nm, the PNCs with the size of 11 nm, which is slightly larger than D_B , exhibited the highest PLQY. Due to the optimal emission efficiency, PNC-LEDs based on the 11 nm MAPbBr₃ achieved the highest EQE of 5.09% among the MAPbBr₃ PNCs with various sizes.

Synthesis temperature also affects PNC size. Using the hot-injection method, CsPbX₃ PNCs (X = Cl⁻, Br⁻, I⁻) were synthesized by reacting Cs-oleate with lead halide, and sizes could

be controlled by adjusting the reaction temperature.^[2] As this temperature decreased from 200 to 140 °C, the CsPbBr₃ PNC sizes decreased from 11.8 to 3.8 nm. As PNC size decreased, the bandgap increased due to quantum confinement, and the PL emission wavelength was blueshifted. Similarly, decreasing synthesis temperature in the ligand-assisted reprecipitation (LARP) method reduces PNC size and blueshifts their PL emission.^[133]

Through various studies on the size control of PNCs, it has been clearly demonstrated that PNC growth is influenced by thermodynamic and kinetic control such as temperature, ligand concentration, precursor conditions (e.g., halide compositions, concentration, reactivity).^[132,134] However, the complex ionic nature and low lattice formation energy of perovskites, the dynamic nature of ligands, and the extremely fast growth of PNCs occurring in seconds make it difficult to separate nucleation and growth processes, thereby complicating the understanding of the PNC growth mechanism.^[135] Despite these difficulties, a recent study utilized TOPO as a sole ligand, rather than the traditional acid-base pair, to investigate the nucleation and growth mechanisms in PNCs.^[136] This study revealed that the complex equilibrium between PbBr₂ precursors and A[PbBr₃] solute affects the conversion path of precursor-monomer-nuclei, enabling to precise control size of PNCs with uniform distribution. Nonetheless, an accurate theoretical model for PNC growth mechanisms using the commonly employed acid-base pair is still lacking.

5.1.2. Surface Ligand Density of PNCs

Controlling ligand density is crucial because the insulating ligands hinder charge transport, and thereby degrade the efficiency of PeLEDs (Figure 10A). To effectively utilize PNCs for the emissive layer in PeLEDs, purification to partially remove these insulating ligands is essential. Purification is typically performed using flocculation solvents such as methyl acetate, ethyl acetate, or acetone, then using centrifugation to precipitate PNCs that have reduced ligand density. However, excessive ligand detachment can generate surface defects. Therefore, ligand removal must be carefully controlled to facilitate charge transport while minimizing defect formation.

For example, performing two washing cycles using a hexane/ethyl acetate mixture moderately reduced the surface ligand density, and yielded CsPbBr₃ PNCs that have balanced PLQY and EQE. This approach achieved PLQY > 90% and 50 times enhancement in EQE, reaching up to 6.27%.^[137] Ionic perovskites are susceptible to solvents that have high dielectric constants, so using low-dielectric solvents in the purification process helps maintain high PLQY. By employing diethylene glycol dimethyl ether (diglyme), which has a low dielectric constant ($\epsilon = 7.23$), as a washing solvent, PNC-LEDs that had low turn-on voltage (2.7 V) and high EQE_{max} (8.08%) were demonstrated.^[138] Additionally, simply storing the PNC solution in a refrigerator enables precipitation of excess ligands and impurities without using flocculation solvents, and thereby improves PNC purity.^[139]

However, excessive removal of ligands can generate surface defects due to insufficient passivation, and thus reduce the PLQY of the PNC solution. Furthermore, significant ligand loss can break down the colloidal stability of PNCs, leading to aggregation, which is detrimental to film fabrication. Therefore, to bal-

ance PLQY, colloidal stability, and electrical properties, the ligand density must be delicately controlled.

5.1.3. Ligand Length Modulation in PNCs

The chain length of ligands has a strong effect on the optical and electrical properties of PNCs. While longer alkyl chains enhance colloidal dispersion, they restrict charge carrier transport and thereby reduce EQE (Figure 10A).^[140] Longer alkyl chains also reduce ligand polarity, thereby decreasing adsorption energy on the PNC surface,^[141] and can cause steric hindrance between ligands.

Adjusting the chain length of primary alkylamines during PNC synthesis predominantly influences photophysical and electrical properties. For example, FAPbBr₃ PNCs synthesized with n-hexylamine and n-octylamine exhibited particle sizes smaller than 10 nm, whereas those synthesized with n-butylamine had sizes of ≈ 10 nm.^[34] This indicates that long organic alkyl chains can suppress crystal growth, leading to smaller particle sizes. However, PLQY decreased from 69% with n-hexylamine to 64% with n-octylamine, due to inferior surface passivation caused by steric hindrance between ligands (Figure 10D). Conversely, very short ligands like n-propylamine led to a loss of colloidal stability, so the PNCs aggregated and the PLQY decreased to 25%. FAPbBr₃ PNCs with n-butylamine achieved optimal PLQY by balancing colloidal stability and surface passivation. Moreover, as chain length increases, insulating properties become more pronounced; this impedes charge transport and reduces carrier confinement within PNCs, and therefore degrades EQE and luminance (Figure 10D). Among the various ligands, FAPbBr₃ PNC with n-butylamine exhibited the highest PLQY and the most efficient charge transport. This enabled the corresponding PNC-LEDs to achieve a current efficiency of 9.16 cd A⁻¹ and EQE of 2.05%.^[34] Although the fundamental approaches for achieving efficient PNCs have been discussed above, the optimal ligand length and density should be tailored based on the composition of perovskite crystals and the appropriate PNC size employed in PNC-LEDs.

5.2. Core-Crystal Engineering for Stabilized PNCs

Defects can be formed within PNCs after synthesis due to the ionic nature of perovskites. These defects cause exciton quenching and lead to accelerated degradation. To mitigate these defects and stabilize PNCs, core-crystal engineering is employed by adding A-site cation dopants (e.g., Cs⁺, MA⁺, FA⁺, and GA⁺) and B-site cation dopants (e.g., Co²⁺, Sn²⁺, Cd²⁺, Zn²⁺, Ni²⁺, Mn²⁺, Sr²⁺, Ce³⁺) (Figure 11A and Table 4). These ionic dopants influence the formation and optical/electrical properties of PNCs.

5.2.1. A-Site Cation Doping

A-site cation doping can primarily impact lattice stabilization. A-site cations with ammonium moieties (e.g., MA, FA, and GA) promote lattice stabilization by forming hydrogen bonds with

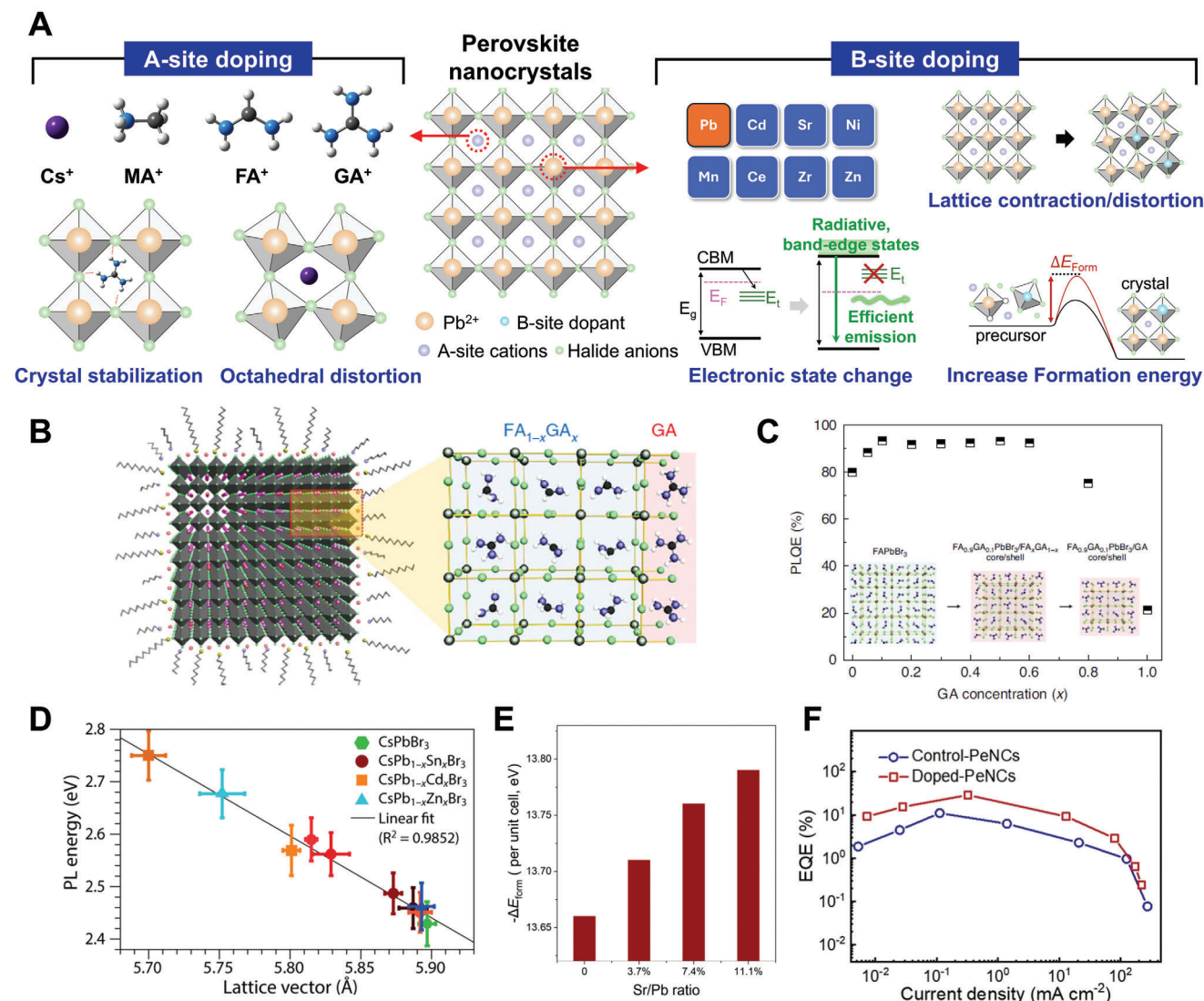


Figure 11. A) Schematic illustration of core-crystal engineering in PNCs. A-site cations with ammonium moiety form hydrogen bonds with halide anions, stabilizing perovskite crystal. B-site cations have various effects on the optical properties of PNCs. B) Schematic illustration of core-crystal engineered FAPbBr₃ PNCs by doping GA cations. Reproduced with permission.^[26] Copyright 2021, Springer Nature. C) PLQY of FA_xGA_{1-x}PbBr₃ PNCs. Reproduced with permission.^[26] Copyright 2021, Springer Nature. D) PL energies versus lattice vectors in Sn, Cd, Zn-doped CsPbBr₃ PNCs. Reproduced with permission.^[148] Copyright 2017, American Chemical Society. E) Calculated formation energies of α -CsPbI₃ PNCs with increasing the ratio of Sr/Pb. Reproduced with permission.^[154] Copyright 2019, American Chemical Society. F) EQE of FAPbBr₃ PNC-LEDs without and with core-crystal engineering by Cd²⁺ doping. Exciton binding energy was higher in Cd²⁺-doped FAPbBr₃ PNCs than in the control sample. Reproduced with permission.^[150] Copyright 2024, WILEY-VCH.

halide ions.^[142,143] On the other hand, inorganic cations like Cs⁺ and Rb⁺, although lacking the ammonium moiety, offer the advantage of superior chemical stability.^[144] Additionally, these inorganic cations induce lattice contraction due to their smaller size than MA, FA, and GA cations, leading to an increase in the bandgap.^[143] By effectively utilizing these effects of A-site doping, the lattice of PNCs can be further stabilized, which significantly enhances luminescent properties.

GA⁺ cation dopants that contain three ammonium moieties can stabilize FAPbBr₃ PNCs (Figure 11B).^[26] Compared to FA⁺, GA⁺ has a larger ionic radius that is beyond the tolerance of cubic-phase perovskite. This lattice mismatch led to a contin-

uous increase in internal energy (enthalpy), but up to 12.5% GA⁺ can be incorporated into the FAPbBr₃ due to the effect of entropy stabilization. The extra amino group of GA⁺ compared to FA⁺ forms hydrogen bonds with bromide anions, and this effect increases internal stabilization. This core-crystal engineering approach increased the PLQY from 79.9% for FAPbBr₃ PNCs to 93.3% for FA_{0.9}GA_{0.1}PbBr₃ PNCs (Figure 11C). Using this strategy, PNC-LEDs achieved a record EQE of 23.4% with EL emission at 531 nm which satisfies the Rec. 2020 color standard.^[26]

Inorganic cations can also enhance the luminescence efficiency of PNCs. Increasing the ratio of Cs⁺ in FA_xCs_{1-x}PbBr₃

Table 4. Performance of PNC-LEDs based on core-crystal engineering techniques.

Cation type	Cation	Perovskite Composition	Working mechanism	PLQY	EL peak (FWHM)	EQE	Operational lifetime	Refs.
A-site	Ag ⁺	CsPbI ₃	Defect passivation	> 60%	690 nm (36 nm)	11.2%	–	[146]
A-site	FA ⁺ , GA ⁺	CsPb(Br/Cl) ₃	Internal crystal stabilization	32% (GA), 39% (FA)	490.5 nm (GA), 492.5 nm (FA)	3.02% (GA), 4.14% (FA)	1.55 min @ 74 cd m ⁻² 1.82 min @ 98 cd m ⁻²	[190]
A-site	GA ⁺	FAPbBr ₃	Internal crystal stabilization	93.3%	531 nm	23.4%	132 min @ 100 cd m ⁻²	[26]
A-site	Rb ⁺	CsPb(Br/Cl) ₃	Reduce trap state	30% (460 nm) 45% (465 nm) 62% (470 nm) 71% (475 nm) 80% (480 nm)	460 nm 465 nm 470 nm 475 nm 480 nm	12.0% (460 nm) 16.7% (465 nm) 21.3% (470 nm) 24.3% (475 nm) 26.4% (480 nm)	–	[147]
B-site	Co ²⁺	CsPbBr ₃	Reduce structural defect Change Fermi level	96%	516 nm (16.7 nm)	21.8%	~300 s @ 40 mA cm ⁻²	[256]
B-site	Cd ²⁺	CsPb(Br/Cl) ₃	Defect passivation Increase E _b	95%	490 nm (19 nm)	14.6%	12 min @ 134 cd m ⁻²	[257]
B-site	Cd ²⁺	FAPbBr ₃	Increase E _b Change Fermi level	>90%	534 nm (22 nm)	29.4%	111.8 min @ 100 cd m ⁻²	[150]
B-site	Zn ²⁺	CsPbI ₃	Suppress defect formation Increase E _b Change Fermi level	98.5%	682 nm	15.1%	–	[152]
B-site	Mn ²⁺ , Ni ²⁺	CsPb(Br/Cl) ₃	Defect passivation	70.2%	469 nm (21 nm)	3.31%	8 min @ 7.3 mA cm ⁻²	[258]
B-site	Mn ²⁺	CsPb(Br/Cl) ₃	Reduce trap state	28%	466 nm (17.9 nm)	2.12%	–	[259]
B-site	Sr ²⁺	CsPbI ₃	Suppress defect formation Increase formation energy	99.8%	687 nm	17.1%	40 min @ 100 cd m ⁻²	[155]
B-site	Sr ²⁺	CsPbI ₃	Increase formation energy Change Fermi level	84%	691 nm	13.5%	–	[151]
B-site	Sr ²⁺	CsPbI ₃	Increase formation energy	>90%	678 nm (32 nm)	5.92%	120 min @ 6V	[154]
B-site	Ce ³⁺	CsPbBr ₃	Generation of radiative near-band-edge states	89%	~515 nm (19 nm)	4.4%	–	[158]
B-site	Zr ²⁺	CsPbI ₃	Defect passivation Change Fermi level	91%	686 nm	13.7%	–	[260]

PNCs gradually induces lattice contraction, and this increases crystallinity and chemical stability.^[145] Ag⁺ cations, diffused from the Ag electrode into the PNC active layer, where they reacted with I⁻ on the PNC surface to form AgI, passivated defects. This method yielded a red PNC-LED that had an EQE of 11.2%.^[146] Incorporating Rb⁺ into CsPb(Br_x/Cl_{1-x})₃ PNCs induces lattice contraction due to the smaller size of Rb⁺ compared to Cs⁺, which increases the bandgap of PNCs. Rb⁺ doping allowed for reducing Cl⁻ content, which typically forms deep traps, while still maintaining the bandgap for blue-emission.^[147] This compensation approach enabled to minimization of the use of Cl⁻ ions for blue emission, resulting in improved PLQY. This strategy enables the realization of highly efficient blue PNC-LEDs that had an EQE of 26.4% at a peak wavelength of 480 nm.^[147]

5.2.2. B-Site Cation Doping

Replacing B-site Pb²⁺ ions (1.19 Å) with divalent or trivalent B-site metal cations like Sr²⁺ (1.18 Å), Cd²⁺ (0.95 Å), Mn²⁺ (0.83 Å), Zn²⁺ (0.74 Å), and Ce³⁺ (1.01 Å), regulates PNC optical properties (Figure 11A). Core-crystal engineering through B-site cation doping can influence several critical factors, including 1) optical

bandgap shift by lattice contraction, 2) formation energy of perovskite, 3) structural defects, 4) exciton binding energy, 5) generation of emissive energetic states, and 6) electrical properties of PNCs by shifting energy level (e.g., CBM, VBM, and Fermi level).

Optical bandgap energies exhibit a linear correlation with the lattice vector in metal cation-doped CsPbBr₃ PNCs. This relationship arises because B-site metal cations with smaller ionic radius than that of Pb²⁺ contract the perovskite lattice, and thus shorten the Pb–Br bond lengths in PbBr₆ octahedra. The lattice contraction increases the overlap between Pb and Br orbitals and thereby raises the energy level of the conduction band minimum (CBM). Consequently, the absorption and emission spectra are slightly blueshifted (Figure 11D).^[148]

Doping with different elements enables tuning of the electrical properties of PNCs by shifting electronic levels such as CBM, VBM, and Fermi energy levels.^[1] The modification of CBM and VBM directly influences the injection barrier at the interface between PNC and HTL (or ETL) layers. If the injection barrier is too high, charge carrier accumulation can occur at the interface, leading to reduced charge balance and ultimately resulting in inefficient EL emission. Moreover, PNCs typically have n-type characteristics, meaning that the Fermi level is located close to the CBM of PNCs.^[1] This n-type characteristics can also impede efficient

hole injection and reduce charge balance, thereby making PNCs with ambipolar properties is also an important requisite for efficient EL in PNCs.^[149] Actually, by doping B-site cations such as Zn²⁺, Cd²⁺, and Sr²⁺, efficient carrier injection and charge balance were simultaneously achieved, resulting in a significant improvement in EQE.^[150–152]

B-site cation doping increases the formation energy of perovskite crystals and thereby stabilizes their structure. Formation energy decreases as crystal size decreases, so this effect is particularly effective in small PNCs, which may be significantly stabilized by doping. The elevated formation energy also greatly improves the phase stability of PNCs.^[153] For instance, iodine-based perovskites such as CsPbI₃ tend to transform to a non-perovskite δ -phase due to their low formation energy. Doping with Sr²⁺ ions increases the formation energy of α -CsPbI₃ PNCs (Figure 11E), and yields significantly enhanced phase stability, as well as improved efficiency, thermal stability, and EL stability.^[151,154,155] Core-crystal engineering with Sr²⁺ doping yielded PNC-LEDs that had an EQE_{max} of 17.1%.^[155]

Core-crystal engineering by incorporating B-site dopants effectively suppresses internal defects; i.e., short-range disorder, in PNCs. Incorporating Ni²⁺ ions into CsPbCl₃ PNCs increased defect formation energy and filled halide vacancies. The improved short-range order of the perovskite lattice boosted PLQY to 93.1%.^[156] Additionally, doping B-site cations of smaller sizes than Pb²⁺ induces beneficial lattice distortions that increase the exciton effective mass and raise the exciton binding energy.^[157] In a recent study, Cd²⁺ doping increased the exciton binding energy from 94 meV for control PNCs to 252 meV for Cd²⁺-doped PNCs, while maintaining nearly steady Auger recombination rates; PNC-LEDs that used these doped PNCs had an EQE_{max} of 29.4% (Figure 11F).^[150]

Dopants can also modify the electron density at the band edge, and thereby affect the efficiency of band-edge emission. Ce³⁺ doping, for example, increased the density of near band-edge radiative states;^[158] This change widened the radiative exciton relaxation channels and increased the EQE of PNC-LEDs from 1.6% to 4.4%.^[158]

5.3. Surface Reconstruction for Efficient and Stable PNC-LEDs

Low vacancy-formation energies of A-site cations and halide anions, along with low activation energy for halide migration, lead to defects such as ionic vacancies, undercoordinated Pb²⁺ ions, and interstitial defects. Ligands strongly bound to the surface of PNCs contribute to passivating these surface defects and improving the stability of the PNCs. However, labile ligands like oleylamine (OAm) and oleic acid (OA) induce defect formation during film deposition, by detaching from the PNC surface due to their dynamic binding. Therefore, achieving high-efficiency PNC-LEDs requires highly defect-tolerant surface reconstruction, which alleviates exciton quenching by either eliminating halide vacancies or neutralizing undercoordinated Pb atoms on the surface.

Maximizing the effect of surface reconstruction requires elaborate ligand design, considering both the head group and the tail group (Figure 12A). The head group is typically a functional moiety such as phosphine oxide, phosphonic acid, or ammonium

bromide, and has an important function in passivating halide vacancies or uncoordinated Pb²⁺ ions, which act as non-radiative recombination centers. Equally important is the design of the tail group, which significantly influences charge-transport properties, inter-particle coupling, and steric hindrance.

Surface reconstruction of PNCs to increase their luminescence efficiency and stability can be achieved using several experimental methods (Figure 12A): 1) In situ modification, which involves adding ligands directly to the synthesis precursor, thereby enabling simultaneous crystallization control and surface passivation during PNC formation. 2) Ligand exchange, by which the initial ligands can be replaced with alternatives that offer superior passivation and improved electrical properties. 3) Layer-type surface modification, which represents depositing an interlayer, either on the top or bottom, to influence PNC film growth and provide additional passivation. Surface reconstruction combined with ligand design can provide beneficial effects such as 1) Surface halide enrichment, 2) Strong coordination to lead ions, and 3) Hetero-interface passivation (Table 5).

5.3.1. Surface-Halide Enrichment

Alkyl ammonium salts are commonly used for surface-halide enrichment and are often applied using post-treatment methods. Halide anions (Cl⁻, Br⁻, I⁻) in alkyl ammonium salts passivate the PNC surface by filling halide vacancies; electrostatic interactions between alkylammonium cations and halide anions provide further stabilization. Additionally, the hydrocarbon moieties of these salts help maintain colloidal stability.

Employing the alkylammonium salts with relatively shorter hydrocarbon chain than weakly-binding oleylamine and oleic acid has shown superior passivation ability and improved charge transport properties, with di-dodecyl dimethyl ammonium bromide (DDAB) being one of the most representative materials, which significantly increased EQE.^[159–163] Moreover, post-treatment using alkylammonium salts with different halide ions enables halide-exchange, which can adjust the bandgap of PNCs. Treatment of oleylammonium iodide salts replaced original bromide ions in CsPbBr₃ PNCs as well as reduced halide defects, yielding red PNC-LEDs with an EQE of 21.3%.^[164]

Post-synthesis treatment with a ligand containing an aromatic ring moiety in the tail can significantly affect electrical properties and charge carrier dynamics in PNCs. Phenethylammonium halide (PEA-X) is the representative aromatic ammonium halide ligand;^[165] aniline hydroiodide, which is shorter than PEA-X, has also been used to produce highly conductive PNCs.^[22,166] Replacing the phenyl moiety with a thiophene group led to the multifunctional ligand 2-thiophen propylamine bromide (ThPABr), which not only replaced OAm⁺ and passivated halide vacancies, but its thiophene group coordinated with Pb²⁺ ions.^[167] Furthermore, triplet energy level (T₁) from π -electrons in polyaromatic moieties also contribute to luminescence quenching in PNCs. Smaller PNCs are particularly prone to severe quenching due to the triplet energy levels of aromatic molecules such as tetracene.^[168,169] A previous study on aromatic ligands revealed that NMA, with a low triplet energy level (T₁ = 2.6 eV), caused efficiency losses in monolayer and low-n phases of Q2D PeLEDs. In contrast, PEA, with a higher triplet energy level

Table 5. Performance of state-of-the-art LEDs that exploit surface-reconstructed-PNCs.

Surface Management Type	Ligand Type	Passivating molecule	Perovskite composition	Color	PLQY	EL Peak (FWHM)	Luminance	EQE	Operational lifetime	Refs.
Post-treatment	Alkyl ammonium salts Alkyl ammonium salts	OAMI AnI	CsPb(Br/I) ₃	Red	80%	649 nm (33 nm)	500 cd m ⁻²	21.3%	180 min @ 100 cd m ⁻²	[164]
Post-treatment	Alkyl ammonium salts	DDAB	CsPbBr ₃	Green		518 nm	45 012 cd m ⁻²	18.6%	60 min @ 2000 cd m ⁻²	[163]
Post-treatment	Alkyl ammonium salts	DDAF	CsPbBr ₃	Green	90±7%	511 nm	2030 cd m ⁻²	19.3%	50 s @ 1000 cd m ⁻²	[173]
Post-treatment	Alkyl ammonium salts	DDeAB DLIPS	CsPbBr ₃	Green	98%	513 nm	9464 cd m ⁻²	12.17%	–	[161]
Post-treatment	Alkyl ammonium salts	ThPABr	CsPbBr ₃	Green	83%	519 nm (18 nm)	13 649 cd m ⁻²	10.5%	621 s @ 100 cd m ⁻²	[167]
Post-treatment	Inorganic halide Alkyl ammonium salts	NaBr-IPABr	CsPbBr ₃	Blue	100%	479 nm 505 nm		12.3% 22%	20 min (L ₀ = 90 cd m ⁻²) 60 min (L ₀ = 1200 cd m ⁻²)	[188]
Post-treatment	Alkyl ammonium salts	PEABr	CsPbBr ₃	Blue	81.6%	463 nm (17 nm)	141 cd m ⁻²	2%	–	[165]
Post-treatment	Alkyl ammonium salts	OctBr	CsPbClBr ₂	Blue	95%	480 nm	1820 cd m ⁻²	3.05%	–	[162]
Post-treatment	Alkyl ammonium salts	DAT	CsPb(Br/Cl) ₃	Blue	100%	471 nm (17 nm)	465 cd m ⁻²	6.3%	99 s @ 4.5V	[174]
Post-treatment	Alkyl ammonium salts	TBABF ₄	CsPb(Br/Cl) ₃ CsPbBr ₃ CsPb(Br/I) ₃	Blue Green Red	80% (Green)	475 nm (19 nm) 520 nm (19 nm) 635 nm (36 nm)	700 cd m ⁻² 5000 cd m ⁻² 900 cd m ⁻²	18.2% 26.2% 22.7%	10 h @ 100 cd m ⁻²	[261]
In-situ modification	Alkyl ammonium salts	HzAc	CsPb(Br/Cl) ₃	Blue	94%	475 nm (14.67 nm)	659 cd m ⁻²	7.82%	49 s @ 100 cd m ⁻²	[262]
Layer	Halogenated organic molecule	TBTB	(FA/GA)PbBr ₃	Green	93.3%	531 nm	–	23.4%	132 min @ 100 cd m ⁻²	[26]
Layer	Halogenated organic molecule	TBB	FAPbBr ₃	Green	>95%	~531 nm (20 nm)	5980 cd m ⁻²	20.1%	T80 ~ 2.9 h @ 100 cd m ⁻²	[263]
Post-treatment	Halogenated organic molecule	TMSBr	CsPbBr ₃	Blue	81%	463 nm	300 cd m ⁻²	11.9%	17 min @ 100 cd m ⁻²	[187]
Post-treatment	Halogenated organic molecule	TMSI	CsPbI ₃	Red	99%	656 nm (33 nm)	1308 cd m ⁻²	22.62%	311 min @ 100 cd m ⁻²	[186]
Post-treatment	Halogenated organic molecule Alkyl ammonium salts	TMSBr AnHI	CsPb(Br/I) ₃	Red	86%	636 nm (28 nm)	7000 cd m ⁻²	22%	T ₉₀ ~ 780 h (L ₀ = 100 cd m ⁻² , r = 1.95)	[22]
Post-treatment	Halogenated organic molecule	Acyl chloride	CsPbI ₃	Red	90%	638 nm	2511 cd m ⁻²	26.1%	7.5 h @ 100 cd m ⁻²	[264]
In-situ modification	Coordinating ligands Alkyl ammonium salts	DSPA TMPI	CsPbI ₃	Red	100%	644 nm	4140 cd m ⁻²	28.5%	30.4 h @ 100 cd m ⁻²	[176]
Post-treatment	Coordinating ligands	NSA	FAPbBr ₃	Green	81%	532 nm (21 nm)	67 115 cd m ⁻²	19.2%	20 min @ 100 cd m ⁻²	[172]

(Continued)

Table 5. (Continued)

Surface Management Type	Ligand Type	Passivating molecule	Perovskite composition	Color	PLQY	EL Peak (FWHM)	Luminance	EQE	Operational lifetime	Refs.
Post-treatment	Coordinating ligands	CsTFA	CsPb(Br/Cl) ₃	Blue	84%	490 nm (16 nm)	2843 cd m ⁻²	23.5%	43.41 min @ 100 cd m ⁻²	[265]
Post-treatment	Coordinating ligands	Lecithin	CsPbI ₃	Red	100%	634 nm (39 nm)	1391 cd m ⁻²	7.1%	33 min @ 200 cd m ⁻²	[266]
Post-treatment	Coordinating ligands	Cysteine	Cs(Mn/Pb)I ₃	Red	99%	653 nm	250 cd m ⁻²	18%	87 min @ 100 cd m ⁻²	[267]
Post-treatment	Coordinating ligands	Tryptophan	CsPb(Br/I) ₃	Red	98%	635 nm (33 nm)	12 910 cd m ⁻²	22.8%	63 min @ 100 cd m ⁻²	[175]
In-situ modification	Coordinating ligands	PMA	CsPbI ₃	Red	89%	689 nm (38.2 nm)	618 cd m ⁻²	17.8%	317 h @ 30 mA cm ⁻²	[177]
In-situ modification	Coordinating ligands	DPA-PMAO	CsPb(Br/I) ₃	Red	80%	647 nm	1000 cd m ⁻²	23.6%	2500 min @ 150 cd m ⁻²	[178]
Post-treatment	Coordinating ligands	EC	CsPbI ₃	Red	87%	686 nm (32 nm)	1674 cd m ⁻²	12.1%	80 min @ 3V	[268]
Post-treatment	Coordinating ligands	S-TBP	Cs(Co/Pb)Br ₃	Green	96%	516 nm (16.7 nm)	60 000 cd m ⁻²	21.8%	~300 s @ 40 mA cm ⁻²	[256]
In-situ modification	Coordinating ligands	4-FBSA	CsPbI ₃	Red	93%	630 nm (35 nm)	21 590 cd m ⁻²	21.8%	11.7 h @ 100 cd m ⁻²	[269]
Post-treatment	Coordinating ligands	EDTA l-glutathione	MAPb(Br/I) ₃	Red	70%	620 nm	627 cd m ⁻²	20.3%	130 min @ 141 cd m ⁻²	[270]
Layer	Coordinating ligands	TSPO1	CsPbBr ₃	Green	85±3%	516 nm (20 nm)	21 000 cd m ⁻²	18.7%	30 min @ 1000 cd m ⁻²	[179]
Layer	Inorganic Halide	LiBr	(FACs)PbBr ₃	Green	70%	518 nm (18 nm)	38 582 cd m ⁻²	16.45	0.462 h @ 300 cd m ⁻²	[181]
Layer	Inorganic Halide	KI	CsPbI ₃ :Sr	Red	79.2%	687 nm (37 nm)	576 cd m ⁻²	21.8%	69 min @ 100 cd m ⁻²	[180]
In-situ modification	Inorganic Halide	CaBr ₂	CsPb(Br/I) ₃	Red	92%	648 nm	11 233 cd m ⁻²	13.2%	–	[271]
Post-treatment	Inorganic Halide	ZnBr ₂	CsPbBr ₃	Blue	99%	469 nm (21 nm)	12 060 cd m ⁻²	10.3%	25 h @ 115 cd m ⁻²	[17]
Post-treatment	Inorganic Halide	ZnBr ₂	CsPbBr ₃	Green	76%	518 nm (18 nm)	76 940 cd m ⁻²	16.48%	136 min @ 0.6 mA/cm ⁻²	[272]
Post-treatment	Inorganic Halide	KI	CsPbI ₃	Red	96%	640 nm (31 nm)	–	23%	10 h @ 200 cd m ⁻²	[189]
Post-treatment	Conjugated Molecular Multipods	TPBi	(FA _{0.9} CA _{0.1})PbBr ₃	Green	100%	531 nm (20 nm)	10 908 cd m ⁻²	26.1%	5 h @ 100 cd m ⁻²	[6]
Post-treatment	Organic Host	mCP	CsPbBr ₃	Blue	94.7%	462 nm (29 nm)	142.87 cd m ⁻²	6.2%	201 s @ 10 cd m ⁻²	[3]

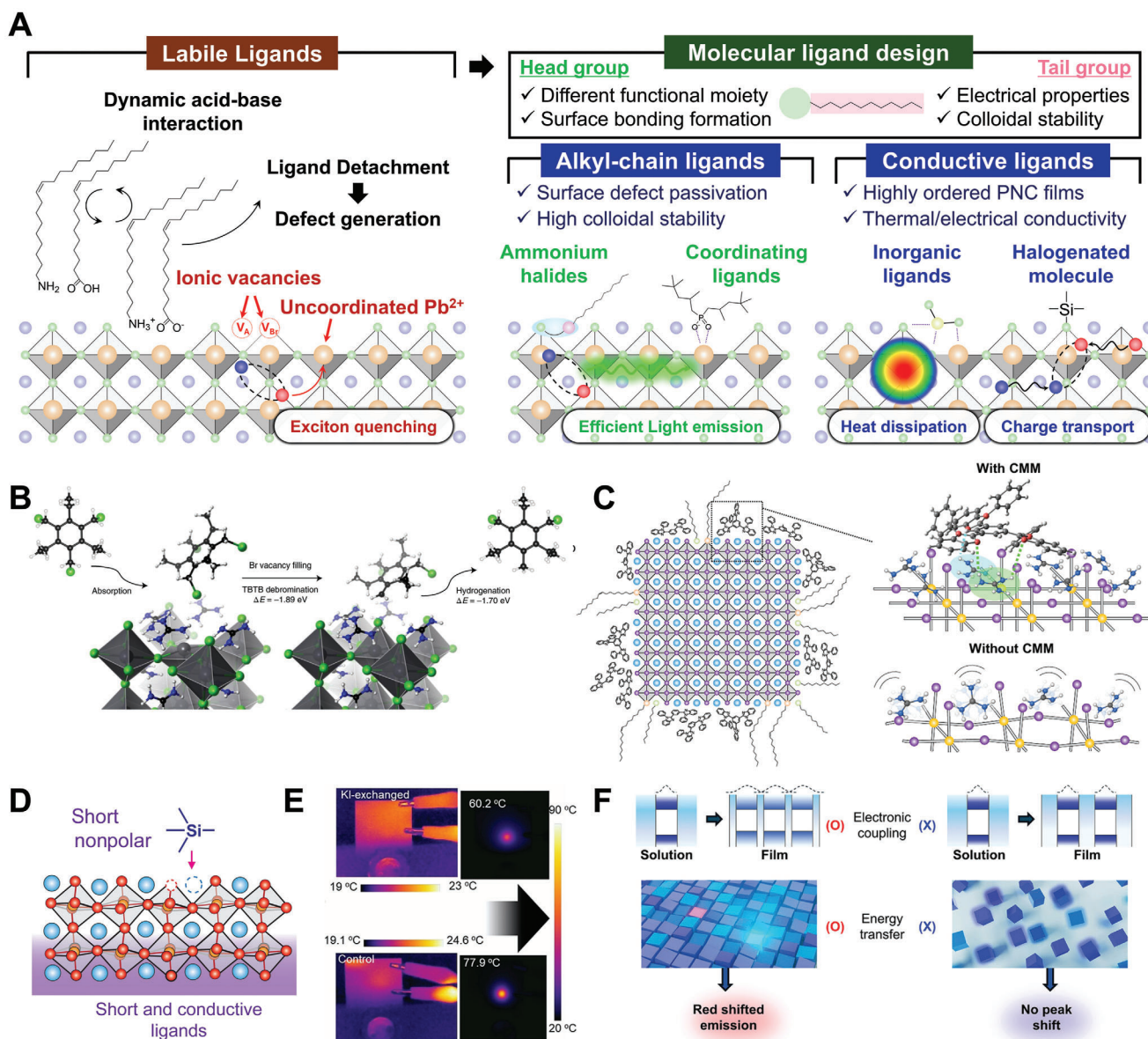


Figure 12. A) Schematic illustration of surface reconstruction for efficient and stable electroluminescence of PNCs. Surface defects can be generated by desorption of labile ligands, which induces exciton quenching. Both the head group and tail group of molecular ligands for surface reconstruction can be designed. Surface reconstruction by alkyl-chain ligands can eliminate surface defects while maintaining colloidal stability. Conductive ligands are particularly effective at enhancing the thermal transport and electrical properties of PNCs. B) Mechanism of halide vacancy passivation in $FA_{0.9}GA_{0.1}PbBr_3$ PNCs by a TBTB molecule. Reproduced with permission.^[26] Copyright 2021, Springer Nature. C) Schematic illustration showing suppressed dynamic motion of PNC lattice by CMMs. Reproduced with permission.^[6] Copyright 2024, Springer Nature. D) Schematic illustration of surface reconstruction with enhanced ordering by halogenated molecule, TMS-X. Reproduced with permission.^[187] Copyright 2023, AAAS. E) Infrared-thermal-imaging pictures of PNC devices treated with and without an inorganic ligand (KI) at their highest temperature. Reproduced with permission.^[189] Copyright 2021, WILEY-VCH. F) Schematic illustrating QD-QD interaction related to emission spectrum shifts, in QD-only film (left) and QD-mCP solid solution (right). Reproduced with permission.^[3] Copyright 2024, WILEY-VCH.

($T_1 = 3.3$ eV), significantly improved EQE.^[170] However, for green and red PNC-LEDs with lower bandgaps ($E_g \approx 2.3$ and 2.0 eV), exciton quenching by the triplet energy of naphthalene groups becomes negligible. Therefore, using 2-naphthalene sulfonic acid (NSA) as a ligand enhances charge transport capability, achieving high EQEs of 19.2% for green and 26.04% for red PNC-LEDs.^[171,172]

Engineering X-site species also stabilizes PNC surfaces. For instance, post-treatment with di-dodecyl dimethyl ammonium fluoride (DDAF) passivates bromine vacancies by filling them with fluoride ions, which form a type I junction at the surface, and ultimately suppress carrier trapping and thermal quenching.^[173] Thiocyanate ions (SCN^-) filled Cl^- vacancies and removed mid-gap states without changing the emission spectrum.^[174]

5.3.2. Incorporation of Strongly-Coordinating Ligands

Uncoordinated Pb^{2+} ions, primarily generated by halide vacancies, act as severe exciton quenching sites. Passivating them is essential to realize high-efficiency PNCs. A common strategy is to employ ligands that possess lone pair electrons in the head group, which can neutralize the uncoordinated Pb^{2+} ions. This approach requires the appropriate design of the ligand's functional moiety because it directly influences the coordination strength with Pb^{2+} ions. For example, lone pair electrons in nucleophile moieties such as $\text{P}=\text{O}$ (from phosphine oxide), $\text{O}=\text{S}=\text{O}$ (from sulfone), $\text{C}=\text{O}$ (ketone), and deprotonated anionic moieties such as CO_2^- (from acetic acid), PO_3^{2-} (from phosphonic acid), and SO_3^{2-} (from sulfonic acid) strongly coordinate lead atoms and thus suppress the formation of undercoordinated Pb^{2+} . While deprotonated oleic acid also has a COO^- moiety with lone pair electrons, its long alkyl chain and relatively weak carboxylate group result in less-stable binding. Therefore, elaborate design of both head and tail groups is essential.

Strongly-coordinating ligands not only passivate defects but also etch the PNC surface by removing imperfect octahedra, enabling to achieve nearly perfect PNC surface. Tryptophan (TRP) with amino acid moiety has been shown to not only coordinate with Pb^{2+} through its carboxylate group but also to form an additional strong cation- π interaction between the indole ring of TRP and Pb^{2+} . Through these multidentate bindings, TRP showed a high adsorption energy of 4.14 eV and the elimination of trap states within the bandgap of CsPbI_3 PNCs. TRP also reconstructed the PNC surface by removing imperfect PbX_6 octahedra due to strong binding with Pb^{2+} . The presence of aromatic ring moiety improves electrical properties, resulting in pure-red PNC-LEDs with an outstanding L_{max} of $12\,910\text{ cd m}^{-2}$ at 635 nm with an EQE of 22.8%.^[175] Diisooctylphosphinic acid (DSPA), which has stronger adsorption energy on the PNC surface compared to oleate species, suppressed the formation of uncoordinated Pb^{2+} ions and iodine Frenkel defects.^[176] Sequential treatments, including surface etching using hydroiodic acid, and the addition of tributylmethylphosphonium iodide (TMPI), further increased surface passivation. LEDs that used such surface-reconstructed PNCs achieved a remarkable EQE of 28.5% and an operational lifetime of 30.4 h. This result demonstrates the value of suppressing vacancy formation, etching away imperfect octahedra, and ensuring near-perfect surface treatment.^[176]

Polymeric ligands that integrate various functional moieties in the polymer chain have also been used to improve luminescent properties of PNCs. Especially, the polymer matrix significantly enhances the material- and operational-stability of PNC films. Poly(maleic anhydride-*alt*-1-octadecene) (PMA), functionalized with maleic anhydride rings, formed strong $\text{Pb}-\text{O}$ bonds, enabling to yield thermodynamically stable β - CsPbI_3 nanocrystals.^[177] Additionally, the 1-octadecene moieties formed a hydrophobic layer that protected against polar solvents during purification. Benefiting from the stabilized phase and surface passivation, PNC-LEDs with cross-linked PMA achieved a remarkable T_{50} of 317 h.^[177] Further design of the side chains in polymeric ligands with incorporating a combination of dispersing alkyl chains and aromatic functional groups significantly enhanced colloidal stability and facilitated charge transport. This resulted in a high EQE_{max} of 23.6% and a long operational life-

time of ≈ 2500 min.^[178] These results emphasize the importance of designing ligands that have a head group that strongly coordinates Pb^{2+} ions and a tail group that effectively assembles PNCs by controlling steric hindrance while maintaining excellent electrical properties and colloidal stability.

5.3.3. Hetero-Interface Passivation

Hetero-interface passivation between the PNC active layer and CTLs is an effective surface reconstruction strategy. This strategy involves inserting interlayers that provide additional passivation to both upper and underlying layers of PNCs, along with improving charge balance. Hetero-interface passivation can also influence PNC organization and packing when applied to underlying layers.

Depositing a layer of 1,3,5-tris(bromomethyl)-2,4,6-triethylbenzene (TBTB) on $\text{FA}_{0.9}\text{GA}_{0.1}\text{PbBr}_3$ PNC film facilitated defect passivation by supplying Br^- anions that were released by debromination of the TBTB molecules (Figure 12B).^[26] In the presence of acid ligands, the de-brominated TBTB undergoes hydrogenation, which stabilizes the TBTB molecule. When deposited between the PNC film and ETL, the insulating TBTB layer slows down electron injection, improving charge balance. PNC-LEDs with the TBTB interlayer achieved a current efficiency of 108 cd/A and an EQE of 23.4%, which was the highest PeLED efficiency in 2021.

Other interlayers containing moieties that have lone pair electrons (e.g., $\text{P}=\text{O}$, $\text{S}=\text{O}$, and $\text{C}=\text{O}$) passivate uncoordinated Pb^{2+} by coordination bonding, and thereby also boost luminescence efficiency.^[179] Bilateral passivation using a diphenylphosphine oxide-4-(triphenylsilyl)phenyl (TSPO1) interlayer improved EL efficiency (EQE_{max} = 18.7%) by a virtue of phosphine oxide moieties what has high bond order to Pb^{2+} .^[179]

Metal halide-based interlayers are also used for hetero-interface passivation. Incorporating a potassium iodide (KI) layer beneath CsPbI_3 PNC films reduced the contact angle of the PNCs solution on the KI layer, owing to the strong interaction of K^+ with the I^- in $[\text{PbI}_6]^{4-}$ octahedra.^[180] This facilitated dense and uniform PNC organization accompanied by improving film roughness. Furthermore, the KI interlayer has high thermal and electrical conductivity, and thereby improves the thermal resistance of PNC films and induced balanced charge injection; these changes also suppress Joule heating and Auger recombination. Using a KI interlayer, high-efficiency PNC-LEDs with deep-red emission were demonstrated, with an EQE of 21.8%.^[180] Similarly, various alkali-metal bromides (e.g., LiBr, NaBr, KBr) also developed interfaces that improved the crystallinity of PNCs and promoted tight packing of them.^[181]

5.3.4. Perovskite Lattice-Strengthening

The ionic nature of halide perovskite materials induces large-amplitude atomic displacement and anharmonic vibration modes, resulting in dynamic disorder that screens excitons and thus reduces radiative recombination.^[182–185] However, few studies have tried to control the lattice dynamics of perovskite materials to reduce non-radiative recombination.

Recently, a novel approach was developed, which employs π -conjugated molecular multipods (CMMs) with multiple binding sites and relatively large molecular size, to suppress dynamic disorder at the perovskite surface. (Figure 12C).^[6] CMMs have nucleophile functional groups, which form multiple hydrogen bonds with FA and GA cations with a favorable horizontal orientation on the surface. This multi-site hydrogen bonding between nanocrystalline perovskite surface, accompanied by van der Waals interaction, stiffens the perovskite lattice (lattice-strengthening) and thus increases the in-plane elastic modulus of perovskite slab. A perovskite lattice with CMMs adsorbed showed a blueshift in low-frequency vibrational modes, especially PbBr₆ octahedral distortion, and rotation, which is clear evidence of suppressed dynamic disorder. Additionally, the effects of lattice strengthening predominantly occur at the surface, so they can be particularly effective in nanocrystalline perovskites, which have a high surface-to-volume ratio.

The trends of the improvement in PL/EL efficiency of the nanocrystalline perovskite (PC perovskites and PNCs) matched well with the increased elastic modulus; this result indicates that surface reconstruction utilizing lattice-strengthening approach is universally-applicable to all types of perovskite emitter. As a result, FA_{0.9}GA_{0.1}PbBr₃ PNCs that used a lattice-strengthening TPBi CMM showed a near-unity PLQY and an EQE of 26.1%. This perspective will provide a novel strategy to overcome the inherent limitation of nanocrystalline perovskite.

5.4. Interparticle Engineering Between PNCs

The organic alkyl chains of the ligands provide colloidal stability and prevent damage by flocculation solvents and moisture. However, in LED operation, these organic mediums can hinder charge transport between PNCs; this necessitates higher voltages to achieve the same brightness. Consequently, ion migration is facilitated, leading to accelerated degradation of LED. Additionally, Joule heating can accelerate the detachment of dynamic ligands. To improve EL efficiency and stability in PNC-LEDs, the charge carrier mobility of PNCs must be increased, and efficient heat dissipation within PNC films must be promoted. These goals can be achieved using two approaches: 1) Enhanced ordering between PNCs and 2) Minimized organic medium in PNC films.

5.4.1. Enhanced Ordering between PNCs

Size variations in PNCs lead to irregular arrangements, which increase average interparticle spacing, and the charge-injection barrier. In contrast, enhanced ordering of PNCs can reduce interparticle distance, and thereby significantly improve charge transport through PNC films. This improvement can promote balanced charge injection, and thus suppress Auger recombination and consequently reduce efficiency roll-off. To achieve periodic ordering of PNCs, they must be engineered to have uniform size. Strong coupling ligands also decrease interparticle distance and increase the ordering of PNCs.

Trimethylsilyl halides (TMS-X) were developed to enhance PNC ordering and passivate surface bromine defects (Figure 12D).^[22] TMS-X reacts with protic agents by a nucleophilic reaction that generates HX, which dissolves PNCs that

have poor ligand coverage and regulates the size of PNCs. Narrowed size distribution by bromotrimethylsilane (TMSBr) treatment induces long-range ordering in PNC films, thereby reducing dot-to-dot distance and causing a redshift in PL emission due to strong coupling. The ordered PNC films had 3.6 times higher conductivity ($4.5 \times 10^{-4} \text{ S m}^{-1}$) than the control film and had improved thermal stability. This enhancement in ordering achieved an impressive operational lifetime, with a T_{90} of 780 h, which is the longest operational lifetime reported for PNC-LEDs to date.^[22] Similarly, iodotrimethylsilane (TMSI), also provides iodine ions to passivate undercoordinated Pb²⁺ ions.^[186] TMSI-treated PNC film achieved a PLQY > 90% and had an order of magnitude increased conductivity due to enhanced compactness; this strategy yielded red-emitting (656 nm) PNC-LEDs that had EQE \approx 23%.^[186]

Liquid TMSBr is also compatible with underlying HTLs, so it enables self-assembly of PNCs down to the monolayer limit with increased ordering.^[187] TMSBr-treated monolayer PNC-LEDs achieved a high EQE of 11.9% with deep-blue emission at 463 nm, which approaches the Rec. 2020 blue standard.^[187]

5.4.2. Minimized Organic Medium in PNCs

Inorganic halides such as NaBr or ZnBr₂ offer superior electrical and thermal conductivity while effectively passivating halide vacancies and undercoordinated Pb²⁺ ions. Minimizing the organic medium by using inorganic halides significantly improves the brightness and stability of PNC-LEDs. However, since they lack alkyl chains, and therefore do not provide colloidal stability; also, sometimes polar solvent is needed to disperse PNCs treated with inorganic halides.^[188]

Bipolar shell resurfacing of PNCs using NaBr demonstrated higher PLQY than organic ligand-passivated PNCs, regardless of PNC size.^[188] The addition of a polar solvent like DMF aided the colloidal dispersion of PNCs. NaBr-terminated PNCs with uniform size distribution assumed a close-packing configuration. They showed superior carrier mobility ($\geq 0.01 \text{ cm}^2 \text{ V}^{-1} \text{ s}^{-1}$) and increased thermal stability compared to the control samples. Bipolar shell PNCs obtained using NaBr treatment demonstrated an EQE of 22% in green PNC-LEDs and 12.3% in blue PNC-LEDs.

Stable α -phase CsPbI₃ PNCs were achieved by solid-state ligand exchange with KI.^[189] KI strengthened interdot interactions by favoring mechanical coupling, and induced strain at the PNC surface; these changes significantly improved phase stability. It also improved thermal transport properties, so the PNC film effectively dissipated Joule heating during device operation (Figure 12E), and thus improved operational stability.^[189]

The function of inorganic halides on PNC surfaces was further elucidated using ZnBr₂. The dielectric constant of ZnBr₂ closely matches that of CsPbBr₃, weakening the dielectric confinement effect and decreasing the exciton binding energy in ZnBr₂-treated CsPbBr₃ PNCs. This reduction in exciton binding energy contributes to the suppression of Auger recombination. Additionally, ZnBr₂ relocates charges near the VBM from the PNC core to the surface; this process reduces carrier accumulation within the PNCs and further inhibits Auger recombination. The PNC-LEDs

treated with ZnBr_2 had a peak emission wavelength of 469 nm, with L_{max} of 12 060 cd m^{-2} and EQE_{max} of 10.3%.^[17]

5.4.3. Decoupling of Perovskite for Deep-Blue Emission

The development of deep-blue PeLEDs remains challenging due to difficulties in achieving the desired color purity. Engineering interparticle interactions can help achieve deep-blue emission with high efficiency. Two primary strategies to obtain deep-blue emission are using mixed halide compositions of Br^- and Cl^- , and inducing strong quantum confinement effects. However, incorporating chloride leads to high defect densities and severe halide segregation.^[190,191] Additionally, strong quantum confinement requires low- or medium- n phases ($n = 2, 3$)^[99] or ultra-small crystal sizes < 4 nm,^[80] which result in increased surface defects and reduced stability. Consequently, achieving deep-blue PeLED emission < 463 nm, as required by the Rec. 2020 color standard, is uncommon.

Emission at 462 nm has been realized using Cl-free perovskite quantum dots while minimizing size reduction to prevent defective surfaces. This approach addresses the intrinsic redshift in the perovskite emitting layer caused by electronic coupling and energy transfer (Figure 12F). A highly diluted perovskite quantum dots in an organic solid solution prevented these particle interactions and enabled a 7 nm blueshift and a high EQE_{max} of 6.2% at 462 nm.^[3] In this system, the semiconducting organic material N,N' -dicarbazolyl-3,5-benzene (mCP) was used to mitigate insulating properties. These results suggest that electronic coupling and energy transfer toward lower bandgaps impede deep-blue emissions; such effects should be considered not only in perovskite quantum dots but also in low- n Q2D and strongly confined in situ PNCs.

6. Tandem PeLEDs

Tandem structures, which stack multiple light-emitting units (LEUs), enable a multifold increase in EQE ;^[7,192,193,194] and are widely utilized in commercial vacuum-deposited OLED technologies. Theoretically, if the charge generation efficiency (ξ_{CGE}) and charge balance factors of each LEU are both 1, the EQE of the tandem LED can be derived by linearly adding the EQEs of the stacked LEUs. The EQE of the tandem device can be calculated using the following equation:

$$\text{EQE}_{\text{tandem}} = \xi_{\text{CGE}} \times \{\text{EQE}_{\text{LEU1}} + \text{EQE}_{\text{LEU2}}\} \quad (4)$$

where ξ_{CGE} is a charge generation efficiency, defined as the number of electrons or holes generated at the charge generation layer (CGL) divided by the number of electrons or holes injected from the electrode. Therefore, incorporating tandem structures into PeLEDs enables the achievement of higher EQE than single-stack devices, which are constrained by theoretical limits. Furthermore, by enabling simultaneous light emission from multiple LEUs, tandem structures reduce the current density required to achieve a given brightness. This reduction in current density significantly lowers electrical stress on individual PeLED units, thereby mitigating degradation factors such as ion migration and

redox reactions during operation. As a result, tandem PeLEDs provide the dual advantages of extended operational lifetimes and increased EQE .

While vacuum deposition allows for easy stacking of LEUs in OLEDs, the EQE of vacuum-deposited PeLEDs remains relatively lower than that of solution-processed PeLEDs, with the highest reported EQE_{max} only at 16.4%.^[14,66] This limitation hinders the achievement of high EQE_{max} on tandem PeLEDs. Additionally, as the solvents can damage or wash away the underlying layers, the realization of all-solution-processed tandem PeLEDs is particularly challenging.

To overcome these limitations, hybrid tandem structures combining a solution-processed PeLED (bottom) and a vacuum-deposited OLED (top) have been introduced.^[195–197] However, the two LEUs use different types of emitters, so they have generally dissimilar EL spectra shapes and J - V - L characteristics, possibly leading to broadened FWHM and unstable EL spectrum during the device operation.

Recently, a valley-centre tandem PeLED has been developed, where both the microcavity effect and the charge balance of each LEUs were optimized (Figure 13A).^[197] The microcavity effect enhances constructive interference of the light emission within the tandem device when the thickness of each layer is precisely controlled. Optical simulations show that the narrowest FWHM is achieved at the valley point with an optimized layer thickness (Figure 13B). If the thickness deviates from the optimized point, a non-cavity structure results in a broadened FWHM. In contrast, the valley-centre tandem PeLED exhibits an emission spectrum with a narrow FWHM < 28 nm (Figure 13C).

Optimizing the charge balance of each LEU is challenging but critical to maximizing the EQEs of the LEUs. To achieve a near-perfect charge balance, a bi-electron transport layer of TPBi and ZADN was employed because ZADN promotes electron injection due to high electron mobility. Based on this modification, an ultra-high-efficiency tandem PeLED with an EQE of 37.0% was obtained, whereas an imbalanced charge configuration with TPBi resulted in an EQE of 26.8% (Figure 13D).

Time-resolved EL spectra during the rising time of EL intensity showed stable emission spectra; this result indicates that both perovskite and organic emitters contribute uniformly to stable LED. In addition, fast on-off EL response and stable EL spectra under different voltages solidify that the charge balance of the two LEUs in valley-centre tandem PeLEDs is nearly perfect. Furthermore, the tandem structure reduced electrical stress to exhibit the same brightness, so the operational lifetime is much longer in the valley-centre tandem PeLEDs than in single PeLEDs (Figure 13E).

This approach, which simultaneously optimizes the microcavity effect and charge balance, offers a promising method to use hybrid tandem device structures (nanocrystalline PeLED stacked with other LEUs), and to increase EQE while maintaining the advantage of the narrow FWHM of nanocrystalline perovskites.

Furthermore, white tandem LEDs can be fabricated by modulating the emission wavelength of each LEU. For example, the combination of a sky-blue perovskite LEU and an orange organic LEU produces white light with a color temperature of 3756 K and a high EQE of 24.3%.^[198] The incorporation of a red organic emitter allows further shifts in the CIE coordinates, resulting in white light with a color temperature of 2522 K and an EQE of

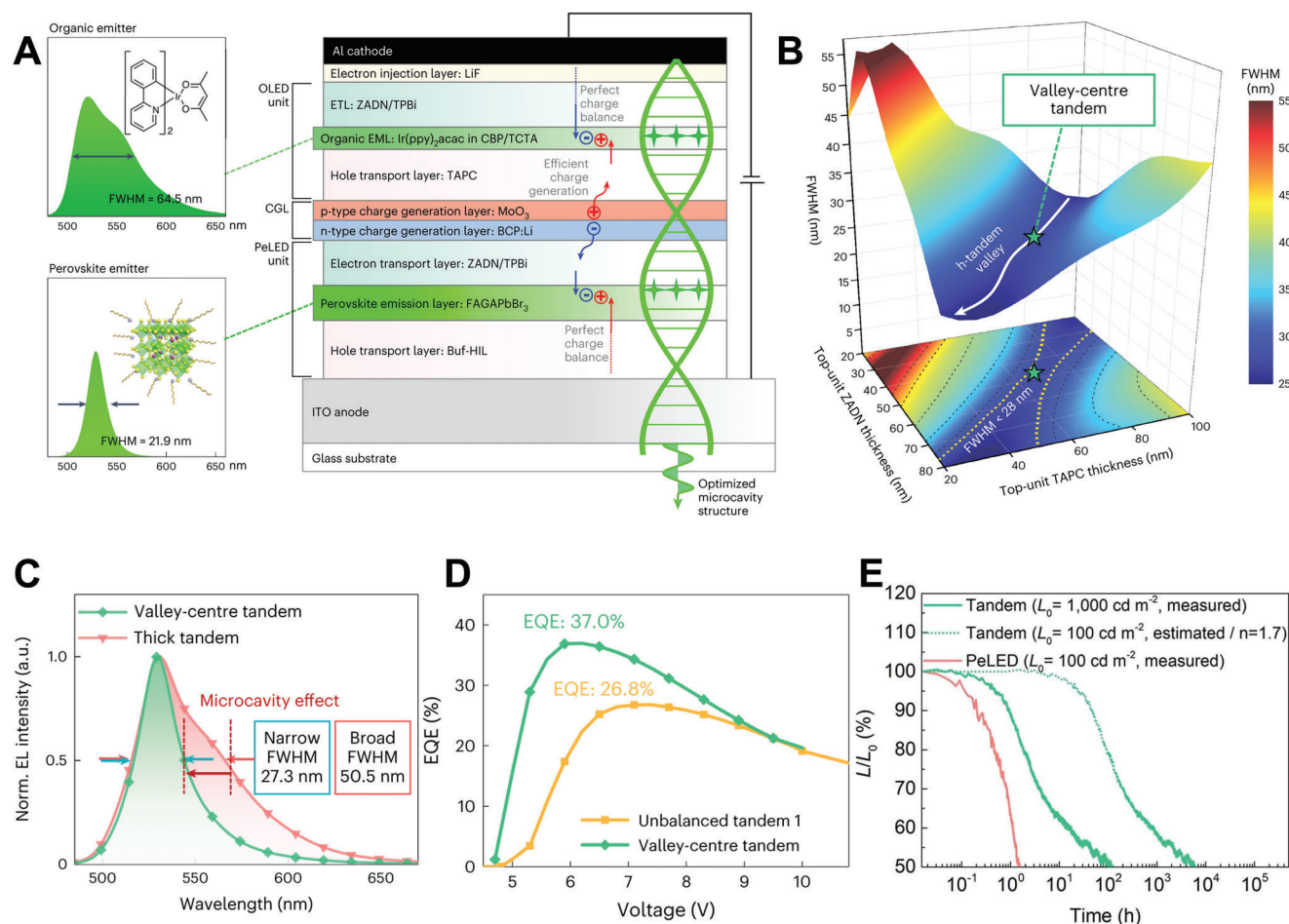


Figure 13. A) Device structure of valley-centre tandem PeLEDs. The EL spectra of single OLED and PeLED were shown. B) Optical simulation of FWHM according to the thickness of charge transport layers of light-emitting units. C) EL spectra of optimized valley-centre tandem and non-cavity structure. The FWHM is shown. D) EQE of balanced valley-centre tandem LED and unbalanced tandem LED. E) Operational lifetime of OLED, PeLED, and valley-centre tandem PeLED. Reproduced with permission.^[197] Copyright 2024, Springer Nature.

23.9%. Another way to obtain white emission is by combining the primary colors of light (red, green, and blue). Stacking three R/G/B-emitting perovskite LEUs leads to a monolithic R/G/B white PeLED, yielding pure white emission with a CIE coordinate of (0.33, 0.33).^[199] Due to the narrow FWHM of each perovskite LEU, a prominent color gamut is achieved, covering 130% of the National Television System Committee (NTSC) standard.

7. Summary of Trends in Nanocrystalline-PeLEDs

This section summarizes major trends and strategies to achieve efficient PeLEDs using each of the three types of nanocrystalline perovskite. (Figure 14).

7.1. Polycrystalline Perovskite

(Phase 0) The initial PC PeLEDs, which lacked grain modulation, had sub-micrometer grains with highly defective surfaces and grain boundaries. These large grains and defects caused luminescence quenching due to thermal ionization of electron-hole

pairs (or excitons) at room temperature and non-radiative recombination in trap states.

(Phase 1) To overcome the material limitations of PC perovskites, such as low exciton binding energy and long exciton diffusion length, a strategy was developed to increase charge confinement by obtaining grains of size < 100 nm. Small and uniform grains were obtained by inducing instantaneous nucleation during the crystallization process by TPBi-based nanocrystal pinning. As a result, a high EQE of 8.53% was reported; this result suggests the possibility of developing high-efficiency PeLEDs.^[10]

(Phase 2) During the development of PeLEDs, two critical challenges arose: to overcome the short device lifetime and to increase efficiency. However, ionic defects in perovskites significantly hindered progress on these challenges. Therefore, a strategy to effectively suppress grain boundary defects was developed. A small amount of large ammonium cation added to the precursor solution formed a 2D phase within the grain; this structure effectively inhibited ion migration, which would lead to device degradation. Additionally, this method successfully suppressed the overshoot phenomenon caused by the formation of an internal electric field under voltage

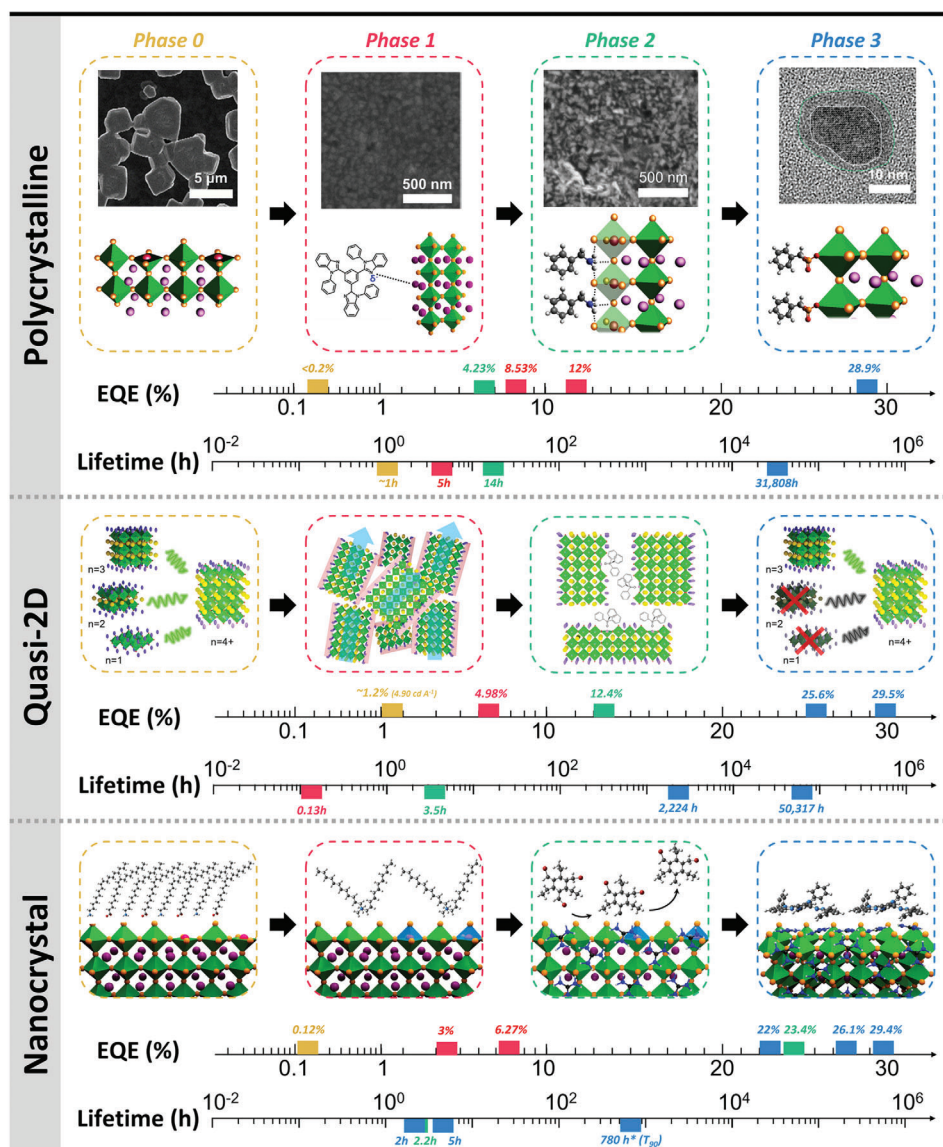


Figure 14. Development of PC, Q2D, and PNC-PeLEDs is divided into four phases. **(Polycrystalline)** Phase 0: sub-micrometer grain with defective surface, and its SEM image. Reproduced with permission.^[10] Copyright 2015, AAAS. **Phase 1:** Small grain size < 100 nm obtained by additive-based nanocrystal pinning and its SEM image. Reproduced with permission.^[10] Copyright 2015, AAAS. **Phase 2:** 3D/2D hybrid perovskite with benzylamine, and its SEM image. Reproduced with permission.^[79] Copyright 2020, Springer Nature. **Phase 3:** in situ core/shell perovskite with BPA, and its TEM image. Reproduced with permission.^[14] Copyright 2022, Springer Nature. **(Quasi-2D)** Phase 0: energy transfer from low-*n* phases to high-*n* phase in the early stage of Q2D perovskite. **Phase 1:** facilitated charge transfer by randomly orientated Q2D perovskite. **Phase 2:** defect passivated, narrowed *n*-distribution Q2D perovskite by with TPPO. **Phase 3:** removal of defective and insulating low-*n* phases (*n* = 1 and *n* = 2). **(Nanocrystal)** Phase 0: PNC with excess long chain ligand with defective surface. **Phase 1:** ligand engineered PNC with DDAB. **Phase 2:** Comprehensive defect passivation using GA and TBTB. **Phase 3:** lattice-strengthened PNC using π -Conjugated molecular multipods. Operational lifetime using accelerated T_{50} is calculated as of $LT_2/LT_1 = (L_1/L_2)^n$ with $n = 1.65$.

operation and thereby extended the device lifetime from ≈ 38 min to ≈ 14 h.^[79]

(Phase 3) The in situ core/shell PNC system maximizes defect passivation by utilizing benzyl phosphonic acid to strongly bind with uncoordinated Pb^{2+} . This system passivates defects at grain boundaries and within the crystal, splitting the large grains into nanograins, and achieving an optimal grain size re-

duced to ≈ 10 nm. It simultaneously enhances exciton binding energy, reduces defect density, and maintains high charge mobility, even as the grain size decreases to ≈ 10 nm and more surfaces and grain boundaries are generated. As a result, a high EQE of 28.9% and an extended device lifetime of 31 808 h (T_{50} , at $L_0 = 100$ cd m⁻²) were realized. These traits opened the possibility of commercialization.^[14]

7.2. Quasi-2D Perovskite

(Phase 0) The first reported Q2D-PeLEDs using PEA as a spacer cation laid the foundation for further developments in the field.^[11] The methods focused primarily on the formation of perovskites that had a multi-quantum-well structure and energy funneling of excitons.^[11,84] However, the low charge mobility caused by the large amount of insulating spacer cations hinders charge transport in PeLEDs, highlighting the need for strategies to overcome the insulating nature of Q2D perovskites.

(Phase 1) To overcome the low charge mobility, the orientation of the planar perovskite layers was modified. The adoption of the nanocrystal pinning process significantly increased charge transport by randomizing the orientation of perovskite layers. This randomization formed a 3D network of charge transport paths overcoming barriers of insulating spacer cations and thereby facilitated charge transport across the layers.^[115]

(Phase 2) Introduction of various additives and engineering of the spacer cations passivated defects and increased the overall efficiency. For example, introducing TPPO to Q2D perovskite significantly reduced defect density and narrowed the distribution of n -phases. As a result, reduced non-radiative recombination and fast and efficient energy funneling led to notable improvements with EQE_{max} of 14% and L_{max} of 45 000 cd m^{-2} .^[69]

(Phase 3) By concentrating the Q2D perovskite phases primarily in high- n phases while effectively removing low- n phases ($n = 1$ or 2), further advances were achieved. This removal of defective and insulating low- n phases, which are key contributors to instability, resulted in highly efficient energy funneling and radiative recombination of excitons. Removing low- n phases can be accomplished through the NCP process during spin-coating^[115] or by adding additives that suppress the formation of PEA agglomerates.^[108] This more recently, selective removal of $n = 1$ and 2 phases using hexylamine led to EQE_{max} of 29.5% and an extended operational lifetime of 50317 h.^[21]

7.3. Perovskite Nanocrystal

(Phase 0) Following the foundational patents on PNCs in 2014,^[125,126] the spatially confined structure of PNC attracted attention due to high PL efficiency. However, the early development of PNC-LEDs was limited by ligand detachment and the insulating nature of long alkyl ligands, caused by inadequate purification and surface passivation.^[12]

(Phase 1) The purification process for PNCs using ethyl acetate as a washing solvent was introduced to effectively reduce ligand density, thereby improving charge injection into PNCs. This approach dramatically increased the EQE_{max} of PNC-LED from 0.12% to 6.27%.^[137] Additionally, a ligand exchange procedure that replaced dynamically-binding ligands (e.g., oleylamine/oleic acid) with a strongly-binding ligand (e.g., DDAB) further enhanced the PLQY from 49% to 71%.^[159] These two strategies laid the foundation for material modifications in PNCs, and are still widely utilized to achieve high-efficiency PNC-LEDs.

(Phase 2) Due to the ionic nature of perovskite crystals and the dynamic binding of ligands, defect formation within the core and at the surface of PNCs is still inevitable, hindering EQE improvements in PNC-LEDs. A comprehensive defect-passivation strat-

egy that uses GA dopant in both the bulk and surface of PNCs and a TBTB interlayer on spin-coated PNC films, was developed to simultaneously stabilize core-crystal and mitigate surface defects in PNCs as well as defects on the surface of the PNC film. This approach significantly increased EQE to 23.4%.^[26]

(Phase 3) The use of excess ligands in PNCs is essential to maintain colloidal stability, but these ligands hinder charge transport between PNCs and accelerate the degradation of PNC-LEDs under device operation, resulting in a shorter operational lifetime than PC-PeLEDs. To overcome these limitations, efforts have focused on improving particle ordering and minimizing the amount of insulating ligands. These approaches have resulted in enhanced thermal and electrical conductivity of PNC films, resulting in an extended operational lifetime of $T_{90} \approx 780$ h.^[22] Nevertheless, the ionic nature of perovskites induces dynamic disorder within the lattice, which interferes with the radiative recombination of charge carriers. To address this issue, CMMs with multiple moieties that bind to the A-site cations of perovskites were designed. These CMMs enhance lattice stability and reduce dynamic disorder on the perovskite nanocrystal (PNC) surface, significantly improving both the efficiency and stability of PNC-LEDs, achieving an EQE of 26.1%. At the same time, this approach provides a new perspective for the development of nanocrystalline perovskites.^[6]

8. Remaining Challenges

Despite significant advances in PeLEDs that use nanocrystalline perovskites, several challenges must be overcome to compete with conventional OLEDs. Key challenges include achieving $\text{EQE}_{\text{max}} > 30\%$, preventing efficiency roll-off during high-brightness operation, and significantly increasing operational stability to $T_{50} \approx 10^6$ h at an initial luminance of 100 cd m^{-2} (Figure 15).

8.1. Achieving EQE > 30%

Even with perfect passivation of perovskites and an electrically-balanced device structure, optical losses within the LED (e.g., substrate mode, waveguided mode, surface plasmon mode) typically limit the EQE_{max} to $< \approx 30\%$. To achieve an ultra-high EQE > 30% like OLEDs requires surpassing the theoretical efficiency limits of PeLEDs by focusing on outcoupling efficiency.^[200] Specifically, photon recycling (i.e., re-emission of reabsorbed photons)^[201] in polycrystalline PeLEDs with sufficient thickness (e.g., ~ 300 nm) can increase outcoupling efficiency by up to 30%; this process accounts for the recent high EQE_{max} values achieved without additional outcoupling enhancement structures. However, to further increase outcoupling efficiency beyond this improvement, additional strategies are required.

Recent academic research on OLEDs has achieved an EQE $\approx 40\%$ in a single device aligning the emitting dipole orientation parallel to the substrate because this arrangement increases the outcoupling efficiency.^[202] To achieve similarly high EQE_{max} , several strategies have been used in nanocrystalline PeLEDs to increase the outcoupling efficiency. First, the perovskite can also tune the emitting dipole orientation, typically by using parallel-stacked nanoplatelet grains with a high aspect ratio.^[203] Other

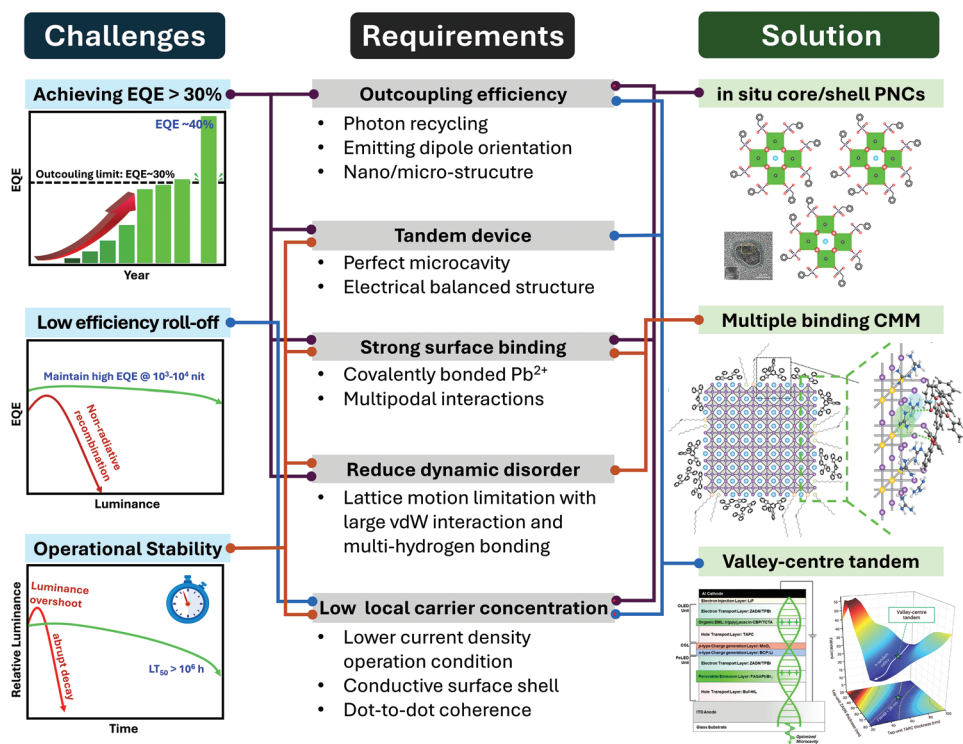


Figure 15. Problems and challenges for the nanocrystalline perovskite LEDs, requirements to overcome, and their potential solutions. The figure of in situ core/shell PNCs is adapted with permission from [14] Copyright 2022, Springer Nature. The figure of multiple binding CMM is adapted with permission from [6] Copyright 2024, Springer Nature. The figure of the valley-centre tandem is adapted with permission from [197] Copyright 2024, Springer Nature.

light-management techniques can be implemented. For example, nanostructures or microstructures that induce light scattering can be introduced into the substrate,^[204] or CTLs,^[205] or by using scattered sub micrometer-scale perovskite grains.^[54,206]

The recent report of a tandem PeLED that has high efficiency (EQE ≈ 37%) provides a new way to increase the EQE_{max}.^[197] By stacking different types of emitting units (i.e., OLED unit and PeLED unit) and achieving a structure that is perfectly balanced both optically and electrically, a high EQE_{max} even > 40% becomes possible. In the reported design, solution-processed thin PNC-PeLED bottom units were engineered to maintain sufficient transmittance of top unit emission, while the top unit was vacuum-deposited OLED. However, other combinations of emitting units, such as PC-PeLED, Q2D-PeLED, and vacuum-deposited PeLEDs, can be used to fabricate highly efficient nanocrystalline tandem PeLEDs, provided that the transmittance of the top unit emission through the bottom unit is ensured.

8.2. Low Efficiency Roll-Off

Maintaining high EQE at higher current densities is essential, especially because AR/VR displays require luminance of 10⁵-10⁶ cd m⁻².^[19] However, in nanocrystalline perovskites, as nanograins or nanocrystals decrease down to ≈10 nm, fast non-radiative Auger recombination becomes dominant, leading to a significant efficiency drop at high charge carrier density.^[30] The Auger recombination rate increases significantly as exciton binding en-

ergy increases,^[207] achieving high radiative excitonic recombination while maintaining low Auger recombination rates remains a significant challenge. Nevertheless, some strategic approaches are available.

Excitons in nanocrystalline perovskites are confined by both spatial and dielectric confinement.^[207] Surrounding organic materials (such as passivators in PCs, spacer cations in Q2Ds, and ligands in PNCs) create a low-dielectric environment compared to the high-dielectric perovskite crystal. This dielectric confinement increases the exciton binding energy and the probability of Auger recombination. By increasing the dielectric constants of the surrounding materials, the dielectric-confinement effect can be suppressed, thereby reducing exciton binding energy while maintaining spatial confinement.^[17,30]

Insulating organic molecules used in nanocrystalline perovskites typically require thin emissive layers to compensate for slow charge injection and transport. However, these thin emissive layers result in increased local carrier concentration, which facilitates Auger recombination.^[208] To address this issue, thicker emissive layers and highly conductive nanocrystalline perovskites are needed to enable efficient charge transport. In PNC-LEDs, using short aromatic ligands, such as aniline hydroiodide combined with halide trimethylsilane, promotes dot-to-dot coherence and long-range order.^[22] This ordered emissive layer increases charge carrier mobility by more than an order of magnitude, and maintains an EQE of 20% at 1000 cd m⁻² with minimal efficiency roll-off.^[22] Additionally, in situ, core/shell PNC that use BPA demonstrates excellent charge carrier

mobility, and thus allow for an emissive layer thickness of 270 nm and achieves a very low efficiency roll-off (only $\approx 5\%$ dropped EQE at $400\,000\text{ cd m}^{-2}$).^[14]

8.3. Operational Stability

The operational lifetime of PeLEDs remains significantly shorter than that of commercial OLEDs. For other practical mobile applications beyond widely-used televisions and mobile phones, a T_{50} of at least 10^6 h at an initial luminance of 100 cd m^{-2} is considered necessary, reflecting the typical daily usage patterns and replacement cycles of electronic devices. Additionally, there is increasing demand for high stability under extremely high luminance ($10^5\text{--}10^6\text{ cd m}^{-2}$) for AR/VR applications.^[1,209,210] To enable commercialization, further research must focus on improving operational stability and elucidating the degradation mechanisms of PeLEDs. Addressing the intrinsic and extrinsic factors contributing to their instability is essential. Among these, ion migration and Joule heating are key intrinsic factors that synergistically accelerate degradation.

8.3.1. Ion Migration

Ion migration occurs when charged defects or ions within the perovskite lattice migrate under electric fields.^[211] The weak ionic bonds in perovskite crystals facilitate the formation of point defects (e.g., interstitial atoms, substitutional atoms, and vacancies), which can migrate as ions (in the case of interstitial atoms, and substitutional atoms) or serve as pathways for ion migration (in the case of vacancies). This migration results in luminance overshooting and a sudden increase in driving voltage.^[79,211] Additionally, ion-penetrated CTLs degrade their charge transport properties and interact with metallic electrodes, triggering electrochemical reactions.^[212,213]

Various strategies, including mixed-cation compositions, molecular passivation of grain boundaries, and the formation of 2D perovskite barriers, have shown promise in suppressing light-induced ion migration in perovskite solar cells.^[143,214,215] Although these approaches have also been applied to PeLEDs, they are insufficient to achieve the operational lifetime required for commercialization. This limitation arises from the stronger electric fields applied during PeLED operation and the smaller grain sizes of perovskites (in the tens of nanometers), which result in a high surface-to-volume ratio. This challenge is further amplified in PNC-LEDs, where the dominant surface area and weakly bound ligands promote ion migration and device instability.

To address these issues, we propose new criteria for ligand (or spacer cation/anion) design to mitigate ion migration in nanocrystalline perovskites under strong electric fields. Traditional ligand research has focused on two key aspects: 1) surface defect passivation to achieve high quantum yield and 2) maintaining high conductivity of perovskites in a film state to facilitate charge injection from CTLs. We suggest adding a third criterion: the ability to suppress ion migration. Promising strategies include stabilizing the perovskite surface through strong coordinative binding molecules, such as DSPA in colloidal PNCs,^[176] and employing CMM like TPBi.^[6] Moreover, aromatic short-chain lig-

ands capable of forming covalent bonds, such as BPA,^[14] can further enhance device stability, as covalent bonds provide stronger and more stable bonding compared with coordinate or hydrogen bonds. Additionally, crosslinking methods can further hinder ion migration and enhance the operational lifetime of PeLEDs.^[216]

8.3.2. Joule Heating

Joule heating occurs when electrical energy is converted into thermal energy due to resistance during current flow. This effect becomes more severe under high-luminance operation, which demands high current density and driving voltage, particularly for AR/VR display applications. The elevated temperature caused by Joule heating accelerates PeLED degradation through thermal quenching of excitons and promotes ion diffusion, severely deteriorating operational stability.

Thermal quenching in perovskites leads to significant efficiency loss in PeLEDs at elevated temperatures. For instance, CsPbBr₃ PNC-LEDs lose over 50% of their efficiency at $70\text{ }^\circ\text{C}$.^[217] This quenching is attributed to defect-induced exciton-phonon coupling or thermally activated exciton trapping at surface trap states. Proper surface passivation is therefore critical. For example, 2,7-dibromo-9,9-bis (3'-diethoxyphosphorylpropyl)-fluorene has been used in Q2D-PeLEDs as an effective passivation agent, maintaining 85% of the initial EQE at $85\text{ }^\circ\text{C}$ by preventing thermal quenching.^[218] In PNC-LEDs, fluorinated surface formation using didodecyl dimethylammonium fluoride creates a type-I-like junction at the surface, suppressing thermally activated surface trapping and preserving 80% of the EQE at $70\text{ }^\circ\text{C}$.^[173]

To mitigate temperature rise caused by Joule heating, employing heat sinks or substrates with high thermal conductivity is an effective approach. These solutions help suppress temperature increases, maintain low operating temperatures, and extend operational lifetime. For instance, using a sapphire substrate with a graphite sheet can increase the maximum current density of 2.5 kA cm^{-2} , and the increased operation lifetime from 0.52 to 5.42 h at a high current density of 100 mA cm^{-2} .^[219]

Additionally, utilizing sub-bandgap emission enables PeLEDs to achieve electroluminescence at extremely low voltages ($\approx 70\%$ of their bandgap voltage), significantly improving operational lifetime with negligible Joule heating. Achieving efficient sub-bandgap operation requires suppressing exciton quenching at the interface of the perovskite emitter with CTLs while ensuring strong charge transport and high conductivity in CTLs.^[220,221] By employing 3D/0D perovskites and modifying HTLs and ETLs to reduce device series resistance, voltages of 2.3 V and 2.7 V were achieved at a luminance of 1000 and $10\,000\text{ cd m}^{-2}$, respectively. Furthermore, the device maintained room temperature during continuous operation for 5 min at a luminance of $10\,000\text{ cd m}^{-2}$. This approach ultimately achieved a remarkable lifetime of 7691 h.^[221]

8.3.3. Environmental Factors

Moisture and oxygen are critical environmental factors that contribute significantly to PeLED degradation. Moisture interacts with hygroscopic materials like metal halides and organic

cations, leading to the formation of monohydrate and dihydrate phases, which eventually degrade into non-emissive species such as PbX_2 .^[222] This degradation also produces volatile compounds like methylamine and HX .^[223] Furthermore, oxygen can react with lead-halide-rich surfaces, forming thermodynamically favored halate species (XO_3^-) and lead(II) halate ($\text{Pb}(\text{XO}_3)_2$) through irreversible chemical reactions, further destabilizing PeLED.^[224]

To mitigate the detrimental effects of oxygen and moisture, some studies have demonstrated the effectiveness of using all-inorganic CTLs such as NiO_x and ZnO . These materials can prevent the penetration of oxygen and moisture into the perovskite layer, allowing unencapsulated devices to retain 80% of their EL intensity under ambient air conditions (28 °C, 30–50% humidity), whereas devices with organic CTLs undergo rapid degradation.^[217,225] This suggests that employing all-inorganic CTLs is a promising approach to enhance PeLED stability against environmental factors.

Additionally, efforts to fabricate perovskite devices under ambient conditions have also been reported. Although humidity and heating in ambient air can induce the formation of unwanted n -phases in Q2D perovskites, interstitial doping with Sb^{3+} or Ga^{3+} has been shown to enhance stability. These dopants help maintain the $n = 3$ phase in ambient conditions, improving both stability and efficiency. This approach enabled the fabrication of ambient air-processed deep-blue Q2D-PeLEDs with an EQE of 2.05%.^[226]

9. Conclusion

In this review, we examined the development of nanocrystalline perovskites and PeLEDs, with a focus on material-design strategies. The development perspectives for the three perovskite structures (PC, Q2D, and PNC) vary significantly. For PCs, grain-size control and defect passivation are crucial; for Q2Ds, n -phase modulation and energy funneling are key strategies; and for PNCs, ligand or surface engineering and doping are essential. These tailored approaches have led to highly efficient nanocrystalline PeLEDs, demonstrating their potential for use in next-generation commercial displays.

Despite these advancements, challenges remain, particularly in achieving long operational lifetimes and reducing efficiency roll-off as the size of nanograins and nanocrystals decreases. Addressing these issues requires converging material-design strategies across different nanocrystalline perovskites. A common direction for material design is emerging, with the following key criteria:

- 1) Optimal grain/crystal size (≈ 10 nm or slightly higher):** Maintaining grain sizes within this range maximizes radiative excitonic recombination by increasing exciton binding energy. Grain sizes smaller than this tend to increase surface defects and Auger recombination, whereas larger grains lose efficient excitonic recombination at low carrier densities.
- 2) Strongly binding passivators:** Using passivators with strong coordinative bonding or multipods interactions effectively passivates surface defects. Synergistic combinations of molecules can further enhance the stability and efficiency of the perovskite layer.

- 3) Retained charge carrier mobility with thick emissive layers:** When designing surfaces with strongly binding molecules, it is crucial to maintain high charge carrier mobility even though the size of nanograins or nanocrystals decreases down to ≈ 10 nm. This ensures efficient charge transport, even in thick emissive layers, which in turn enhances device stability and luminance.

By adhering to these development criteria, both the efficiency and operational lifetimes of nanocrystalline PeLEDs can be improved. Such progress would significantly advance PeLEDs toward commercialization, meeting the needs of next-generation display technologies. Continued collaborative efforts in material design and device engineering are essential to overcome the remaining challenges and fully realize the potential of PeLEDs in practical applications.

Acknowledgements

K.Y., S.E.C., D.H.K., and E.Y. contributed equally to this work. This work was supported by the National Research Foundation of Korea (NRF) grant funded by the Korea government (Ministry of Science, ICT & Future Planning) (NRF-2016R1A3B1908431, 2022M3H4A1A04096380).

Conflict of Interest

The authors declare no competing interests.

Keywords

defect management, exciton recombination dynamics, perovskite nanocrystals, polycrystalline perovskites, quasi-2D perovskites

Received: October 14, 2024

Revised: December 31, 2024

Published online:

- [1] T.-H. Han, K. Y. Jang, Y. Dong, R. H. Friend, E. H. Sargent, T.-W. Lee, *Nat. Rev. Mater.* **2022**, *7*, 757.
- [2] L. Protesescu, S. Yakunin, M. I. Bodnarchuk, F. Krieg, R. Caputo, C. H. Hendon, R. X. Yang, A. Walsh, M. V. Kovalenko, *Nano Lett.* **2015**, *15*, 3692.
- [3] K. Y. Jang, S. Y. Hwang, S.-J. Woo, E. Yoon, C.-Y. Park, S. Y. Kim, D.-H. Kim, H. Kim, J. Park, E. H. Sargent, T.-W. Lee, *Adv. Mater.* **2024**, *36*, 2404856.
- [4] F. Chun, K. Y. Jang, H. Zhou, S. Kim, E. Yoon, T.-W. Lee, *Small* **2024**, *2400959*.
- [5] H. Lee, J. Park, S. Kim, S.-C. Lee, Y.-H. Kim, T.-W. Lee, *Adv. Mater. Technol.* **2020**, *5*, 2000091.
- [6] D.-H. Kim, S.-J. Woo, C. P. Huelmo, M.-H. Park, A. M. Schankler, Z. Dai, J.-M. Heo, S. Kim, G. Reuveni, S. Kang, J. S. Kim, H. J. Yun, J. Park, J. Park, O. Yaffe, A. M. Rappe, T.-W. Lee, *Nat. Commun.* **2024**, *15*, 6245.
- [7] J. Y. Woo, M.-H. Park, S.-H. Jeong, Y.-H. Kim, B. Kim, T.-W. Lee, T.-H. Han, *Adv. Mater.* **2023**, *35*, 2207454.
- [8] H. Moon, W. Lee, J. Kim, D. Lee, S. Cha, S. Shin, H. Chae, *Chem. Commun.* **2019**, *55*, 13299.
- [9] S. D. Stranks, G. E. Eperon, G. Grancini, C. Menelaou, M. J. P. Alcocer, T. Leijtens, L. M. Herz, A. Petrozza, H. J. Snaith, *Science* **2013**, *342*, 341.

- [10] H. Cho, S.-H. Jeong, M.-H. Park, Y.-H. Kim, C. Wolf, C.-L. Lee, J. H. Heo, A. Sadhanala, N. Myoung, S. Yoo, S. H. Im, R. H. Friend, T.-W. Lee, *Science* **2015**, *350*, 1222.
- [11] J. Byun, H. Cho, C. Wolf, M. Jang, A. Sadhanala, R. H. Friend, H. Yang, T.-W. Lee, *Adv. Mater.* **2016**, *28*, 7515.
- [12] L. C. Schmidt, A. Pertegás, S. González-Carrero, O. Malinkiewicz, S. Agouram, G. Mínguez Espallargas, H. J. Bolink, R. E. Galian, J. Pérez-Prieto, *J. Am. Chem. Soc.* **2014**, *136*, 850.
- [13] Z.-K. Tan, R. S. Moghaddam, M. L. Lai, P. Docampo, R. Higler, F. Deschler, M. Price, A. Sadhanala, L. M. Pazos, D. Credgington, F. Hanusch, T. Bein, H. J. Snaith, R. H. Friend, *Nat. Nanotechnol.* **2014**, *9*, 687.
- [14] J. S. Kim, J.-M. Heo, G.-S. Park, S.-J. Woo, C. Cho, H. J. Yun, D.-H. Kim, J. Park, S.-C. Lee, S.-H. Park, E. Yoon, N. C. Greenham, T.-W. Lee, *Nature* **2022**, *611*, 688.
- [15] H. Wang, F. U. Kosasih, H. Yu, G. Zheng, J. Zhang, G. Pozina, Y. Liu, C. Bao, Z. Hu, X. Liu, L. Kobera, S. Abbrent, J. Brus, Y. Jin, M. Fahlman, R. H. Friend, C. Ducati, X.-K. Liu, F. Gao, *Nat. Commun.* **2020**, *11*, 891.
- [16] J. Zeng, X. Sun, Y. Liu, W. Jin, S. He, X. Zhu, K. Niu, G. Sun, J. Li, H. He, T. Sun, Z. Ye, Y. Jin, *Nat. Photonics* **2024**, *18*, 325.
- [17] C. Bi, Z. Yao, J. Hu, X. Wang, M. Zhang, S. Tian, A. Liu, Y. Lu, N. H. de Leeuw, M. Sui, J. Tian, *ACS Energy Lett.* **2023**, *8*, 731.
- [18] L. H. Eun, K. J. Hong, Presented at 2016 IEEE 6th International Conference on Consumer Electronics – Berlin, ICCE, Berlin **2016**, 141–144.
- [19] S. J. Park, C. Keum, H. Zhou, T.-W. Lee, W. Choe, H. Cho, *Adv. Mater. Technol.* **2023**, *8*, 2201070.
- [20] E.-L. Hsiang, Z. Yang, Q. Yang, P.-C. Lai, C.-L. Lin, S.-T. Wu, *Adv. Opt. Photonics* **2022**, *14*, 783.
- [21] S. Ding, Q. Wang, W. Gu, Z. Tang, B. Zhang, C. Wu, X. Zhang, H. Chen, X. Zhang, R. Cao, T. Chen, L. Qian, C. Xiang, *Nat. Photonics* **2024**, *18*, 363.
- [22] Y.-K. Wang, H. Wan, S. Teale, L. Grater, F. Zhao, Z. Zhang, H.-W. Duan, M. Imran, S.-D. Wang, S. Hoogland, L.-S. Liao, *Nature* **2024**, *629*, 586.
- [23] A. Liu, C. Bi, J. Tian, *Adv. Funct. Mater.* **2022**, *32*, 2207069.
- [24] R. Su, Z. Xu, J. Wu, D. Luo, Q. Hu, W. Yang, X. Yang, R. Zhang, H. Yu, T. P. Russell, Q. Gong, W. Zhang, R. Zhu, *Nat. Commun.* **2021**, *12*, 2479.
- [25] A. Miyata, A. Mitioglu, P. Plochocka, O. Portugall, J. T.-W. Wang, S. D. Stranks, H. J. Snaith, R. J. Nicholas, *Nat. Phys.* **2015**, *11*, 582.
- [26] Y.-H. Kim, S. Kim, A. Kakekhani, J. Park, J. Park, Y.-H. Lee, H. Xu, S. Nagane, R. B. Wexler, D.-H. Kim, S. H. Jo, L. Martínez-Sarti, P. Tan, A. Sadhanala, G.-S. Park, Y.-W. Kim, B. Hu, H. J. Bolink, S. Yoo, R. H. Friend, A. M. Rappe, T.-W. Lee, *Nat. Photonics* **2021**, *15*, 148.
- [27] C. Sun, Y. Jiang, M. Cui, L. Qiao, J. Wei, Y. Huang, L. Zhang, T. He, S. Li, H.-Y. Hsu, C. Qin, R. Long, M. Yuan, *Nat. Commun.* **2021**, *12*, 2207.
- [28] Y.-H. Kim, C. Wolf, H. Kim, T.-W. Lee, *Nano Energy* **2018**, *52*, 329.
- [29] J. Qin, X.-K. Liu, C. Yin, F. Gao, *Trends Chem* **2021**, *3*, 34.
- [30] Y. Jiang, M. Cui, S. Li, C. Sun, Y. Huang, J. Wei, L. Zhang, M. Lv, C. Qin, Y. Liu, M. Yuan, *Nat. Commun.* **2021**, *12*, 336.
- [31] M. B. Johnston, L. M. Herz, *Acc. Chem. Res.* **2016**, *49*, 146.
- [32] Y.-H. Kim, H. Cho, J. H. Heo, T.-S. Kim, N. Myoung, C.-L. Lee, S. H. Im, T.-W. Lee, *Adv. Mater.* **2015**, *27*, 1248.
- [33] S. E. Chang, C.-Y. Park, E. Yoon, J. S. Kim, T.-W. Lee, *J. Inf. Disp.* **2024**, *25*, 97.
- [34] Y.-H. Kim, G.-H. Lee, Y.-T. Kim, C. Wolf, H. J. Yun, W. Kwon, C. G. Park, T.-W. Lee, *Nano Energy* **2017**, *38*, 51.
- [35] K. Yan, M. Long, T. Zhang, Z. Wei, H. Chen, S. Yang, J. Xu, *J. Am. Chem. Soc.* **2015**, *137*, 4460.
- [36] P. Boonmongkolras, D. Kim, E. M. Alhabshi, I. Gereige, B. Shin, *RSC Adv.* **2018**, *8*, 21551.
- [37] M. Li, Y. Zhao, X. Qin, Q. Ma, J. Lu, K. Lin, P. Xu, Y. Li, W. Feng, W.-H. Zhang, Z. Wei, *Nano Lett.* **2022**, *22*, 2490.
- [38] Q. Cui, D. Zhang, Y. Gao, C. Fan, Q. Cai, H. Li, X. Wu, M. Zhu, J. Si, X. Dai, H. He, Z. Ye, *ACS Nano* **2024**, *18*, 10609.
- [39] Y.-H. Song, J. Ge, L.-B. Mao, K.-H. Wang, X.-L. Tai, Q. Zhang, L. Tang, J.-M. Hao, J.-S. Yao, J.-J. Wang, T. Ma, J.-N. Yang, Y.-F. Lan, X.-C. Ru, L.-Z. Feng, G. Zhang, Y. Lin, Q. Zhang, H.-B. Yao, *Sci. Adv.* **2024**, *8*, eabq2321.
- [40] Z. Ren, B. Guo, S. Liu, Y. Lian, Y. Wang, S. Xing, Y. Yang, G. Zhang, W. Tang, Y. Gao, Z. Wang, J. Hong, M. Yu, S. Zhang, D. Lan, C. Zou, B. Zhao, D. Di, *ACS Appl. Mater. Interfaces* **2024**, *16*, 9012.
- [41] J. Kim, B. Park, J. Baek, J. S. Yun, H.-W. Kwon, J. Seidel, H. Min, S. Coelho, S. Lim, S. Huang, K. Gaus, M. A. Green, T. J. Shin, A. W. Y. Ho-baillie, M. G. Kim, S. I. Seok, *J. Am. Chem. Soc.* **2020**, *142*, 6251.
- [42] D. P. McMeekin, Z. Wang, W. Rehman, F. Pulvirenti, J. B. Patel, N. K. Noel, M. B. Johnston, S. R. Marder, L. M. Herz, H. J. Snaith, *Adv. Mater.* **2017**, *29*, 1607039.
- [43] N. K. Noel, M. Congiu, A. J. Ramadan, S. Fearn, D. P. McMeekin, J. B. Patel, M. B. Johnston, B. Wenger, H. J. Snaith, *Joule* **2017**, *1*, 328.
- [44] M.-H. Park, J. S. Kim, J.-M. Heo, S. Ahn, S.-H. Jeong, T.-W. Lee, *ACS Energy Lett.* **2019**, *4*, 1134.
- [45] V. K. LaMer, R. H. Dinegar, *J. Am. Chem. Soc.* **1950**, *72*, 4847.
- [46] J.-M. Heo, H. Cho, S.-C. Lee, M.-H. Park, J. S. Kim, H. Kim, J. Park, Y.-H. Kim, H. J. Yun, E. Yoon, D.-H. Kim, S. Ahn, S.-J. Kwon, C.-Y. Park, T.-W. Lee, *ACS Energy Lett.* **2022**, *7*, 2807.
- [47] Y. Liu, F. Li, L. Qiu, K. Yang, Q. Li, X. Zheng, H. Hu, T. Guo, C. Wu, T. W. Kim, *ACS Nano* **2019**, *13*, 2042.
- [48] X. Ji, X. Peng, Y. Lei, Z. Liu, X. Yang, *Org. Electron.* **2017**, *43*, 167.
- [49] S. Ahn, M.-H. Park, S.-H. Jeong, Y.-H. Kim, J. Park, S. Kim, H. Kim, H. Cho, C. Wolf, M. Pei, H. Yang, T.-W. Lee, *Adv. Funct. Mater.* **2019**, *29*, 1807535.
- [50] C. Bi, Q. Wang, Y. Shao, Y. Yuan, Z. Xiao, J. Huang, *Nat. Commun.* **2015**, *6*, 7747.
- [51] J. Lee, H. Kang, G. Kim, H. Back, J. Kim, S. Hong, B. Park, E. Lee, K. Lee, *Adv. Mater.* **2017**, *29*, 1606363.
- [52] L. Veeramuthu, F.-C. Liang, Z.-X. Zhang, C.-J. Cho, E. Ercan, C.-C. Chueh, W.-C. Chen, R. Borsali, C.-C. Kuo, *ACS Omega* **2020**, *5*, 8972.
- [53] L. Zhang, X. Yang, Q. Jiang, P. Wang, Z. Yin, X. Zhang, H. Tan, Y. (Michael) Yang, M. Wei, B. R. Sutherland, E. H. Sargent, J. You, *Nat. Commun.* **2017**, *8*, 15640.
- [54] M. Karlsson, Z. Yi, S. Reichert, X. Luo, W. Lin, Z. Zhang, C. Bao, R. Zhang, S. Bai, G. Zheng, P. Teng, L. Duan, Y. Lu, K. Zheng, T. Pullerits, C. Deibel, W. Xu, R. Friend, F. Gao, *Nat. Commun.* **2021**, *12*, 361.
- [55] J. H. Warby, B. Wenger, A. J. Ramadan, R. D. J. Oliver, H. C. Sansom, A. R. Marshall, H. J. Snaith, *ACS Nano* **2020**, *14*, 8855.
- [56] Z. Li, K. Cao, J. Li, X. Du, Y. Tang, B. Yu, *Org. Electron.* **2020**, *81*, 105675.
- [57] E. G. Dyrvik, J. H. Warby, M. M. McCarthy, A. J. Ramadan, K.-A. Zaininger, A. E. Lauritzen, S. Mahesh, R. A. Taylor, H. J. Snaith, *ACS Nano* **2023**, *17*, 3289.
- [58] M.-H. Park, S.-H. Jeong, H.-K. Seo, C. Wolf, Y.-H. Kim, H. Kim, J. Byun, J. S. Kim, H. Cho, T.-W. Lee, *Nano Energy* **2017**, *42*, 157.
- [59] H. Cho, J. S. Kim, C. Wolf, Y.-H. Kim, H. J. Yun, S.-H. Jeong, A. Sadhanala, V. Venugopalan, J. W. Choi, C.-L. Lee, R. H. Friend, T.-W. Lee, *ACS Nano* **2018**, *12*, 2883.
- [60] K. H. Ngai, X. Sun, Y. Wang, L. Lin, Z. Chen, Q. Wei, M. Li, C. Luan, W. Zhang, J. Xu, M. Long, *Adv. Funct. Mater.* **2023**, *33*, 2211830.
- [61] S. R. Pering, P. J. Cameron, *Mater. Adv.* **2022**, *3*, 7918.
- [62] D. W. Ferdani, S. R. Pering, D. Ghosh, P. Kubiak, A. B. Walker, S. E. Lewis, A. L. Johnson, P. J. Baker, M. S. Islam, P. J. Cameron, *Energy Environ. Sci.* **2019**, *12*, 2264.
- [63] L. Zhang, Y. Jiang, Y. Feng, M. Cui, S. Li, X. Fu, H.-Y. Hsu, C. Qin, M. Yuan, *Angew. Chem., Int. Ed.* **2023**, *62*, 202302184.

- [64] K. Lin, J. Xing, L. N. Quan, F. P. G. de Arquer, X. Gong, J. Lu, L. Xie, W. Zhao, D. Zhang, C. Yan, W. Li, X. Liu, Y. Lu, J. Kirman, E. H. Sargent, Q. Xiong, Z. Wei, *Nature* **2018**, 562, 245.
- [65] X. Gong, X. Hao, J. Si, Y. Deng, K. An, Q. Hu, Q. Cai, Y. Gao, Y. Ke, N. Wang, Z. Du, M. Cai, Z. Ye, X. Dai, Z. Liu, *ACS Nano* **2024**, 18, 8673.
- [66] J. Li, P. Du, Q. Guo, L. Sun, Z. Shen, J. Zhu, C. Dong, L. Wang, X. Zhang, L. Li, C. Yang, J. Pan, Z. Liu, B. Xia, Z. Xiao, J. Du, B. Song, J. Luo, J. Tang, *Nat. Photonics* **2023**, 17, 435.
- [67] M. T. Weller, O. J. Weber, J. M. Frost, A. Walsh, *J. Phys. Chem. Lett.* **2015**, 6, 3209.
- [68] Z. Qiu, F. Wang, C. Wang, C. Zhu, H. Wang, Q. Chen, Y. Chen, Y. Zhang, Z. Guo, N. Li, H. Zai, J. M. Vicent-Luna, S. Tao, H. Zhou, *Nano Energy* **2022**, 99, 107388.
- [69] L. Na Quan, D. Ma, Y. Zhao, O. Voznyy, H. Yuan, E. Bladt, J. Pan, F. P. García de Arquer, R. Sabatini, Z. Piontkowski, A.-H. Emwas, P. Todorović, R. Quintero-Bermudez, G. Walters, J. Z. Fan, M. Liu, H. Tan, M. I. Saidaminov, L. Gao, Y. Li, D. H. Anjum, N. Wei, J. Tang, D. W. McCamant, M. B. J. Roeffaers, S. Bals, J. Hofkens, O. M. Bakr, Z.-H. Lu, E. H. Sargent, *Nat. Commun.* **2020**, 11, 170.
- [70] B. Guo, R. Lai, S. Jiang, L. Zhou, Z. Ren, Y. Lian, P. Li, X. Cao, S. Xing, Y. Wang, W. Li, C. Zou, M. Chen, Z. Hong, C. Li, B. Zhao, D. Di, *Nat. Photonics* **2022**, 16, 637.
- [71] H. Kim, J.-M. Heo, C. Wolf, Y.-H. Kim, S.-C. Lee, E. Yoon, G.-H. Lee, K. Y. Jang, J. Park, J. S. Kim, M.-H. Park, S.-H. Jeong, H. Cho, T.-H. Han, E. Oveisi, M. K. Nazeeruddin, T.-W. Lee, *Small* **2024**, 2405272.
- [72] H.-K. Seo, H. Kim, J. Lee, M.-H. Park, S.-H. Jeong, Y.-H. Kim, S.-J. Kwon, T.-H. Han, S. Yoo, T.-W. Lee, *Adv. Mater.* **2017**, 29, 1605587.
- [73] C. Lin, Y. Zou, H. Hu, P. Lin, P. Wang, X. Wu, L. Xu, C. Cui, *ACS Appl. Energy Mater.* **2024**, 7, 2496.
- [74] Q. Zhang, Y. Zhao, X. Qin, M. Li, H. Sun, P. Zhou, W. Feng, Y. Li, J. Lu, K. Lin, L. Shi, Z. Wei, *Adv. Funct. Mater.* **2024**, 34, 2308547.
- [75] C. C. Boyd, R. C. Shallcross, T. Moot, R. Kerner, L. Bertoluzzi, A. Onno, S. Kavadiya, C. Chosy, E. J. Wolf, J. Werner, J. A. Raiford, C. de Paula, A. F. Palmstrom, Z. J. Yu, J. J. Berry, S. F. Bent, Z. C. Holman, J. M. Luther, E. L. Ratcliff, N. R. Armstrong, M. D. McGehee, *Joule* **2020**, 4, 1759.
- [76] Y. Zhao, M. Li, X. Qin, P. Yang, W.-H. Zhang, Z. Wei, *ACS Appl. Mater. Interfaces* **2023**, 15, 3644.
- [77] S. Xing, Y. Yuan, G. Zhang, S. Zhang, Y. Lian, W. Tang, K. Zhou, S. Liu, Y. Gao, Z. Ren, G. Zhang, T. Sun, B. Zhao, D. Di, *ACS Energy Lett.* **2024**, 9, 3643.
- [78] Q. Wang, Y. Chen, C. Yan, X. Zeng, X. Fu, L. Pan, J. Cao, S. Yang, W. Li, X. Chen, W. Yang, *ACS Energy Lett.* **2023**, 8, 3710.
- [79] H. Kim, J. S. Kim, J.-M. Heo, M. Pei, I.-H. Park, Z. Liu, H. J. Yun, M.-H. Park, S.-H. Jeong, Y.-H. Kim, J.-W. Park, E. Oveisi, S. Nagane, A. Sadhanala, L. Zhang, J. J. Kweon, S. K. Lee, H. Yang, H. M. Jang, R. H. Friend, K. P. Loh, M. K. Nazeeruddin, N.-G. Park, T.-W. Lee, *Nat. Commun.* **2020**, 11, 3378.
- [80] Y. Jiang, C. Sun, J. Xu, S. Li, M. Cui, X. Fu, Y. Liu, Y. Liu, H. Wan, K. Wei, T. Zhou, W. Zhang, Y. Yang, J. Yang, C. Qin, S. Gao, J. Pan, Y. Liu, S. Hoogland, E. H. Sargent, J. Chen, M. Yuan, *Nature* **2022**, 612, 679.
- [81] Y. Jiang, K. Wei, C. Sun, Y. Feng, L. Zhang, M. Cui, S. Li, W.-D. Li, J. T. Kim, C. Qin, M. Yuan, *Adv. Mater.* **2023**, 35, 2304094.
- [82] M. Jiang, X. Zhang, F. Wang, *Adv. Mater.* **2024**, 36, 2400565.
- [83] W. Yu, M. Wei, Z. Tang, H. Zou, L. Li, Y. Zou, S. Yang, Y. Wang, Y. Zhang, X. Li, H. Guo, C. Wu, B. Qu, Y. Gao, G. Lu, S. Wang, Z. Chen, Z. Liu, H. Zhou, B. Wei, Y. Liao, L. Zhang, Y. Li, Q. Gong, E. H. Sargent, L. Xiao, *Adv. Mater.* **2023**, 35, 2301114.
- [84] M. Yuan, L. N. Quan, R. Comin, G. Walters, R. Sabatini, O. Voznyy, S. Hoogland, Y. Zhao, E. M. Bearegard, P. Kanjanaboos, Z. Lu, D. H. Kim, E. H. Sargent, *Nat. Nanotechnol.* **2016**, 11, 872.
- [85] I. C. Smith, E. T. Hoke, D. Solis-Ibarra, M. D. McGehee, H. I. Karunadasa, *Angew. Chem., Int. Ed.* **2014**, 53, 11232.
- [86] J. Dong, W. Yang, K. Cho, J. H. Jung, H. Zhou, E. Yoon, H. Chen, H.-D. Lee, S. H. Jo, J.-M. Park, Q. Zeng, T. Long, K. Y. Jang, S. E. Chang, C.-Y. Park, M.-J. Sung, J. S. Kim, H. Kim, D. Song, Z. Xu, J. Park, J.-Y. Sun, T.-W. Lee, *ACS Energy Lett.* **2024**, 9, 5879.
- [87] M. Kumagai, T. Takagahara, *Phys. Rev. B* **1989**, 40, 12359.
- [88] K. Tanaka, T. Takahashi, T. Kondo, T. Umabayashi, K. Asai, K. Erma, *Phys. Rev. B* **2005**, 71, 45312.
- [89] G. C. Papavassiliou, *Prog. Solid State Chem.* **1997**, 25, 125.
- [90] R. Chakraborty, G. Paul, A. J. Pal, *Phys. Rev. Appl.* **2022**, 17, 54045.
- [91] C. Katan, N. Mercier, J. Even, *Chem. Rev.* **2019**, 119, 3140.
- [92] B. Traore, L. Pedesseau, L. Assam, X. Che, J.-C. Blancon, H. Tsai, W. Nie, C. C. Stoumpos, M. G. Kanatzidis, S. Tretiak, A. D. Mohite, J. Even, M. Kepenekian, C. Katan, *ACS Nano* **2018**, 12, 3321.
- [93] L. N. Quan, M. Yuan, R. Comin, O. Voznyy, E. M. Bearegard, S. Hoogland, A. Buin, A. R. Kirmani, K. Zhao, A. Amassian, D. H. Kim, E. H. Sargent, *J. Am. Chem. Soc.* **2016**, 138, 2649.
- [94] D. Ma, K. Lin, Y. Dong, H. Choubisa, A. H. Proppe, D. Wu, Y.-K. Wang, B. Chen, P. Li, J. Z. Fan, F. Yuan, A. Johnston, Y. Liu, Y. Kang, Z.-H. Lu, Z. Wei, E. H. Sargent, *Nature* **2021**, 599, 594.
- [95] H. Qi, Y. Tong, X. Zhang, H. Wang, L. Zhang, Y. Chen, Y. Wang, J. Shang, K. Wang, H. Wang, *Adv. Mater.* **2024**, 36, 2409319.
- [96] Z. Guo, Y. Liang, D. Ni, L. Li, S. Liu, Y. Zhang, Q. Chen, Q. Zhang, Q. Wang, H. Zhou, *Adv. Mater.* **2023**, 35, 2302711.
- [97] S. Liu, Z. Guo, X. Wu, X. Liu, Z. Huang, L. Li, J. Zhang, H. Zhou, L.-D. Sun, C.-H. Yan, *Adv. Mater.* **2023**, 35, 2208078.
- [98] J. Xing, Y. Zhao, M. Askerka, L. N. Quan, X. Gong, W. Zhao, J. Zhao, H. Tan, G. Long, L. Gao, Z. Yang, O. Voznyy, J. Tang, Z.-H. Lu, Q. Xiong, E. H. Sargent, *Nat. Commun.* **2018**, 9, 3541.
- [99] Y. Xia, B. Song, Z. Zhang, K.-L. Wang, Y.-H. Li, N. Li, C.-H. Chen, J. Chen, G. Xing, Z.-K. Wang, *Angew. Chem., Int. Ed.* **2024**, 63, 202403739.
- [100] F. Wang, Z. Wang, W. Sun, Z. Wang, Y. Bai, T. Hayat, A. Alsaedi, Z. Tan, *Small* **2020**, 16, 2002940.
- [101] M. Worku, A. Ben-Akacha, S. Sridhar, J. R. Frick, S. Yin, Q. He, A. J. Robb, M. Chaaban, H. Liu, J. S. R. V. Winfred, K. Hanson, F. So, D. Dougherty, B. Ma, *Adv. Funct. Mater.* **2021**, 31, 2103299.
- [102] Y. Zhang, M. Chen, T. He, H. Chen, Z. Zhang, H. Wang, H. Lu, Q. Ling, Z. Hu, Y. Liu, Y. Chen, G. Long, *Adv. Mater.* **2023**, 35, 2210836.
- [103] T. Jiang, H. Min, R. Zou, M. Wang, K. Wen, J. Lai, L. Xu, Y. Wang, W. Xu, C. Wang, K. Wei, N. V. Medhekar, Q. Peng, J. Chang, W. Huang, J. Wang, *J. Phys. Chem. Lett.* **2022**, 13, 4098.
- [104] B. He, T. Liu, C. Wang, Z. Wen, B. Sun, W. Wen, G. Xing, X. Gao, S. Chen, *Small* **2023**, 19, 2303255.
- [105] B. Chen, H. Liu, J. Yang, M. Ahmadi, Q. Chen, N. Yin, S. Zhang, M. Xiao, H. Zhang, L. Xu, P. Chen, *Adv. Funct. Mater.* **2024**, 34, 2402522.
- [106] J. Jiang, Z. Chu, Z. Yin, J. Li, Y. Yang, J. Chen, J. Wu, J. You, X. Zhang, *Adv. Mater.* **2022**, 34, 2204460.
- [107] K. Wang, Z.-Y. Lin, Z. Zhang, L. Jin, K. Ma, A. H. Coffey, H. R. Atapattu, Y. Gao, J. Y. Park, Z. Wei, B. P. Finkenauer, C. Zhu, X. Meng, S. N. Chowdhury, Z. Chen, T. Terlier, T.-H. Do, Y. Yao, K. R. Graham, A. Boltasseva, T.-F. Guo, L. Huang, H. Gao, B. M. Savoie, L. Dou, *Nat. Commun.* **2023**, 14, 397.
- [108] M. Ban, Y. Zou, J. P. H. Rivett, Y. Yang, T. H. Thomas, Y. Tan, T. Song, X. Gao, D. Credgington, F. Deschler, H. Sirringhaus, B. Sun, *Nat. Commun.* **2018**, 9, 3892.
- [109] S. Yuan, T. Fang, B. Han, Q. Shan, C. Wei, X. Zheng, X. Li, B. Xu, H. Zeng, *Adv. Funct. Mater.* **2024**, 34, 2316206.
- [110] H. Rui, X. Wu, Y. Qiu, X. Liu, S. Bu, H. Cao, S. Yin, *Adv. Funct. Mater.* **2023**, 33, 2308147.
- [111] M. Yu, C. Yi, N. Wang, L. Zhang, R. Zou, Y. Tong, H. Chen, Y. Cao, Y. He, Y. Wang, M. Xu, Y. Liu, Y. Jin, W. Huang, J. Wang, *Adv. Opt. Mater.* **2019**, 7, 1801575.

- [112] Y. Shang, Y. Liao, Q. Wei, Z. Wang, B. Xiang, Y. Ke, W. Liu, Z. Ning, *Sci. Adv.* **2024**, 5, eaaw8072.
- [113] Z. Ren, J. Yu, Z. Qin, J. Wang, J. Sun, C. C. S. Chan, S. Ding, K. Wang, R. Chen, K. S. Wong, X. Lu, W.-J. Yin, W. C. H. Choy, *Adv. Mater.* **2021**, 33, 2005570.
- [114] X. Bao, Y. Gao, Y. Liu, Z. Xu, F. Zhang, M. Lu, Z. Wu, Y. Wu, Q. Wang, Y. Zhang, Y. Wang, Z. Shi, J. Hu, X. Bai, *ACS Energy Lett.* **2023**, 8, 1018.
- [115] H.-D. Lee, H. Kim, H. Cho, W. Cha, Y. Hong, Y.-H. Kim, A. Sadhanala, V. Venugopalan, J. S. Kim, J. W. Choi, C.-L. Lee, D. Kim, H. Yang, R. H. Friend, T.-W. Lee, *Adv. Funct. Mater.* **2019**, 29, 1901225.
- [116] W. Dong, X. Zhang, F. Yang, Q. Zeng, W. Yin, W. Zhang, H. Wang, X. Yang, S. V. Kershaw, B. Yang, A. L. Rogach, W. Zheng, *ACS Nano* **2022**, 16, 9679.
- [117] A. Liu, P. Lu, M. Lu, X. Chai, Y. Liu, G. Guan, Y. Gao, Z. Wu, X. Bai, J. Hu, D. Wang, Y. Zhang, *Nano Lett.* **2023**, 23, 11082.
- [118] J.-W. Lee, Z. Dai, T.-H. Han, C. Choi, S.-Y. Chang, S.-J. Lee, N. De Marco, H. Zhao, P. Sun, Y. Huang, Y. Yang, *Nat. Commun.* **2018**, 9, 3021.
- [119] Z. Tang, Y. Guo, Z. Li, Q. Wang, Y. Fu, Z. Xie, *J Mater Chem C Mater* **2024**, 12, 9693.
- [120] H. Xue, Z. Chen, S. Tao, G. Brocks, *ACS Energy Lett.* **2024**, 9, 2343.
- [121] H. Li, X. Zhu, D. Zhang, Y. Gao, Y. Feng, Z. Ma, J. Huang, H. He, Z. Ye, X. Dai, *Nat. Commun.* **2024**, 15, 6561.
- [122] F. Zhang, H. Zhong, C. Chen, X. Wu, X. Hu, H. Huang, J. Han, B. Zou, Y. Dong, *ACS Nano* **2015**, 9, 4533.
- [123] J. Song, J. Li, X. Li, L. Xu, Y. Dong, H. Zeng, *Adv. Mater.* **2015**, 27, 7162.
- [124] Y.-H. Kim, C. Wolf, Y.-T. Kim, H. Cho, W. Kwon, S. Do, A. Sadhanala, C. G. Park, S.-W. Rhee, S. H. Im, R. H. Friend, T.-W. Lee, *ACS Nano* **2017**, 11, 6586.
- [125] T.-W. Lee, S. Im, Y.-H. Kim, H. Cho, Perovskite nanocrystalline particles and optoelectronic device using same, WO2016072805A1, Priority date: 6 November 2014
- [126] T.-W. Lee, Y.-H. Kim, H. Cho, Wavelength converting particle, method for manufacturing wavelength converting particle, and light-emitting diode containing wavelength converting particle, WO2016072803A1. Priority date: 6 November 2014.
- [127] T.-W. Lee, Y.-H. Kim, H. Cho, Perovskite nanocrystal particle light emitting body with core-shell structure, method for fabricating same, and light emitting element using same, WO2016072806A2, Priority date: 6 November 2014.
- [128] A. Pan, B. He, X. Fan, Z. Liu, J. J. Urban, A. P. Alivisatos, L. He, Y. Liu, *ACS Nano* **2016**, 10, 7943.
- [129] B. J. Bohn, Y. Tong, M. Gramlich, M. L. Lai, M. Döblinger, K. Wang, R. L. Z. Hoyer, P. Müller-Buschbaum, S. D. Stranks, A. S. Urban, L. Polavarapu, J. Feldmann, *Nano Lett.* **2018**, 18, 5231.
- [130] C. Otero-Martínez, D. García-Lojo, I. Pastoriza-Santos, J. Pérez-Juste, L. Polavarapu, *Angew. Chem., Int. Ed.* **2021**, 60, 26677.
- [131] S. R. Smock, Y. Chen, A. J. Rossini, R. L. Brutchey, *Acc. Chem. Res.* **2021**, 54, 707.
- [132] G. Almeida, L. Goldoni, Q. Akkerman, Z. Dang, A. H. Khan, S. Marras, I. Moreels, L. Manna, *ACS Nano* **2018**, 12, 1704.
- [133] H. Huang, A. S. Susha, S. V. Kershaw, T. F. Hung, A. L. Rogach, *Adv. Sci.* **2015**, 2, 1500194.
- [134] Y. Dong, T. Qiao, D. Kim, D. Parobek, D. Rossi, D. H. Son, *Nano Lett.* **2018**, 18, 3716.
- [135] W. Sun, R. Yun, Y. Liu, X. Zhang, M. Yuan, L. Zhang, X. Li, *Small* **2023**, 19, 2205950.
- [136] Q. A. Akkerman, T. P. T. Nguyen, S. C. Boehme, F. Montanarella, D. N. Dirin, P. Wechsler, F. Beiglböck, G. Rainò, R. Erni, C. Katan, J. Even, M. V. Kovalenko, *Science* **2022**, 377, 1406.
- [137] J. Li, L. Xu, T. Wang, J. Song, J. Chen, J. Xue, Y. Dong, B. Cai, Q. Shan, B. Han, H. Zeng, *Adv. Mater.* **2017**, 29, 1603885.
- [138] K. Hoshi, T. Chiba, J. Sato, Y. Hayashi, Y. Takahashi, H. Ebe, S. Ohisa, J. Kido, *ACS Appl. Mater. Interfaces* **2018**, 10, 24607.
- [139] K. Vighnesh, S. Wang, H. Liu, A. L. Rogach, *ACS Nano* **2022**, 16, 19618.
- [140] N. Fiuza-Maneiro, K. Sun, I. López-Fernández, S. Gómez-Graña, P. Müller-Buschbaum, L. Polavarapu, *ACS Energy Lett.* **2023**, 8, 1152.
- [141] K. Chen, Q. Zhong, W. Chen, B. Sang, Y. Wang, T. Yang, Y. Liu, Y. Zhang, H. Zhang, *Adv. Funct. Mater.* **2019**, 29, 1900991.
- [142] K. L. Svane, A. C. Forse, C. P. Grey, G. Kieslich, A. K. Cheetham, A. Walsh, K. T. Butler, *J. Phys. Chem. Lett.* **2017**, 8, 6154.
- [143] J.-W. Lee, S. Tan, S. Il Seok, Y. Yang, N.-G. Park, *Science* **1979** **2024**, 375, eabj1186.
- [144] J. Zhuang, J. Wang, F. Yan, *Nanomicro Lett* **2023**, 15, 84.
- [145] X. Zhang, H. Liu, W. Wang, J. Zhang, B. Xu, K. L. Karen, Y. Zheng, S. Liu, S. Chen, K. Wang, X. W. Sun, *Adv. Mater.* **2017**, 29, 1606405.
- [146] M. Lu, X. Zhang, X. Bai, H. Wu, X. Shen, Y. Zhang, W. Zhang, W. Zheng, H. Song, W. W. Yu, A. L. Rogach, *ACS Energy Lett.* **2018**, 3, 1571.
- [147] Y. Gao, Q. Cai, Y. He, D. Zhang, Q. Cao, M. Zhu, Z. Ma, B. Zhao, H. He, D. Di, Z. Ye, X. Dai, *Sci. Adv.* **2024**, 10, eado5645.
- [148] W. van der Stam, J. J. Geuchies, T. Altantzis, K. H. W. van den Bos, J. D. Meeldijk, S. Van Aert, S. Bals, D. Vanmaekelbergh, C. de Mello Donega, *J. Am. Chem. Soc.* **2017**, 139, 4087.
- [149] A. Dey, J. Ye, A. De, E. Debroye, S. K. Ha, E. Bladt, A. S. Kshirsagar, Z. Wang, J. Yin, Y. Wang, L. N. Quan, F. Yan, M. Gao, X. Li, J. Shamsi, T. Debnath, M. Cao, M. A. Scheel, S. Kumar, J. A. Steele, M. Gerhard, L. Chouhan, K. Xu, X. Wu, Y. Li, Y. Zhang, A. Dutta, C. Han, I. Vincon, A. L. Rogach, et al., *ACS Nano* **2021**, 15, 10775.
- [150] J. Zhang, J. Wang, L. Cai, S. Wang, K. Wu, B. Sun, W. Zheng, S. V. Kershaw, G. Jia, X. Zhang, A. L. Rogach, X. Yang, *Angew. Chem., Int. Ed.* **2024**, 63, 202403996.
- [151] M. Lu, X. Zhang, Y. Zhang, J. Guo, X. Shen, W. W. Yu, A. L. Rogach, *Adv. Mater.* **2018**, 30, 1804691.
- [152] X. Shen, Y. Zhang, S. V. Kershaw, T. Li, C. Wang, X. Zhang, W. Wang, D. Li, Y. Wang, M. Lu, L. Zhang, C. Sun, D. Zhao, G. Qin, X. Bai, W. W. Yu, A. L. Rogach, *Nano Lett.* **2019**, 19, 1552.
- [153] S. Dastidar, D. A. Egger, L. Z. Tan, S. B. Cromer, A. D. Dillon, S. Liu, L. Kronik, A. M. Rappe, A. T. Fafarman, *Nano Lett.* **2016**, 16, 3563.
- [154] J.-S. Yao, J. Ge, K.-H. Wang, G. Zhang, B.-S. Zhu, C. Chen, Q. Zhang, Y. Luo, S.-H. Yu, H.-B. Yao, *J. Am. Chem. Soc.* **2019**, 141, 2069.
- [155] C. Chen, T. Xuan, W. Bai, T. Zhou, F. Huang, A. Xie, L. Wang, R.-J. Xie, *Nano Energy* **2021**, 85, 106033.
- [156] Z.-J. Yong, S.-Q. Guo, J.-P. Ma, J.-Y. Zhang, Z.-Y. Li, Y.-M. Chen, B.-B. Zhang, Y. Zhou, J. Shu, J.-L. Gu, L.-R. Zheng, O. M. Bakr, H.-T. Sun, *J. Am. Chem. Soc.* **2018**, 140, 9942.
- [157] M. Seitz, A. J. Magdaleno, N. Alcázar-Cano, M. Meléndez, T. J. Lubbers, S. W. Walraven, S. Pakdel, E. Prada, R. Delgado-Buscalioni, F. Prins, *Nat. Commun.* **2020**, 11, 2035.
- [158] J.-S. Yao, J. Ge, B.-N. Han, K.-H. Wang, H.-B. Yao, H.-L. Yu, J.-H. Li, B.-S. Zhu, J.-Z. Song, C. Chen, Q. Zhang, H.-B. Zeng, Y. Luo, S.-H. Yu, *J. Am. Chem. Soc.* **2018**, 140, 3626.
- [159] J. Pan, L. N. Quan, Y. Zhao, W. Peng, B. Murali, S. P. Sarmah, M. Yuan, L. Sinatra, N. M. Alyami, J. Liu, E. Yassitepe, Z. Yang, O. Voznyy, R. Comin, M. N. Hedhili, O. F. Mohammed, Z. H. Lu, D. H. Kim, E. H. Sargent, O. M. Bakr, *Adv. Mater.* **2016**, 28, 8718.
- [160] J. Song, J. Li, L. Xu, J. Li, F. Zhang, B. Han, Q. Shan, H. Zeng, *Adv. Mater.* **2018**, 30, 1800764.
- [161] Z. Zeng, Y. Meng, Z. Yang, Y. Ye, Q. Lin, Z. Meng, H. Hong, S. Ye, Z. Cheng, Q. Lan, J. Wang, Y. Chen, H. Zhang, Y. Bai, X. Jiang, B. Liu, J. Hong, T. Guo, F. Li, Y. Chen, Z. Weng, *ACS Appl. Mater. Interfaces* **2024**, 16, 10389.
- [162] L. Gao, T. Cheng, L. Gou, Y. Zhang, Y. Liu, L. Yuan, X. Zhang, Y. Wang, F. Meng, J. Zhang, *ACS Appl. Mater. Interfaces* **2023**, 15, 18125.

- [163] M. Li, J. Wang, J. Yao, S. Wang, L. Xu, J. Song, *Adv. Funct. Mater.* **2024**, *34*, 2308341.
- [164] T. Chiba, Y. Hayashi, H. Ebe, K. Hoshi, J. Sato, S. Sato, Y.-J. Pu, S. Ohisa, J. Kido, *Nat. Photonics* **2018**, *12*, 681.
- [165] H. Wang, F. Ye, J. Sun, Z. Wang, C. Zhang, J. Qian, X. Zhang, W. C. H. Choy, X. W. Sun, K. Wang, W. Zhao, *ACS Energy Lett.* **2022**, *7*, 1137.
- [166] C. Bi, Z. Yao, X. Sun, X. Wei, J. Wang, J. Tian, *Adv. Mater.* **2021**, *33*, 2006722.
- [167] C. Zhao, C. Zhu, Y. Yu, W. Xue, X. Liu, F. Yuan, J. Dai, S. Wang, B. Jiao, Z. Wu, *ACS Appl. Mater. Interfaces* **2023**, *15*, 40080.
- [168] X. Luo, R. Lai, Y. Li, Y. Han, G. Liang, X. Liu, T. Ding, J. Wang, K. Wu, *J. Am. Chem. Soc.* **2019**, *141*, 4186.
- [169] X. Luo, Y. Han, Z. Chen, Y. Li, G. Liang, X. Liu, T. Ding, C. Nie, M. Wang, F. N. Castellano, K. Wu, *Nat. Commun.* **2020**, *11*, 28.
- [170] C. Qin, T. Matsushima, W. J. Potscavage, A. S. D. Sandanayaka, M. R. Leyden, F. Bencheikh, K. Goushi, F. Mathevet, B. Heinrich, G. Yumoto, Y. Kanemitsu, C. Adachi, *Nat. Photonics* **2020**, *14*, 70.
- [171] Y. Li, M. Deng, X. Zhang, T. Xu, X. Wang, Z. Yao, Q. Wang, L. Qian, C. Xiang, *Nat. Commun.* **2024**, *15*, 5696.
- [172] H. Zhao, H. Chen, S. Bai, C. Kuang, X. Luo, P. Teng, C. Yin, P. Zeng, L. Hou, Y. Yang, L. Duan, F. Gao, M. Liu, *ACS Energy Lett.* **2021**, *6*, 2395.
- [173] M. Liu, Q. Wan, H. Wang, F. Carulli, X. Sun, W. Zheng, L. Kong, Q. Zhang, C. Zhang, Q. Zhang, S. Brovelli, L. Li, *Nat. Photonics* **2021**, *15*, 379.
- [174] X. Zheng, S. Yuan, J. Liu, J. Yin, F. Yuan, W.-S. Shen, K. Yao, M. Wei, C. Zhou, K. Song, B.-B. Zhang, Y. Lin, M. N. Hedhili, N. Wehbe, Y. Han, H.-T. Sun, Z.-H. Lu, T. D. Anthopoulos, O. F. Mohammed, E. H. Sargent, L.-S. Liao, O. M. Bakr, *ACS Energy Lett.* **2020**, *5*, 793.
- [175] J. Zhang, B. Cai, X. Zhou, F. Yuan, C. Yin, H. Wang, H. Chen, X. Ji, X. Liang, C. Shen, Y. Wang, Z. Ma, J. Qing, Z. Shi, Z. Hu, L. Hou, H. Zeng, S. Bai, F. Gao, *Adv. Mater.* **2023**, *35*, 2303938.
- [176] H. Li, Y. Feng, M. Zhu, Y. Gao, C. Fan, Q. Cui, Q. Cai, K. Yang, H. He, X. Dai, J. Huang, Z. Ye, *Nat. Nanotechnol.* **2024**, *19*, 638.
- [177] H. Li, H. Lin, D. Ouyang, C. Yao, C. Li, J. Sun, Y. Song, Y. Wang, Y. Yan, Y. Wang, Q. Dong, W. C. H. Choy, *Adv. Mater.* **2021**, *33*, 2008820.
- [178] B. Lyu, H. Lin, D. Li, A. Sergeev, Q. Wang, Z. Jiang, L. Huo, H. Su, K. S. Wong, Y. Wang, W. C. H. Choy, *ACS Energy Lett.* **2024**, *9*, 2118.
- [179] L. Xu, J. Li, B. Cai, J. Song, F. Zhang, T. Fang, H. Zeng, *Nat. Commun.* **2020**, *11*, 3902.
- [180] C. Chen, T. Xuan, Y. Yang, F. Huang, T. Zhou, L. Wang, R.-J. Xie, *ACS Appl. Mater. Interfaces* **2022**, *14*, 16404.
- [181] K. Yang, J. Zheng, J. Mao, H. Zhao, S. Ju, Q. Zhang, Z. Lin, Y. Yu, F. Li, *ACS Appl. Mater. Interfaces* **2023**, *15*, 40062.
- [182] O. Yaffe, Y. Guo, L. Z. Tan, D. A. Egger, T. Hull, C. C. Stoumpos, F. Zheng, T. F. Heinz, L. Kronik, M. G. Kanatzidis, J. S. Owen, A. M. Rappe, M. A. Pimenta, L. E. Brus, *Phys. Rev. Lett.* **2017**, *118*, 136001.
- [183] M. J. Schilcher, P. J. Robinson, D. J. Abramovitch, L. Z. Tan, A. M. Rappe, D. R. Reichman, D. A. Egger, *ACS Energy Lett.* **2021**, *6*, 2162.
- [184] M. Z. Mayers, L. Z. Tan, D. A. Egger, A. M. Rappe, D. R. Reichman, *Nano Lett.* **2018**, *18*, 8041.
- [185] M. J. Schilcher, D. J. Abramovitch, M. Z. Mayers, L. Z. Tan, D. R. Reichman, D. A. Egger, *Phys. Rev. Mater.* **2023**, *7*, L081601.
- [186] F. Zhao, H.-W. Duan, S.-N. Li, J.-L. Pan, W.-S. Shen, S.-M. Li, Q. Zhang, Y.-K. Wang, L.-S. Liao, *Angew. Chem., Int. Ed.* **2023**, *62*, 202311089.
- [187] Y.-K. Wang, F. Jia, X. Li, S. Teale, P. Xia, Y. Liu, P. T. Chan, H. Wan, Y. Hassan, M. Imran, H. Chen, L. Grater, L.-D. Sun, G. C. Walker, S. Hoogland, Z.-H. Lu, C.-H. Yan, L.-S. Liao, E. H. Sargent, *Sci. Adv.* **2024**, *9*, eadh2140.
- [188] Y. Dong, Y.-K. Wang, F. Yuan, A. Johnston, Y. Liu, D. Ma, M.-J. Choi, B. Chen, M. Chekini, S.-W. Baek, L. K. Sagar, J. Fan, Y. Hou, M. Wu, S. Lee, B. Sun, S. Hoogland, R. Quintero-Bermudez, H. Ebe, P. Todorovic, F. Dinic, P. Li, H. T. Kung, M. I. Saidaminov, E. Kumacheva, E. Spiecker, L.-S. Liao, O. Voznyy, Z.-H. Lu, E. H. Sargent, *Nat. Nanotechnol.* **2020**, *15*, 668.
- [189] Y.-K. Wang, F. Yuan, Y. Dong, J.-Y. Li, A. Johnston, B. Chen, M. I. Saidaminov, C. Zhou, X. Zheng, Y. Hou, K. Bertens, H. Ebe, D. Ma, Z. Deng, S. Yuan, R. Chen, L. K. Sagar, J. Liu, J. Fan, P. Li, X. Li, Y. Gao, M.-K. Fung, Z.-H. Lu, O. M. Bakr, L.-S. Liao, E. H. Sargent, *Angew. Chem., Int. Ed.* **2021**, *60*, 16164.
- [190] F. Zhang, J. Song, B. Cai, X. Chen, C. Wei, T. Fang, H. Zeng, *Sci Bull (Beijing)* **2021**, *66*, 2189.
- [191] F. Chun, K. Y. Jang, T.-W. Lee, *Sci Bull (Beijing)* **2021**, *66*, 2159.
- [192] T.-H. Han, M.-H. Park, S.-J. Kwon, S.-H. Bae, H.-K. Seo, H. Cho, J.-H. Ahn, T.-W. Lee, *NPG Asia Mater* **2016**, *8*, e303.
- [193] Y.-M. Xie, L.-S. Liao, M.-K. Fung, *Adv. Funct. Mater.* **2024**, *n/a*, 2401789.
- [194] D. Zhao, Z. Qin, J. Huang, J. Yu, *Org. Electron.* **2017**, *51*, 220.
- [195] M. Zhu, S.-Q. Sun, W. He, Y.-L. Xu, Q. Sun, Y.-M. Xie, M.-K. Fung, S.-T. Lee, *J Mater Chem C Mater* **2024**, *12*, 2623.
- [196] L. Kong, Y. Luo, Q. Wu, X. Xiao, Y. Wang, G. Chen, J. Zhang, K. Wang, W. C. H. Choy, Y.-B. Zhao, H. Li, T. Chiba, J. Kido, X. Yang, *Light Sci Appl* **2024**, *13*, 138.
- [197] H.-D. Lee, S.-J. Woo, S. Kim, J. Kim, H. Zhou, S. J. Han, K. Y. Jang, D.-H. Kim, J. Park, S. Yoo, T.-W. Lee, *Nat. Nanotechnol.* **2024**, *19*, 624.
- [198] S.-Q. Sun, Y. Cai, M. Zhu, W. He, B.-C. Liu, Y.-L. Xu, X. Lv, Q. Sun, P. Liu, T. Shi, Y.-M. Xie, M.-K. Fung, *Adv. Funct. Mater.* **2023**, *33*, 2306549.
- [199] R. Wang, H. Xiang, Y. Li, Y. Zhou, Q. Shan, Y. Su, Z. Li, Y. Wang, H. Zeng, *Adv. Funct. Mater.* **2023**, *33*, 2215189.
- [200] B. Zhao, M. Vasilopoulou, A. Fakhruddin, F. Gao, A. R. bin Mohd Yusoff, R. H. Friend, D. Di, *Nat. Nanotechnol.* **2023**, *18*, 981.
- [201] C. Cho, B. Zhao, G. D. Tainter, J.-Y. Lee, R. H. Friend, D. Di, F. Deschler, N. C. Greenham, *Nat. Commun.* **2020**, *11*, 611.
- [202] Y. Chen, D. Zhang, Y. Zhang, X. Zeng, T. Huang, Z. Liu, G. Li, L. Duan, *Adv. Mater.* **2021**, *33*, 2103293.
- [203] J. Cui, Y. Liu, Y. Deng, C. Lin, Z. Fang, C. Xiang, P. Bai, K. Du, X. Zuo, K. Wen, S. Gong, H. He, Z. Ye, Y. Gao, H. Tian, B. Zhao, J. Wang, Y. Jin, *Sci. Adv.* **2024**, *7*, eabg8458.
- [204] Q. Zhang, M. M. Tavakoli, L. Gu, D. Zhang, L. Tang, Y. Gao, J. Guo, Y. Lin, S.-F. Leung, S. Poddar, Y. Fu, Z. Fan, *Nat. Commun.* **2019**, *10*, 727.
- [205] Y. Shen, H.-Y. Wu, Y.-Q. Li, K.-C. Shen, X. Gao, F. Song, J.-X. Tang, *Adv. Funct. Mater.* **2021**, *31*, 2103870.
- [206] C. Xie, X. Zhao, E. W. Y. Ong, Z.-K. Tan, *Nat. Commun.* **2020**, *11*, 4213.
- [207] V. I. Klimov, A. A. Mikhailovsky, D. W. McBranch, C. A. Leatherdale, M. G. Bawendi, *Science* **1999**, *287*, 1011.
- [208] Z. Li, Z. Chen, Y. Yang, Q. Xue, H.-L. Yip, Y. Cao, *Nat. Commun.* **2019**, *10*, 1027.
- [209] S. R. Forrest, *Organic Electronics: Foundations to Applications*, Oxford University Press, Walton Street, Oxford **2020**.
- [210] S.-J. Woo, J. S. Kim, T.-W. Lee, *Nat. Photonics* **2021**, *15*, 630.
- [211] N. Li, Y. Jia, Y. Guo, N. Zhao, *Adv. Mater.* **2022**, *34*, 2108102.
- [212] H. Lee, D. Ko, C. Lee, *ACS Appl. Mater. Interfaces* **2019**, *11*, 11667.
- [213] T. Cheng, G. Tumen-Ulzii, D. Klotz, S. Watanabe, T. Matsushima, C. Adachi, *ACS Appl. Mater. Interfaces* **2020**, *12*, 33004.
- [214] S. Teale, M. Degani, B. Chen, E. H. Sargent, G. Grancini, *Nat. Energy* **2024**, *9*, 779.
- [215] H. Zhu, B. Shao, J. Yin, Z. Shen, L. Wang, R.-W. Huang, B. Chen, N. Wehbe, T. Ahmad, M. Abulikemu, A. Jamal, I. Gereige, M. Freitag, O. F. Mohammed, E. H. Sargent, O. M. Bakr, *Adv. Mater.* **2024**, *36*, 2306466.
- [216] B. Han, S. Yuan, B. Cai, J. Song, W. Liu, F. Zhang, T. Fang, C. Wei, H. Zeng, *Adv. Funct. Mater.* **2021**, *31*, 2011003.

- [217] Z. Shi, S. Li, Y. Li, H. Ji, X. Li, D. Wu, T. Xu, Y. Chen, Y. Tian, Y. Zhang, C. Shan, G. Du, *ACS Nano* **2018**, *12*, 1462.
- [218] D. Zhang, Y. Fu, H. Zhan, C. Zhao, X. Gao, C. Qin, L. Wang, *Light Sci Appl* **2022**, *11*, 69.
- [219] L. Zhao, K. Roh, S. Kacmoli, K. Al Kurdi, S. Jhulki, S. Barlow, S. R. Marder, C. Gmachl, B. P. Rand, *Adv. Mater.* **2020**, *32*, 2000752.
- [220] Y. Lian, D. Lan, S. Xing, B. Guo, Z. Ren, R. Lai, C. Zou, B. Zhao, R. H. Friend, D. Di, *Nat. Commun.* **2022**, *13*, 3845.
- [221] S. Zheng, Z. Wang, N. Jiang, H. Huang, X. Wu, D. Li, Q. Teng, J. Li, C. Li, J. Li, T. Pang, L. Zeng, R. Zhang, F. Huang, L. Lei, T. Wu, F. Yuan, D. Chen, *Sci. Adv.* **2024**, *10*, eadp8473.
- [222] R. Azmi, S. Zhumagali, H. Bristow, S. Zhang, A. Yazmaciyan, A. R. Pininti, D. S. Utomo, A. S. Subbiah, S. De Wolf, *Adv. Mater.* **2024**, *36*, 2211317.
- [223] J. M. Frost, K. T. Butler, F. Brivio, C. H. Hendon, M. van Schilfgaarde, A. Walsh, *Nano Lett.* **2014**, *14*, 2584.
- [224] J. Hidalgo, W. Kaiser, Y. An, R. Li, Z. Oh, A.-F. Castro-Méndez, D. K. LaFollette, S. Kim, B. Lai, J. Breternitz, S. Schorr, C. A. R. Perini, E. Mosconi, F. De Angelis, J.-P. Correa-Baena, *J. Am. Chem. Soc.* **2023**, *145*, 24549.
- [225] Z. Shi, Y. Li, Y. Zhang, Y. Chen, X. Li, D. Wu, T. Xu, C. Shan, G. Du, *Nano Lett.* **2017**, *17*, 313.
- [226] Y. Guo, P. Yang, F. Dong, H. Li, J. Gao, Z. Cheng, J. Wu, Y. Xu, H. Wang, H. Wang, *Adv. Sci.* **2024**, *12*, 2414499.
- [227] H. Shen, Q. Gao, Y. Zhang, Y. Lin, Q. Lin, Z. Li, L. Chen, Z. Zeng, X. Li, Y. Jia, S. Wang, Z. Du, L. S. Li, Z. Zhang, *Nat. Photonics* **2019**, *13*, 192.
- [228] Y. Deng, F. Peng, Y. Lu, X. Zhu, W. Jin, J. Qiu, J. Dong, Y. Hao, D. Di, Y. Gao, T. Sun, M. Zhang, F. Liu, L. Wang, L. Ying, F. Huang, Y. Jin, *Nat. Photonics* **2022**, *16*, 505.
- [229] Y.-H. Won, O. Cho, T. Kim, D.-Y. Chung, T. Kim, H. Chung, H. Jang, J. Lee, D. Kim, E. Jang, *Nature* **2019**, *575*, 634.
- [230] Y. Bian, X. Yan, F. Chen, Q. Li, B. Li, W. Hou, Z. Lu, S. Wang, H. Zhang, W. Zhang, D. Zhang, A. Tang, F. Fan, H. Shen, *Nature* **2024**, *635*, 854.
- [231] T. Kim, K.-H. Kim, S. Kim, S.-M. Choi, H. Jang, H.-K. Seo, H. Lee, D.-Y. Chung, E. Jang, *Nature* **2020**, *586*, 385.
- [232] K. Lin, C. Yan, R. P. Sabatini, W. Feng, J. Lu, K. Liu, D. Ma, Y. Shen, Y. Zhao, M. Li, C. Tian, L. Xie, E. H. Sargent, Z. Wei, *Adv. Funct. Mater.* **2022**, *32*, 2200350.
- [233] X. Qin, M. Li, Y. Zhao, J. Luo, Q. Zhang, E. Hou, J. Lu, J. Li, C. Tian, K. Lin, Z. Li, Z. Wei, *ACS Nano* **2024**, *18*, 14696.
- [234] Y. Zhao, W. Feng, M. Li, J. Lu, X. Qin, K. Lin, J. Luo, W.-H. Zhang, E. L. Lim, Z. Wei, *Nano Lett.* **2023**, *23*, 8560.
- [235] W. Xiong, C. Zou, W. Tang, S. Xing, Z. Wang, B. Zhao, D. Di, *ACS Energy Lett.* **2023**, *8*, 2897.
- [236] S. Lee, J. Kim, H. Kim, C. Kim, S. Kim, C. Kim, H. Lee, B. Choi, C. Muthu, T. Kim, J. Lee, S. Lee, H. Ihee, J.-Y. Lee, *Sci. Adv.* **2024**, *10*, eadn8465.
- [237] X. Sun, W. Meng, K. H. Ngai, Z. Nie, C. Luan, W. Zhang, S. Li, X. Lu, B. Wu, G. Zhou, M. Long, J. Xu, *Adv. Mater.* **2024**, *36*, 2400347.
- [238] Z. Li, Z. Ren, Q. Liang, P. W. K. Fong, J. Tian, G. Li, *Adv. Mater.* **2024**, *36*, 2313981.
- [239] Z. Li, Z. Ren, Q. Liang, P. W. K. Fong, H. Liu, X. Lu, I. (John) Kymissis, G. Li, *Joule* **2024**, *8*, 1176.
- [240] S. J. Yang, K. Wang, Y. Luo, J. Y. Park, H. Yang, A. H. Coffey, K. Ma, J. Sun, S. Wiegold, C. Zhu, L. Dou, *ACS Energy Lett.* **2023**, *8*, 3693.
- [241] J. Jiang, M. Shi, Z. Xia, Y. Cheng, Z. Chu, W. Zhang, J. Li, Z. Yin, J. You, X. Zhang, *Sci. Adv.* **2024**, *10*, eadn5683.
- [242] F. Yang, W. Dong, C. Kang, Z. Zhu, Q. Zeng, W. Zheng, X. Zhang, B. Yang, *Nano Lett.* **2024**, *24*, 7012.
- [243] D. Zhang, L. Chao, G. Jin, Z. Xing, W. Hong, Y. Chen, L. Wang, J. Chen, D. Ma, *Adv. Funct. Mater.* **2022**, *32*, 2205707.
- [244] S.-Q. Sun, J.-W. Tai, W. He, Y.-J. Yu, Z.-Q. Feng, Q. Sun, K.-N. Tong, K. Shi, B.-C. Liu, M. Zhu, G. Wei, J. Fan, Y.-M. Xie, L.-S. Liao, M.-K. Fung, *Adv. Mater.* **2024**, *36*, 2400421.
- [245] W. Bai, T. Xuan, H. Zhao, H. Dong, X. Cheng, L. Wang, R.-J. Xie, *Adv. Mater.* **2023**, *35*, 2302283.
- [246] D. Zhang, C. Liu, J. Sun, Q. Xiong, X. Xiao, D. Li, B. Lyu, H. Su, W. C. H. Choy, *ACS Energy Lett.* **2024**, *9*, 1133.
- [247] Z. Li, Z. Chen, Z. Shi, G. Zou, L. Chu, X.-K. Chen, C. Zhang, S. K. So, H.-L. Yip, *Nat. Commun.* **2023**, *14*, 6441.
- [248] C. Zhao, W. Wu, H. Zhan, W. Yuan, H. Li, D. Zhang, D. Wang, Y. Cheng, S. Shao, C. Qin, L. Wang, *Angew. Chem., Int. Ed.* **2022**, *61*, 202117374.
- [249] W. Dong, H. Li, J. Li, Y. Hua, F. Yang, Q. Dong, X. Zhang, W. Zheng, *Nano Lett.* **2024**, *24*, 3952.
- [250] L. Shu, B. Han, Q. Zhang, S. Poddar, D. Zhang, Y. Fu, Y.-B. Cao, Y. Ding, Y. Zhu, Y. Lin, D.-B. Kuang, J.-F. Liao, Z. Fan, *Adv. Funct. Mater.* **2023**, *33*, 2306570.
- [251] Y. Yu, B.-F. Wang, Y. Shen, Z.-H. Su, K. Zhang, H. Ren, Y.-F. Zhang, X. Gao, J.-X. Tang, Y.-Q. Li, *Angew. Chem., Int. Ed.* **2024**, *63*, 202319730.
- [252] W. Zhou, Y. Shen, L.-X. Cao, Y. Lu, Y.-Y. Tang, K. Zhang, H. Ren, F.-M. Xie, Y.-Q. Li, J.-X. Tang, *Adv. Funct. Mater.* **2023**, *33*, 2301425.
- [253] L. Wang, Z.-H. Su, Y. Shen, S.-C. Feng, F.-M. Xie, K. Zhang, K.-F. Meng, X. Gao, J.-X. Tang, Y.-Q. Li, *Adv. Funct. Mater.* **2024**, *34*, 2401297.
- [254] F. Zhang, Y. Yang, Y. Gao, D. Wang, W. Dong, P. Lu, X. Wang, M. Lu, Y. Wu, P. Chen, J. Hu, X. Yang, D. Zhou, D. Liu, L. Xu, B. Dong, Z. Wu, Y. Zhang, H. Song, X. Bai, *Nano Lett.* **2024**, *24*, 1268.
- [255] Y.-H. Li, Y. Xia, Z. Zhang, B. Wang, R.-J. Jin, C.-H. Chen, J. Chen, K.-L. Wang, G. Xing, Z.-K. Wang, L.-S. Liao, *ACS Nano* **2024**, *18*, 6513.
- [256] W. Yin, M. Li, W. Dong, X. Zhang, W. Zheng, *Angew. Chem., Int. Ed.* **2023**, *62*, 202303462.
- [257] H. Zhu, G. Tong, J. Li, E. Xu, X. Tao, Y. Sheng, J. Tang, Y. Jiang, *Adv. Mater.* **2022**, *34*, 2205092.
- [258] J. Pan, Z. Zhao, F. Fang, L. Wang, G. Wang, C. Liu, Q. Huang, J. Sun, Y. Huang, L. Mao, J. Xie, Y. Xue, J. Chen, W. Lei, *Adv. Opt. Mater.* **2022**, *10*, 2102569.
- [259] S. Hou, M. K. Gangishetty, Q. Quan, D. N. Congreve, *Joule* **2018**, *2*, 2421.
- [260] M. Lu, J. Guo, S. Sun, P. Lu, J. Wu, Y. Wang, S. V. Kershaw, W. W. Yu, A. L. Rogach, Y. Zhang, *Nano Lett.* **2020**, *20*, 2829.
- [261] Y. Gao, H. Li, X. Dai, X. Ying, Z. Liu, J. Qin, J. Guo, Z. Han, Y. Zhang, M. Zhu, X. Wu, Q. Cai, Y. Yang, L. Feng, X. Zhang, J. Huang, H. He, F. Gao, Z. Ye, *Nat. Electron.* **2024**, *7*, 487.
- [262] L. Ma, X. Li, X. Li, J. Song, Y. Nong, J. Huang, C. Wei, W. Zhang, B. Xu, *ACS Energy Lett.* **2024**, *9*, 1210.
- [263] H. Wang, X. Gong, D. Zhao, Y.-B. Zhao, S. Wang, J. Zhang, L. Kong, B. Wei, R. Quintero-Bermudez, O. Voznyy, Y. Shang, Z. Ning, Y. Yan, E. H. Sargent, X. Yang, *Joule* **2020**, *4*, 1977.
- [264] Y. Feng, H. Li, M. Zhu, Y. Gao, Q. Cai, G. Lu, X. Dai, Z. Ye, H. He, *Angew. Chem., Int. Ed.* **2024**, *63*, 202318777.
- [265] Y. Nong, J. Yao, J. Li, L. Xu, Z. Yang, C. Li, J. Song, *Adv. Mater.* **2024**, *36*, 2402325.
- [266] W. J. Mir, A. Alamoudi, J. Yin, K. E. Yorov, P. Maity, R. Naphade, B. Shao, J. Wang, M. N. Lintangpradipto, S. Nematulloev, A.-H. Emwas, A. Genovese, O. F. Mohammed, O. M. Bakr, *J. Am. Chem. Soc.* **2022**, *144*, 13302.
- [267] D. Chen, P. K. Ko, C.-H. A. Li, B. Zou, P. Geng, L. Guo, J. E. Halpert, *ACS Energy Lett.* **2023**, *8*, 410.
- [268] S. Sun, P. Jia, M. Lu, P. Lu, Y. Gao, Y. Zhong, C. Tang, Y. Zhang, Z. Wu, J. Zhu, Y. Zhang, W. W. Yu, X. Bai, *Adv. Funct. Mater.* **2022**, *32*, 2204286.
- [269] Y. Feng, M. Zhu, Q. Cao, H. Li, X. Zhu, X. Lyu, X. Dai, H. He, Z. Ye, *ACS Energy Lett.* **2024**, *9*, 1125.

- [270] Y. Hassan, J. H. Park, M. L. Crawford, A. Sadhanala, J. Lee, J. C. Sadighian, E. Mosconi, R. Shivanna, E. Radicchi, M. Jeong, C. Yang, H. Choi, S. H. Park, M. H. Song, F. De Angelis, C. Y. Wong, R. H. Friend, B. R. Lee, H. J. Snaith, *Nature* **2021**, 591, 72.
- [271] X. Shen, X. Zhang, Z. Wang, X. Gao, Y. Wang, P. Lu, X. Bai, J. Hu, Z. Shi, W. W. Yu, Y. Zhang, *Adv. Funct. Mater.* **2022**, 32, 2110048.
- [272] J. Song, T. Fang, J. Li, L. Xu, F. Zhang, B. Han, Q. Shan, H. Zeng, *Adv. Mater.* **2018**, 30, 1805409.



Kyung Yeon Jang is studying for his Ph.D. Course and received his B.S. degree in the Department of Materials Science and Engineering of Seoul National University. His current research focuses on the synthesis of blue-emitting perovskite quantum dots and the fabrication of perovskite LED for displays.



Seong Eui Chang received his B.S. degree in the Department of Materials Science and Engineering, at Yonsei University in 2022. He is currently a Ph.D. candidate student in the Department of Materials Science and Engineering, at Seoul National University. His current research focuses on the synthesis of quasi-2D and nanocrystalline polycrystal perovskites for the fabrication of light-emitting diodes for display.



Dong-Hyeok Kim is currently a Ph. D. candidate in the Department of Materials Science and Engineering at Seoul National University, Korea. He received his B.S. in the Department of Materials Science and Engineering from Hanyang University, Korea. His research interests include perovskite LEDs for displays and photophysical analysis of optoelectronic devices.



Eojin Yoon received his B.S. degree in the Department of Materials Science and Engineering, at Seoul National University in 2019. He is currently a Ph.D. candidate student in the Department of Materials Science and Engineering, at Seoul National University. His research focuses on the synthesis of perovskite nanoparticles for the fabrication of perovskite light-emitting diodes and the development of color conversion layers for micro-LEDs.



Tae-Woo Lee is a professor in MSE at Seoul National University, South Korea. He received his Ph.D. in Chemical Engineering from KAIST in 2002. He joined Bell Laboratories, USA, as a postdoctoral researcher and worked as a research staff at Samsung Advanced Institute of Technology (2003–2008). He was an associate professor at Pohang University of Science and Technology (POSTECH), South Korea, until 2016. He founded SN Display Co. Ltd. in 2020. His research focuses on soft printed electronics and optoelectronics based on organic and organic–inorganic hybrid electronic materials for flexible/stretchable displays, solar cells, neuromorphic computing, robotics, and bioelectronics.